Structural and functional characterization of CNNM magnesium transporters

Yu Seby Chen
Department of Biochemistry
McGill University
Montreal, Quebec, Canada
December 2020

A thesis submitted to McGill University in partial fulfillment of the requirements of the degree of Doctor of Philosophy

Abstract

CNNMs (cystathionine-β-synthase (CBS)-pair domain divalent metal cation transport mediators) represent a conserved family of integral membrane proteins implicated in Mg^{2+} homeostasis and divalent cation transport in bacteria, plants, and animals. Seventeen years since the discovery of CNNM proteins, the mechanism of Mg^{2+} transport by CNNM remains unknown and actively debated. Some groups suggest CNNMs directly transport divalent cations such as Mg^{2+} while other groups suggest CNNMs regulate other transporters. Structurally, CNNMs are defined by a conserved transmembrane domain and a cytosolic CBS-pair domain. Eukaryotic CNNMs contain an additional extracellular domain and a cytosolic C-terminal cyclic nucleotide-binding homology (CNBH) domain. Here, I carried out a stepwise structural approach to understand the function and mechanism of Mg^{2+} transport by CNNM proteins. I first characterized the structure and function of the C-terminal CNBH domain. I found that instead of binding cyclic nucleotides, CNBH domain functions as a dimerization domain functionally important for Mg^{2+} efflux. Next, I characterized the interplay of the CNNM cytosolic domains. I found that Mg^{2+} efflux function is regulated by conformational changes associated with Mg^{2+}-ATP binding to the CBS-pair domain. Lastly, I determined the structure of a prokaryotic CNNM consisting of the transmembrane domain and CBS-pair domain with Mg^{2+}-ATP-bound. The structure reveals a negatively charged cavity and a Na^{+}-binding site on the cytosolic side of the membrane. These results strongly suggest that CNNM proteins mediate ion transport across membranes and provide a structural basis for future studies of the function of CNNM proteins in health and disease.

Résumé

Les CNNMs (médiateurs du transport de cations métalliques divalents à domaine cystathionine-bêta-synthase (CBS)) sont une famille conservée de protéines membranaires intégrales impliquées dans l'homéostasie du Mg^{2+} et dans le transport de cations divalents chez les bactéries, les plantes et les animaux. Depuis leur découverte il y a plus de 17 ans, le mécanisme des CNNMs demeure inconnu et fait l'objet de débats. Certains groupes pensent que les CNNMs transportent directement les cations divalents (ex: Mg^{2+}), tandis que d'autres suggèrent que ces protéines participent à la régulation d'autres transporteurs d'ions. La structure générale des CNNMs est définie par un domaine transmembranaire conservé (DUF21) et un domaine cytosolique CBS. Les CNNMs eucaryotes contiennent un domaine extracellulaire supplémentaire, de même qu'un domaine homologue de liaison au nucléotide cyclique (CNBH) au C-terminus. Le but de mon projet est de caractériser les protéines CNNMs, en commençant par les domaines cytosoliques individuels jusqu'à la protéine transmembranaire complète, afin de mieux comprendre leur fonction biologique ainsi que leur mécanisme de transport du Mg^{2+}. J'ai d'abord déterminé la structure du domaine CNBH et démontré l'importance de son interface de dimérisation pour l'efflux de Mg^{2+} chez les CNNMs. Ensuite, j'ai caractérisé une interaction entre les deux domaines cytosoliques et démontré que la fonction d'efflux de Mg^{2+} est régulée par des changements de conformation associés à la liaison du complexe Mg^{2+}-ATP au domaine CBS. Enfin, j'ai déterminé la structure d'un CNNM procaryote contenant le domaine transmembranaire lié au complexe Mg^{2+}-ATP. Cette structure démontre que le domaine transmembranaire possède une cavité centrale chargée négativement, ainsi qu'un site de liaison pour le Na^{+} sur son côté cytosolique. Tous ces résultats suggèrent fortement que les CNNMs régulent le transport d'ions à travers les membranes cellulaires et constituent une base structurelle pour de futures études du rôle de ces protéines dans les maladies.

Table of Contents

List of Figures

List of Tables

List of Abbreviations

ABC transporter – ATP-binding cassette transporter

ACDP – ancient conserved domain protein

ADP – adenosine diphosphate

AHB – acidic helical bundle

AMP – adenosine monophosphate

AMP-PNP – adenosine 5'-(β,γ-imido)triphosphate

AMPK – AMP-activated protein kinase

ATP – adenosine triphosphate

ATPase – adenosine triphosphatase

AUC – analytical ultracentrifugation

BSA – bovine serum albumin

cAMP – cyclic adenosine monophosphate

CBS – cystathionine-β-synthase

cGMP – cyclic guanosine monophosphate

CHESS – Cornell High-Energy Synchrotron Source

CLS – Canadian Light Source

CMC – critical micelle concentration

CNBH – cyclic nucleotide-binding homology domain

CNNM – CBS-pair domain divalent metal cation transport mediator

cRNA – complementary RNA

DCT – distal convoluted tubule

DDM – n-dodecyl-β-D-maltopyranoside

DNA – deoxyribonucleic acid

DUF21 – domain of unknown function 21

ER – endoplasmic reticulum

GAPDH – glyceraldehyde 3-phosphate dehydrogenase

GST – glutathione S-transferase

GWAS – genome-wide association studies

HDX-MS – hydrogen deuterium exchange mass spectrometry

HPLC – high performance liquid chromatography

HSQC – ^{15}N-^{1}H heteronuclear single quantum correlation

IMAC – immobilized metal affinity chromatography

IMPDH – inosine-5'-monophosphate dehydrogenase

IPTG – isopropyl 1-thio-*β*-D-galactopyranoside

ITC – isothermal titration calorimetry

JM – juxtamembrane

KCNH – ether-à-go-go K^+

K_d – dissociation constant

MpfA – magnesium protection factor A

MR – molecular replacement

mRNA – messenger RNA

NMDG – *N*-methyl-D-glucamine

NMR – nuclear magnetic resonance

PBS – phosphate buffered saline

PDB – Protein Data Bank

PRL – phosphatase of regenerating liver

RMSD – root mean square deviation

RNA – ribonucleic acid

SAD – single-wavelength anomalous dispersion

SBFI – sodium-binding benzofuran isophthalate

SDS-PAGE – sodium dodecyl sulfate polyacrylamide gel electrophoresis

SPC – signal peptidase complex

SUMO – small ubiquitin-related modifier

SV-AUC – sedimentation velocity analytical ultracentrifugation

TAL – thick ascending limb

TMD – transmembrane domain

TRPM6/7 – transient receptor potential ion channel subfamily M member 6/7

TSA – thermal shift assay

UDM – n-undecyl-β-D-maltopyranoside

Preface

This is a manuscript-based thesis, consisting of two published articles and one manuscript in preparation.

Chapter 2

Chen, Y. S., Kozlov, G., Fakih, R., Funato, Y., Miki, H., and Gehring, K. (2018). The cyclic nucleotide–binding homology domain of the integral membrane protein CNNM mediates dimerization and is required for Mg^{2+} efflux activity. *Journal of Biological Chemistry* **293**, 19998-20007.

Chapter 3

Chen, Y. S., Kozlov, G., Fakih, R., Yang, M., Zhang, Z., Kovrigin, E. L., and Gehring, K. (2020). Mg^{2+}-ATP sensing in CNNM, a putative magnesium transporter. *Structure* **28**, 324-335.

Chapter 4

Chen, Y. S., Kozlov, G., Armitano, J., Moeller, B. E., Fakih, R., Burke, J. E., Gehring, K. Crystal structure of an archaeal CNNM magnesium transporter. *Manuscript in preparation.*

Author Contributions

Chapter 2

Guennadi Kozlov and I designed the experiments, cloned constructs, performed NMR experiments, and solved the crystal structures. Rayan Fakih and I performed TSA and AUC experiments. I performed gel-filtration experiments. Yosuke Funato and I performed Mg^{2+} efflux assays. Kalle Gehring, Guennadi Kozlov and I wrote the manuscript.

Chapter 3

I designed the experiments, cloned the constructs, purified proteins, solved the crystal structures, and performed ITC experiments, ATP hydrolysis, and Mg^{2+} efflux assays. Guennadi Kozlov assisted with crystallographic data collection and performed ITC experiments. Evgenii L. Kovrigin simulated the ITC titrations using the U-R2L2 model. Rayan Fakih and I performed the AUC experiments. Meng Yang performed initial crystallographic screening of CNNM3 cytosolic fragment structure. Zhidian Zhang assisted with protein purification for ITC experiments. Kalle Gehring and I wrote the manuscript.

Chapter 4

I designed the experiments, cloned constructs, performed small-scale screenings, purified proteins, solved crystal structures, and performed liposome transport assays. Guennadi Kozlov assisted with crystal screening and performed ITC experiments. Joshua Armitano performed complementation assays. Brandon Moeller and John Burke performed HDX-MS experiments. Rayan Fakih performed AUC experiments. Kalle Gehring and I wrote the manuscript.

Original Contributions to Knowledge

Chapter 2

- Determined the first crystal structures of CNBH domains from two human CNNM proteins.
- Contrary to expectations, CNBH domains do not bind cyclic nucleotides but mediate dimerization both in crystal and in solution.
- Mutational analysis revealed that CNBH domain is required for Mg^{2+} efflux activity.
- Together, these results highlight the importance of CNBH domain in CNNM function.

Chapter 3

- Determined crystal structures of cytosolic fragments of human CNNMs in two conformations: Mg^{2+}-AMP-PNP bound (closed) and ligand-free (open).
- The structures reveal functionally important contacts not observed in structures of the individual domains.
- A second Mg^{2+}-binding region in the CBS-pair domain and a different dimerization interface for the CNBH domain were identified.
- AUC and ITC experiments revealed a tight correlation between Mg^{2+}-ATP binding and CBS-pair domain dimerization.
- Mutations that blocked either function prevented cellular Mg^{2+} efflux activity.
- These results suggest that Mg^{2+} efflux is regulated by conformational changes associated with Mg^{2+}-ATP binding to the CBS-pair domains.

Chapter 4

- Performed high-throughput expression and detergent screening of 20 prokaryotic CNNM proteins.
- Performed *in vitro* liposome transport assay demonstrating direct Mg^{2+} transport by MtCNNM.
- Determined crystal structure of MtCNNM bound to Mg^{2+}-ATP.
- The structure reveals a novel transmembrane fold, representing the largest family of domain of unknown function.

- The transmembrane domain exists in an inward-facing conformation with a highly negatively charged cavity.
- The π-helix in TM3 is involved in coordinating a Na^+ ion.
- The structure reveals an acidic helical bundle enriched in acidic residues between TMD and CBS-pair domain.
- The results provide structural insights into the mechanism by which MtCNNM exchanges Na^+ and Mg^{2+}.

Acknowledgements

First to my supervisor, Dr. Kalle Gehring. Thank you for accepting me into your lab when I was a clueless undergrad, giving me a chance when others did not. You welcomed me into the world of structural biology and trained me to be a well-rounded scientist. You always come up with new things for me to learn. You taught me how to present and write better. You gave me confidence when I doubted myself. Most importantly, you taught me independence, perseverance, and skepticism.

I would not have made this far without the help of Gehring lab members. Dr. Jingwei Xie – you were my first mentor in the lab. You taught me almost everything I know, from using pipettes, cloning, protein purification to crystallization. Drs. Guennadi Kozlov and Véronique Sauvé – you are the yin and yang of Gehring lab. You are always there to answer my countless questions, trouble-shoot my experiments, and save me from malfunctioned instruments. Dr. Kathy Wong – you taught me how to clone and crystallize better. You also taught me how to survive in grad school. Without your tips, I doubt I would have survived. Dr. Meng Yang – thank you for always being there when I needed someone to talk with. You graciously transferred your grad school knowledge to me, teaching how to fish crystals and set up publication alerts. Thank you to all the present and past members of Gehring lab for the company and support. Big thanks to all the undergraduate students who have assisted me over the years: Zhidian Zhang, David Scarlata, Rayan Fakih, Robert Goldstein, Ioana Nica, Temi Oladeji, Ellie Zhang, and Samuel Nyandwi.

Being in the McGill Centre for Structural Biology, I am very fortunate to be surrounded by many talented students and researchers. Dr. Alexei Gorelik – thank you for teaching me how to process crystallographic data. Katalin Illes – thank you for teaching me how to culture insect and mammalian cells. Dr. Nadeem Siddiqui – thank you for your advice on AUC data processing. To my Research Advisory Committee members, Drs. John Silvius, Gergely Lukacs, and Alba Guarné, thank you for the constructive advice and criticism over the years.

This thesis would not be possible with the help from many collaborators. Dr. Katharina Dürr for allowing my exchange at your lab and teaching me everything I know about membrane proteins. Drs. Hiroaki Miki and Yosuke Funato for the Mg^{2+} efflux assays in Chapter 2 and teaching me how to do the assays in Chapter 3. Dr. Evgenii Kovrigin for the ITC analysis in

Chapter 3. Dr. Nazzareno D'Avanzo for showing me how to make liposomes. Dr. Joshua Armitano for the growth-based assay. Dr. John Burke and Brandon Moeller for the HDX-MS experiments.

A lot of the crystallographic data were collected at Cornell High-Energy Synchrotron Source (CHESS) and at Canadian Light Source (CLS). To the support staff at CLS: Michel Fodje, Shaun Labiuk, Bulat Gabidullin, and Kathyrn Janzen, thank you for taking good care of my crystals and answering my late-night calls.

Thank you to my funding sources: NSERC CREATE Training Program in Bionanomachines Graduate Research Award, Fonds de Recherche du Quebec (FRQS) Doctoral Award, and Canadian Institutes of Health Research (CIHR) Frederick Banting and Charles Best Canada Graduate Scholarship Doctoral Award.

Lastly, I would also like to thank my family and friends for supporting me during this arduous journey. Thank you for listening to me rant about my failed experiments and lab shenanigans. Finally, I would also like to thank myself for not giving up even though I thought about it a million times.

Chapter 1 – Introduction

1.1 Background on magnesium

Magnesium (Mg^{2+}), the most abundant divalent cation in cells, is essential for life [1]. Mg^{2+} is important for the maintenance of genomic stability as it acts as a counter ion for nucleic acids. Mg^{2+} forms complexes with ATP and is required for over 600 enzymatic reactions, including topoisomerases, helicases, exonucleases, protein kinases, cyclases, and ATPases [2]. Mg^{2+} is an essential co-factor for DNA and RNA polymerases and ribosomes [3-5]. Mg^{2+} plays key roles in the stabilization of cell membranes, neuronal transmission, and muscle contraction as it regulates the permeability of various ion channels [6]. In essence, Mg^{2+} is an important ion that is involved in almost every biochemical process within the cell, and pathological serum perturbations in Mg^{2+} levels are associated with many diseases, such as osteoporosis, diabetes, hypertension, neurological disorders, and immunodeficiency [7, 8].

Human adults contain approximately 25 g of magnesium unequally distributed across different tissues [9]. The largest amount is found in bones (~60%), where it resides on the surface of hydroxyapatite and in the hydration shell around the crystal, thus contributing to maintaining the integrity of the skeleton [10]. Intracellular Mg^{2+} concentrations range from 5 to 20 mM; 1-5% is free in solution (0.2 mM to 1 mM), the remainder is bound to proteins, negatively charged molecules and ATP [1]. Extracellular Mg^{2+} accounts for 1% of total body magnesium, which is primarily found in serum and red blood cells [11]. Balance between intestinal absorption and renal excretion is tightly regulated to keep the plasma Mg^{2+} concentration in its physiological range (0.7-1.1 mM) [12]. Mg^{2+} is unique among divalent cations in that it has the smallest ionic radius and largest hydrated radius [13]; therefore, the transport of Mg^{2+} across the membrane requires the action of specific channels and transporters, including CNNM proteins [2].

1.2 CNNM – functional characterizations

CNNMs (CBS-pair domain divalent metal cation transport mediators), discovered in 2003, are represented by four integral membrane proteins in humans called CNNM1, CNNM2, CNNM3, and CNNM4. They are known by other names such as ancient conserved domain protein (ACDP) or cyclin M (CNNM). They were named as ACDPs because they contain a domain that is evolutionarily highly conserved in diverse species ranging from bacteria, yeast, *C. elegans*, and Drosophila to mammals (**Fig. 1.1**) [14]. Later on, this family of proteins was speciously named as cyclin M because they were thought to have a cyclin box motif and a role in cell cycle regulation. However, a cyclin function was never demonstrated. Instead, CNNMs have been implicated in Mg^{2+} homeostasis and divalent metal handling. Therefore, retaining the same acronym, they have been renamed as CBS-pair domain divalent cation transport mediator, reflecting their conserved CBS-pair domain and role in divalent cation transport.

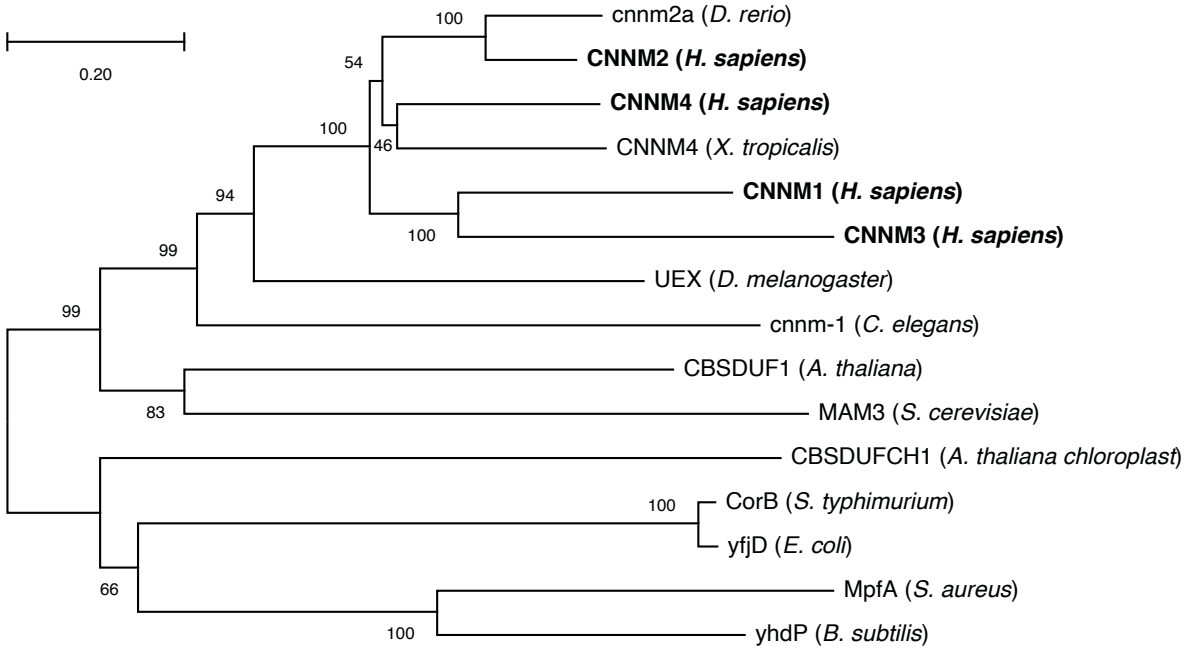

Figure 1.1 Phylogenetic analysis of the CNNM family

Amino acid sequences of various CNNM orthologs were aligned using MUSCLE [15], and the phylogenetic tree was generated using neighbor-joining method in MEGAX (Version 10.1.8) [16]. The number beside the branches reflect the confidence level by bootstrapping of 1,000 replications. The listed CNNM orthologs and their UniProt accession numbers are: cnnm2a

(*Danio rerio*; A2ATX7), CNNM2 (*Homo sapiens*; Q9H8M5), CNNM4 (*Homo sapiens*; Q6P4Q7), CNNM4 (*Xenopus tropicalis*; A0JPA0), CNNM1 (*Homo sapiens*; Q9NRU3), CNNM3 (*Homo sapiens*; Q8NE01), UEX (*Drosophila melanogaster*; A0A0B7P9G0), cnnm-1 (*Caenorhabditis elegans*; A3QM97), CBSDUF1 (*Arabidopsis thaliana*; Q67XQ0), MAM3 (*Saccharomyces cerevisiae*; Q12296), CBSDUFCH1 (*Arabidopsis thaliana*; Q9LK65), CorB (*Salmonella typhimurium*; Q8XFY3), yfjD (*Escherichia coli*; P37908), MpfA (*Staphylococcus aureus*; A0A0H3JL60), and yhdP (*Bacillus subtilis*; O07585). Human CNNMs are bolded.

1.2.1 CNNMs are implicated in magnesium homeostasis

There is an abundance of evidence indicating CNNM proteins are involved in mediating divalent cation transport. For example, CNNM1-4 alleles have been shown to strongly associate with serum Mg^{2+} concentrations in a genome-wide association studies (GWAS) [17]. In mice studies, there is upregulation of CNNM2 mRNA in mice kept on a low-Mg^{2+} diet and also kidney cells grown in low Mg^{2+} media, suggesting a role in Mg^{2+} absorption and retention [18, 19]. More convincingly, $CNNM4^{-/-}$ double knockout mice exhibit hypomagnesemia, characterized by low magnesium serum level, indicating these mice have altered magnesium regulation [20]. Under closer examinations, they found higher levels of magnesium in their feces due to malabsorption of intestinal magnesium, suggesting a role in magnesium absorption in the gastrointestinal tract [20]. In addition, when fed a Mg^{2+}-deficient diet, these mice have a higher mortality rate, indicating importance of CNNM proteins in coping with low Mg^{2+}-diets [20]. On the other hand, the $CNNM2^{-/-}$ double knockout die in utero, and heterozygotic $CNNM2^{+/-}$ mice have lower Mg^{2+} serum levels than wild-type mice [21]. Altogether, these results strongly suggest that CNNMs proteins play critical roles in magnesium homeostasis.

1.2.2 Tissue & cellular localization

CNNM1 is only expressed in brain and testis, while other three are ubiquitously expressed with higher expressions in certain tissues [14, 22]. CNNM2 is highly expressed in kidney, brain, and heart [18, 21, 23]. Immunohistochemistry on human kidney sections showed that CNNM2 is predominantly expressed in both distal convoluted tubule (DCT) and thick ascending limb (TAL) of Henle's loop, the two consecutive nephron segments primarily

responsible for Mg^{2+} reabsorption. CNNM3 is highly expressed in kidney, brain, lung, spleen, and heart [24]. CNNM4 shows highest expression in small intestine and colon, where dietary Mg^{2+} absorption occurs [24].

In terms of cellular localization, immunostaining studies of kidney cells have shown that CNNM2 localizes at the basolateral membrane of DCT epithelial cells [19, 21, 24]. Likewise, CNNM4 has been shown to localize at the basolateral membrane of intestinal epithelia [20], and the localization is dependent on AP-1 clathrin adaptor proteins, which recognizes multiple dileucine motifs in the cytosolic domains of CNNM4 [25]. In both intestinal absorption and renal reabsorption, Mg^{2+} entry into the epithelial cells is mediated by apically localized Mg^{2+}-permeable channels, TRPM6/7 [26, 27]. However, the identities of Mg^{2+} transporters involved in Mg^{2+} efflux at the basolateral membrane have remained unknown. Due to their basolateral localization, CNNMs have been proposed to be the long-sought Mg^{2+}-efflux proteins [20].

1.2.3 Mechanism of Mg^{2+} transport by CNNM

In order to understand the molecular mechanism of Mg^{2+} transport by CNNM, several groups have performed transport assays on cells overexpressing CNNMs with mixed conclusions. Here are the studies listed in chronological order.

The first group is Goytain et al. In 2005, they injected mouse CNNM2 cRNA into *Xenopus laevis* oocytes and detected large inward Mg^{2+}-evoked currents with a Michaelis constant of 0.56 mM [18]. The Mg^{2+}-evoked currents were not altered with deletion of external NaCl, arguing against Mg^{2+}-Na^{+} and Mg^{2+}-Cl^{-} coupled transport [18]. They also tested transport of other divalent cations. Mg^{2+}, Co^{2+}, Mn^{2+}, Sr^{2+}, Ba^{2+}, Cu^{2+}, and Fe^{2+} gave appreciable currents while Ca^{2+}, Ni^{2+}, Zn^{2+}, and Cd^{2+} did not, suggesting CNNM2 is a nonselective divalent cation transporter [18].

In 2010, Sponder et al. overexpressed human CNNM2 in a Salmonella strain MM281 missing three major Mg^{2+} influx systems (corA, mgtA, mgtB), which requires high Mg^{2+}-media to proliferate. They found that CNNM2 is able to partly restore the Mg^{2+}-deficient growth phenotype [28]. Using mag-fura-2 fast filter spectroscopy, they detected a large inward-oriented Mg^{2+} influx in CNNM2-expressing cells [28]. They concluded that CNNM2 is a functional Mg^{2+} transporting entity by itself [28].

In 2011, Stuiver et al. performed patch clamp analysis of HEK293 cells transiently transfected with mouse CNNM2, and they detected Mg^{2+}-sensitive Na^+ currents rather than Mg^{2+}-induced currents [19]. Additionally, these Na^+ currents were blocked by increased extracellular Mg^{2+} concentrations (20 mM) as well as addition of 20 mM $ZnSO_4$ [19]. Therefore, the authors suggested CNNM2 might contribute to a Mg^{2+}-sensing mechanism rather than act as a transporter itself [19].

In 2013, Yamazaki et al. performed a series of experiments that proposed CNNMs as Na^+/Mg^{2+} exchangers. They performed elemental analyses of CNNM4-overexpressing HEK293 cells and detected a decrease of Mg^{2+} and an increase of Na^+ levels, without effects on other major metals [20]. Imaging analyses with Magnesium Green, a fluorescent indicator for Mg^{2+} showed that the fluorescent signal in cells expressing CNNM4 rapidly decreased after exchanging bathing solution from 40 mM to 0 mM Mg^{2+}. They concluded CNNM4 is able to stimulate Mg^{2+} extrusion [20]. Performing the same assay with Na^+ replaced by *N*-methyl-D-glucamine (NMDG) abolished the Mg^{2+} efflux, suggesting the efflux is Na^+-dependent [20]. They also performed electrophysiological analyses on CNNM4 or CNNM2-expressed HEK293 cells and found that CNNM4 expression induced no significant electronic currents while CNNM2 expression generated an inward current of Na^+ [20]. Using ratiometric fluorescent probes, sodium-binding benzofuran isophthalate (SBFI) and mag-fura-2, the molar ratio of changes in Na^+ and Mg^{2+} was close to 2:1, suggesting electroneutral exchange of Na^+ and Mg^{2+} by CNNM4 [20].

In 2014, Arjona et al. performed $^{25}Mg^{2+}$ uptake in HEK293 cells transiently transfected with mouse CNNM2 and found that CNNM2-transfected cells displayed a higher $^{25}Mg^{2+}$ uptake compared to control cells [29]. They also found that the CNNM2-dependent $^{25}Mg^{2+}$ uptake was significantly inhibited by addition of 2-APB, an inhibitor of TRPM7 [29]. Additionally, uptake was found to be independent of Na^+ and Cl^- availability and present in assays performed with NMDG or gluconate buffers [29]. These results suggest that CNNM2 is not a Mg^{2+} transporter itself but a regulator of TRPM7 [29].

In 2016, Sponder et al. changed their original stance and claimed that CNNM2 is not a Mg^{2+} transporter by itself, but a Mg^{2+} homeostatic factor. They performed patch-clamp analyses on HEK293 cells overexpressing CNNM2. They were not able to detect constitutive membrane currents above the control, concluding CNNM2 is unable to mediate Na^+ or Mg^{2+} currents [30].

In summary, there are many conflicting conclusions. Some groups suggest CNNMs mediate Mg^{2+} influx, some suggest they mediate efflux, and yet others suggest that they do not mediate transport at all. A debate on this subject with more complete arguments has been published in the *Journal of Physiology* [31-33]. Currently, the field has not come into a consensus on the function of CNNMs.

1.3 CNNM orthologs in other species

In addition to studies on human and mouse CNNMs, there is an abundance of evidence that CNNM orthologs mediate metal handling in species such as zebrafish, roundworm, yeast, and bacteria.

1.3.1 Zebrafish

In zebrafish (*Danio rerio*), there are five CNNM genes. Phylogenetic analysis of CNNM sequences shows that the separation of CNNM paralogs preceded the divergence of boney fish and tetrapods. In addition to Cnnm1, Cnnm3, and Cnnm4, there are two distinct zebrafish CNNM2 orthologs, Cnnm2a and Cnnm2b. Their amino acid sequence identity with human CNNM2 is 79% [34]. Cnnm2a and Cnnm2b were ubiquitously expressed in all adult zebrafish tissues. Cnnm2a was most abundantly found in the brain and ovary; and Cnnm2b found in the gut, brain, and testis [34]. In the gut of fish fed a Mg^{2+}-deficient diet, both Cnnm2a and Cnnm2b expression levels showed significant upregulation [34]. Knockdown of both CNNM2 orthologs in zebrafish resulted in impaired development of the brain with abnormal altered locomotor and touch-evoke escape behaviors, and Mg^{2+} wasting. These phenotypes could be rescued by injection of mouse CNNM2 cRNA, demonstrating the functional complementation between mammalian CNNM2 and the zebrafish orthologs [29].

1.3.2 Roundworm

In *C. elegans*, there are five CNNM orthologs (CNNM-1 to CNNM-5); each sharing significant identity with human proteins (24 - 47%) [35]. Mutational studies showed that worms missing both CNNM-1 and CNNM-3 were smaller in size, had shorter lifespan, and were sterile. The sterility phenotype could be rescued by Mg^{2+} supplementation [35]. Further studies indicated that the sterility was caused by gonadogenesis defect [35]. The sterility could be restored by inactivation of aak-2, which encodes α-subunit of AMP-activated protein kinase (AMPK) [35].

1.3.3 Yeast

In studies of bakers' yeast (*Saccharomyces cerevisiae*), MAM3 gene deletions confer high levels of manganese resistance as well as increased resistance to zinc and cobalt [36].

MAM3 gene encodes Mam3p, a CNNM ortholog with 39% sequence identity to human CNNM2. Studies showed that yeast Mam3p functions at the site of the vacuolar membrane and affects manganese toxicity through a mechanism that does not involve vacuolar sequestration of the metal or the manganese homeostasis pathways mediated by Pho84p, Pmr1p or Smf2p [36]. The role of Mam3p in manganese metabolism appears unique and the exact mechanism is still unknown.

1.3.4 Bacteria

In 1986, characterization of cobalt resistant mutants in *Salmonella typhimurium* by the group of Michael E. Maguire first identified CorA, the major Mg^{2+} uptake system in prokaryotes [37]. In 1991, the same group additionally identified three genes from cobalt resistant mutant screening called corB, corC, and corD. CorB is the CNNM ortholog in *S. typhimurium*. The authors found that although CorA alone is necessary and sufficient for influx of Mg^{2+}, efflux requires the presence of a co-effector, either CorB, CorC, or CorD. Mutation of CorB, CorC, and CorD individually or in combination markedly reduced the ability of extracellular Mg^{2+} to elicit efflux via CorA [38].

Studies in *Staphylococcus aureus* identified a CNNM ortholog called MpfA (magnesium protection factor A). MpfA deletion mutants are unable to grow in the presence of high concentrations of magnesium [39]. Complementation by MpfA-containing plasmids can reverse these phenotypes, indicating perturbation of magnesium homeostasis [39]. Using a Mg^{2+}-sensing riboswitch, the authors showed that loss of MpfA results in an increase of internal magnesium concentrations consistent with MpfA acting as a Mg^{2+} exporter itself or promoting Mg^{2+} export via another protein [40]. The ΔMpfA mutants also showed moderate resistant to cobalt and manganese which the authors attributed to increased competition for Co^{2+} and Mn^{2+} binding sites by intracellular Mg^{2+} [39].

1.4 CNNM – disease relevance

CNNMs are associated with a myriad of genetic diseases linked to abnormal Mg^{2+} handling, such as hypomagnesemia, Jalili syndrome, cancer, hypertension, infertility, and schizophrenia.

1.4.1 Hypomagnesemia

Mutations in CNNM2 were first identified in patients with dominant hypomagnesemia in two families (**Table 1.1**). The patients suffered from muscle weakness, tremor, and headaches accompanied by low Mg^{2+} serum concentrations (0.3-0.5 mM) [19]. Analysis of the heterozygous missense mutation T568I shows that the mutant protein was properly localized to the plasma membrane but caused a significant decrease in CNNM2 activity in Mg^{2+}-sensitive Na^{+} currents [19] and Mg^{2+} efflux activity [41]. In 2014, Arjona et al. identified new mutations in CNNM2 in five unrelated families suffering from hypomagnesemia with cerebral seizures, mental retardation, and brain malformations [29]. In the first family, the patients had a homozygous missense mutation of E122K inherited recessively [29]. The four remaining cases consisted of dominant, *de novo* heterozygous mutations: S269W, L330F, or E357K [29]. All of these mutants except for L330F exhibited severely reduced $^{25}Mg^{2+}$ uptake, possibly due to destabilization of CNNM2. The E112K and S269W mutants showed reduced plasma membrane expression [29]. Recently, two papers identified additional mutations associated with hypomagnesemia in the CNNM2 cytosolic domains [42, 43]. Together with the finding that knockdown of CNNM2 orthologs in zebrafish resulted in impaired brain development and reduced body Mg^{2+} content [29], these results demonstrate a strong link between CNNM2-induced hypomagnesemia and brain development.

Table 1.1 Disease-associated mutations in CNNM proteins

Disease	Protein	Location	Missense mutations	Nonsense mutations	References
Hypomagnesemia	CNNM2	Extracellular	E122K	I40Sfs*15	[19, 29]
		Transmembrane	S269W, L330F, E357K	-	[29]
		CBS-pair	V548M, T568I	-	[19, 42]
		CNBH	-	S795*	[43]
Jalili syndrome	CNNM4	Extracellular	-	L21Hfs*185, D63Efs*12, F93Lfs*31	[44-46]
		Transmembrane	S196P, S200Y, R236Q, R236W, S245L, L324P	I232Pfs*80, A300Cfs*22	[44, 45, 47-51]
		CBS-pair	R407L, P409L, G492C, T495I, V499M	G364Vfs*9, L438Sfs*41, L438Pfs*9	[44, 45, 50, 52-56]
		CNBH	N594S	R519*, Q564*, Y581*, R605*, Q717*	[44, 45, 50, 51, 57-59]
Schizophrenia	CNNM1	CBS-pair	H528Y	-	[60]
	CNNM3	CNBH	Y628D	-	[60]
	CNNM4	Transmembrane	G249R	-	[60]

1.4.2 Jalili syndrome

A large number of mutations in CNNM4 are associated with Jalili syndrome, a rare disease characterized by recessively inherited amelogenesis imperfecta and cone-rod dystrophy (**Table 1.1**) [61]. Amelogenesis imperfecta is caused by defects in dental enamel formation, which negatively affects the structure, composition, and thickness of both primary and secondary teeth, causing unusually small, discolored, pitted or grooved teeth [62]. Cone-rod dystrophy is characterized by dysfunction of cone receptors, which results in reduced central visual acuity, photophobia, and loss of color vision [63]. Defects in amelogenesis were also observed in CNNM4$^{-/-}$ knockout mice, in which levels of both calcium and phosphorus in the incisors were significantly decreased, confirming the occurrence of hypomineralization [20]. Immunohistochemical staining showed CNNM4 localization to the basolateral membrane of ameloblasts, the enamel-forming epithelial cells [20]. Mg^{2+} efflux assays on two Jalili syndrome-

associated mutations (S200Y and L324P) showed abolishment of Mg^{2+} efflux activity by both mutants, suggesting dysfunction of Mg^{2+} extrusion probably underlies this rare disease [20]. However, the precise role of Mg^{2+} in the enamel-forming process remains unknown, although there has been reports that the magnesium content of the enamel is inversely correlated with the extent of mineralization [64].

1.4.3 Cancer

CNNM4 has been shown to act as a tumor suppressor in a mouse model of colon cancer. Knockdown of CNNM4 significantly augmented the number of tumor nodules on the mice lungs, confirming the tumor-suppressing role of endogenous CNNM4 [65]. In addition, in $Apc^{\Delta/14+}$ mice, which spontaneously form benign polyps in the intestine, deletion of CNNM4 promoted malignant progression of intestinal polyps to adenocarcinomas [65]. CNNM4 mRNA levels in colon cancer were significantly reduced, and this reduction was more evident in metastatic colon cancer than non-metastatic ones, implicating CNNM4 down-regulation in human colon cancer development [65].

Two groups independently identified an interaction between CNNM proteins and phosphatases of regenerating liver (PRLs), a family of potent oncogenes frequently overexpressed in malignant human cancers [65, 66]. Both groups found that CNNM-PRL interaction promoted oncogenesis and disruption of interaction abolished tumor progression [65, 67]. Mechanistically, the two groups proposed different mechanisms but with the same downstream effect. Funato et al. postulated that CNNM4 mediates Mg^{2+} efflux with PRL3 inhibiting CNNM4 activity and increasing intracellular Mg^{2+} [65]. In contrast, Hardy et al. postulated that CNNM3 mediates Mg^{2+} influx with PRL2 enhancing influx activity to again increase intracellular Mg^{2+} levels [66]. Both groups suggested that increased binding of Mg^{2+} to ATP would promote the activity of enzymes associated with energy metabolism and protein synthesis, thereby promoting cellular proliferation and tumor invasiveness [68-71].

1.4.4 Hypertension

Several genome-wide association studies have identified CNNM2 as a candidate gene associated with blood pressure variation and hypertension [72-76]. Studies of CNNM2 and CNNM4 knockdown mice suggested opposing roles of CNNM proteins on blood pressure:

CNNM2$^{+/-}$ mice had lower blood pressure, while CNNM4$^{-/-}$ mice had increased blood pressure [21]. The authors proposed the following explanation: CNNM2 is involved in renal absorption of Mg^{2+}, and when CNNM2 expression is knocked down, it leads to impaired activity of renal reabsorption, thus leading to lower blood pressure [21]. On the other hand, knockdown of CNNM4 results in lower intestinal Mg^{2+} absorption and lower serum magnesium level. This in turn upregulates renal Mg^{2+} reabsorption by CNNM2, and the increased renal activity leads to increased blood pressure [21].

1.4.5 Infertility

Evidence of CNNM involvement in infertility comes from CNNM knockout studies in *C. elegans* and mice. In *C. elegans*, CNNM-1 and CNNM-3 double mutant worms were sterile due to gonadogenesis defect that severely attenuated proliferation of germ cells [35]. In mice, CNNM4$^{-/-}$ males are almost infertile because of loss of sperm mobility and fertility [77]. Detailed analyses of these sperm revealed that their lack of hyperactivation motility is due to defects in activation of CatSper, a sperm-specific Ca^{2+} channel required for hyperactivation [77]. These sperm also showed higher levels of magnesium, in which excessive Mg^{2+} accumulation was considered to impair the CatSper Ca^{2+} channel function, suggesting a functional relationship between Mg^{2+} homeostasis and Ca^{2+} signaling [77]. In addition, Cnnm2$^{+/-}$ Cnnm4$^{-/-}$ mice were infertile, and their sperm showed a more severe motility-defective phenotype than those from Cnnm4$^{-/-}$ mice, thus also implicating the role of CNNM2 in sperm motility [78].

1.4.6 Schizophrenia

Many genome-wide association studies have identified CNNM2 as a risk locus for schizophrenia [79-83]. A study found that a CNNM2 SNP variant (rs7914558; located within an intron) is associated with grey matter morphological vulnerability of the bilateral inferior frontal gyri, which may represent the mechanism by which CNNM2 increases the risk for schizophrenia [84]. Rose et al. also investigated the effect of CNNM2 rs7914558 variant and showed that this variant has an effect on both social cognition (i.e. attributional style) and grey matter volume in regions previously implicated in the processing of social stimuli [85]. Large-scale phenotypic landscape characterization of schizophrenia-association genes in zebrafish also identified CNNM2 as a promising candidate for the disease; CNNM2 mutants caused decreased brain

activity in retinal arborization field, tectum, and hypothalamus [86]. Together with previous findings mutations in CNNM2 results in hypomagnesemia and impaired brain development [29], these studies strongly suggest that CNNM2 plays important roles in brain development and pathophysiological of schizophrenia. In addition, genome sequencing of individuals affected with schizophrenia have identified missense mutations in CNNM1, CNNM3, and CNNM4, thereby linking all four members to schizophrenia (**Table 1.1**) [60]. Recently, two studies in flies have implicated the CNNM ortholog, Uex, in brain development and function. Prl-1, which acts upstream of Uex, was shown to be required for proper synapse formation and fly movement [87]. Prl-1 and Uex were also found to play neuroprotective roles. Loss of either Uex or Prl-1 led to neural dysfunction characterized by a wing up phenotype upon CO_2 exposure [88].

1.5 CNNM – domain organization and structure

CNNMs are multi-domain proteins. Eukaryotic CNNMs contain four domains: the extracellular domain, transmembrane domain (TMD), CBS-pair domain, and cyclic nucleotide-binding homology (CNBH) domain (**Fig. 1.2**). The transmembrane and CBS-pair domains are the most conserved domains and found associated together in essentially all organisms from humans down to bacteria. Prokaryotic CNNMs lack the extracellular domain and have a smaller C-terminal domain, termed CorC, that is unrelated to the eukaryotic CNBH domain.

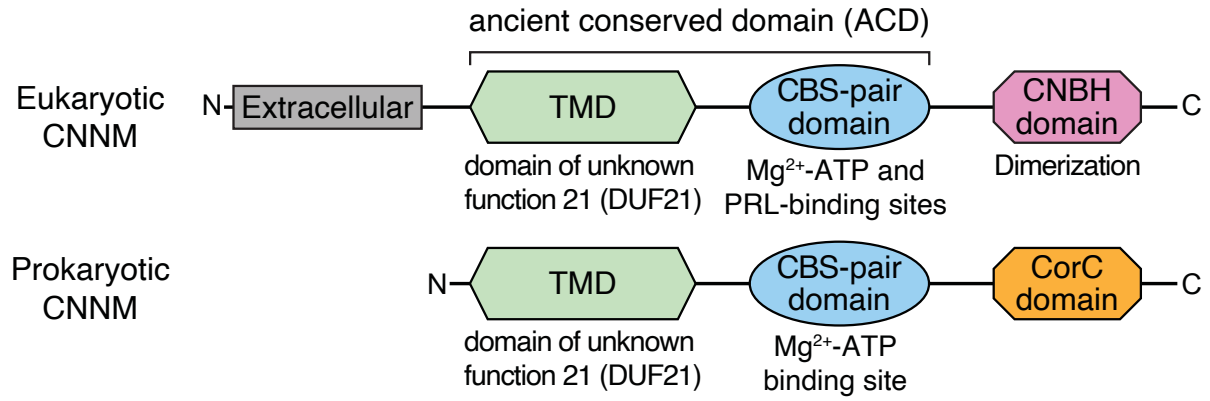

Figure 1.2 Domain architecture of eukaryotic and prokaryotic CNNMs

---

1.5.1 Extracellular domain

Based on sequence analysis, all four human CNNMs contain a signal peptide prior to the N-terminal extracellular domain [89]. In CNNM2, the signal peptide has been experimentally determined to be 64 amino acid long and is cleaved by signal peptidase complex (SPC) in the ER [24]. The structure and function of the extracellular domain is unknown. de Baaij et al. identified a glycosylation site in CNNM2 at Asn-112 [24]. Mutation of Asn-112 to alanine resulted in 90% reduction in plasma membrane expression, suggesting glycosylation is necessary for localization or protein stability [24]. The domain is the site of a hypomagnesemia-associated mutation (CNNM2 E122K) that similarly reduces in plasma membrane expression [29].

1.5.2 Transmembrane domain (TMD)

The transmembrane domain is the defining feature of CNNM proteins. The domain is very broadly conserved and constitutes the largest family of protein domains of unknown function (DUFs) on the Pfam database [90]. Called domain of unknown function 21 (DUF21), there are close to 20,000 protein sequences from over 7,000 species ranging from bacteria to plants and animals. Transmembrane prediction software predicts four transmembrane helices. However, since the preceding domain is extracellular and following domain is intracellular, it must have an odd number of transmembrane sequences. Thus, De Baaij et al. has predicted the DUF21 to be composed of three transmembrane helices and one re-entrant helix [24]. They predicted the second helix to be the re-entrant helix since it is the shortest and the least hydrophobic (**Fig. 1.3**) [24]. Several Jalili syndrome mutations reside in this domain of CNNM4, such as S196P, S200Y, R236Q, R236W, S245L, and L324P [44, 48-51] (**Table 1.1**). Mg^{2+} efflux studies on S200Y and L324P mutants in CNNM4 showed diminished efflux activity [20]. In addition, several hypomagnesemia-associated mutations also reside in DUF21 of CNNM2: S269W, L330F, and E357K [29].

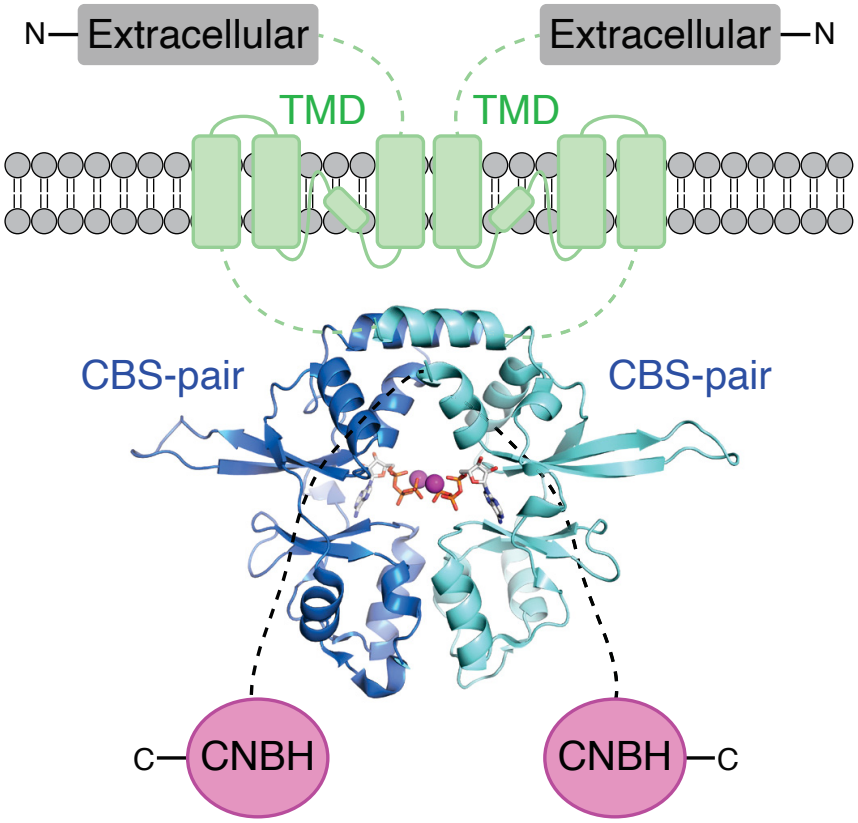

Figure 1.3 Topological model of CNNM proteins

Prior to this thesis, the only structures of eukaryotic CNNM protein known were fragments comprising the CBS-pair domain. The CNNM TMD is predicted to consist of three transmembrane helices and 1 re-entrant helix. The structure of CBS-pair domain shown (PDB: 4P1O [91]) crystallized as a dimer with two Mg^{2+}-ATP bound in the central cavity. CNNMs are predicted to be dimers due to dimerization of the CBS-pair domains.

1.5.3 CBS-pair domain

The TMD is followed by a cytosolic domain called cystathionine-β-synthase (CBS)-pair domain (**Fig. 1.3**). CBS-pair domains, also known as Bateman modules, consist of two repeated 60-residue CBS motifs that fold together. CBS-pair domains are found in many proteins: AMP-activated protein kinase (AMPK), inosine-5′-monophophate dehydrogenase (IMPDH), chloride channel (ClC), and bacterial Mg^{2+} transporter MgtE [92, 93]. In AMPK, this domain acts as an energy sensor as it is able to bind different adenine nucleotides, such as AMP, ADP, and ATP

[94]. In CNNM, this domain also binds ATP and is also the site of PRL binding. This domain has been characterized most extensively and is the only CNNM domain with a known structure prior to this thesis.

1.5.3.1 CNNM CBS-pair domains bind ATP

Hirata et al. measured the affinity of ATP to CBS-pair domain of CNNM1-4 using a [^{32}P]ATP filter binding assay (**Table 1.2**) [41]. They observed that the CBS-pair domains of CNNM2 and CNNM4 bound ATP in a Mg^{2+}-dependent manner (10 mM Mg^{2+}). The domains of CNNM1 and CNNM3 showed negligible binding [41]. The affinities of ATP binding to CNNM2 and CNNM4 are considerably lower than the ATP concentration found in the cells (1-2 mM) [95], which led the authors to conclude that ATP is constitutively bound irrespective of the energetic state of the cells [41].

Table 1.2 Binding affinities of CBS-pair domains for ATP [41].

CBS-pair domain	ATP (μM)	Mg^{2+}-ATP (μM)
CNNM1	No binding	915 ± 389
CNNM2	No binding	159 ± 28
CNNM3	No binding	No binding
CNNM4	No binding	43.4 ± 8.9

1.5.3.2 Crystal structures of CBS-pair domain

In order to characterize the structural basis of ATP binding, Corral-Rodriguez et al. determined crystal structures of the CNNM2 CBS-pair domain without ligand and in complex with different adenine nucleotides. The CBS-pair domain is made up of two consecutive CBS motifs (CBS1 and CBS2) that fold together (**Fig. 1.4**) [91]. Both CBS motifs adopt βαββα folds and contact each other via three-stranded β-sheets (where the first two β strands run parallel, the third one runs antiparallel) [91]. The CBS-pair domain exists as a dimer in which two CBS-pair domains associate to form a disk, commonly referred to as a CBS module. The dimer of CBS-pair domains binds nucleotides and metal ions in the central cavity [91].

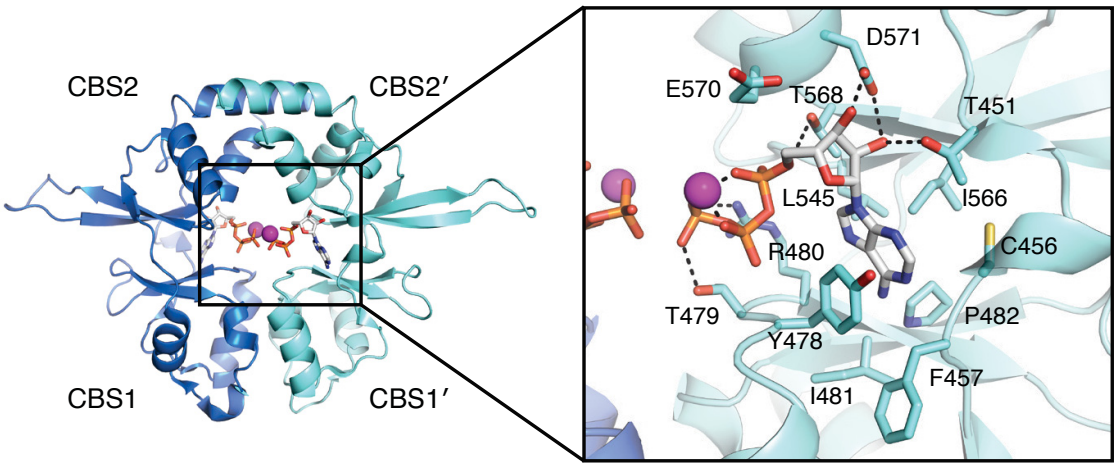

Figure 1.4 Structural basis of Mg^{2+}-ATP binding by CBS-pair domain

Crystal structure of CNNM2 CBS-pair domain bound to Mg^{2+}-ATP (PDB: 4P1O [91]). ATP binds to the canonical nucleotide-binding site. Mg^{2+} ions are represented as magenta spheres.

In the three structures, CBS-pair domain of CNNM2 binds adenine nucleotides (AMP, ADP, or Mg^{2+}-ATP) in the central cavity (**Fig. 1.4**). In the Mg^{2+}-ATP-bound structure, the adenine ring is sandwiched between Tyr478 and Ile566 in a hydrophobic pocket comprising Pro482, Ile481, Cys456, and Phe457, while the ribose ring forms hydrogen bonds with the side chains of Thr451 and Asp571 [91]. For the phosphate groups, the α-phosphate is stabilized by Thr568. When present, the β-phosphate and/or γ-phosphate are hydrogen-bonded by Thr479 and Arg480 [91]. In hypomagnesemia patients, this Thr568 residue is mutated to a bulkier isoleucine residue, consequently causing steric clashing with the ribose moiety, thus inhibiting adenine nucleotide binding [19]. In the Mg^{2+}-ATP-bound structure, the Mg^{2+} is coordinated by all three phosphates and is considered an allosteric activator for ATP binding as Mg^{2+} binding alleviates the otherwise negative charge repulsion existing between acidic residues and phosphate groups of ATP [91].

Additionally, Corral-Rodriguez et al. obtained the CBS-pair domain structure of CNNM2 in an unliganded form. In absence of bound nucleotide, the dimer adopts a twisted conformation, in which both CBS2 motifs remain in contact while CBS1 motifs have separated (**Fig. 1.5**) [91]. In addition, the monomers differ markedly in the relative orientation of helix α0 that leads to the TMD and helix α4 that connects to the following CNBH domain. These changes suggest that the

movements induced by nucleotide binding could be translated to the two neighboring domains [91].

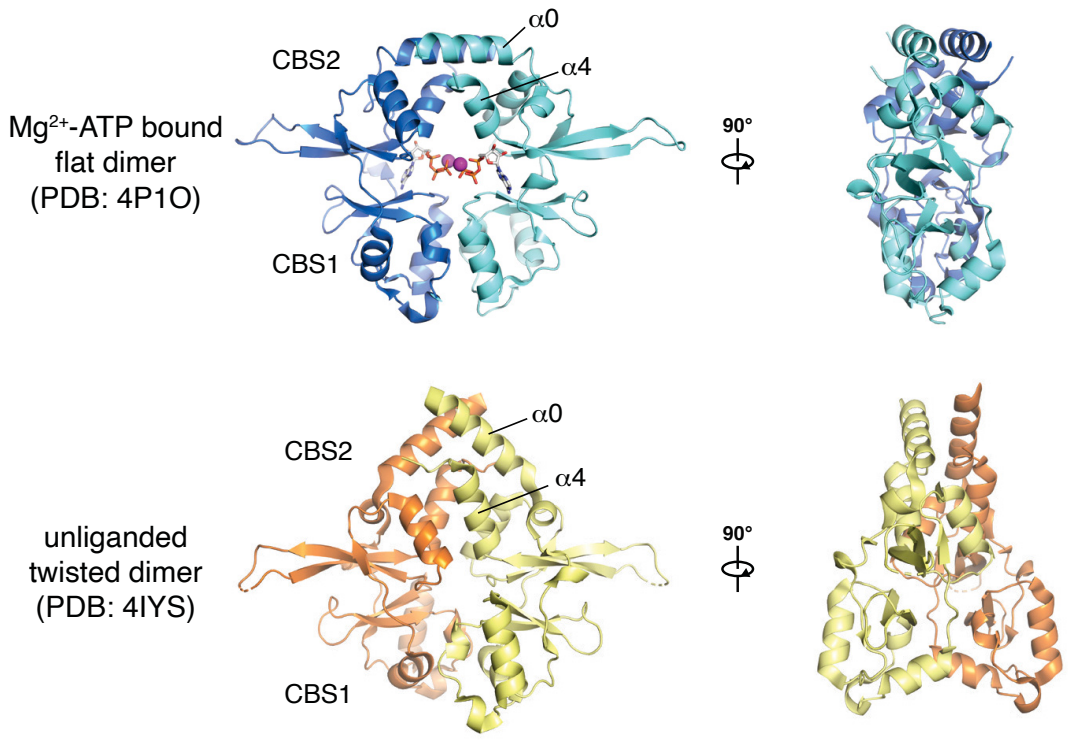

Figure 1.5 CBS module adopts different conformations depending on Mg^{2+}-ATP binding
In presence of Mg^{2+}-ATP, the CNNM2 CBS-pair domain adopts a flat, disc-like dimer (PDB: 4P1O [91]). Without ligand, the domain forms a twisted shape similar to a lock washer (PDB: 4IYS [91]). The alpha helices, α0 and α4, that connect to neighboring domains undergo major conformational rearrangements.

1.5.3.3 Co-crystal structures of CBS-pair domain and PRL

Our group reported the first co-crystal structure of a CBS-pair domain (CNNM3) and phosphatase (PRL2) [96]. Additional structures of CNNM2 and CNNM3 with different PRL proteins were subsequently reported [97, 98]. In the structures, the CBS-pair domain is always present as a flat disc-like dimer, similar to the nucleotide-bound conformation. The complexes are very similar. The CBS-pair domain interacts with PRL using the extend loop that connects β5

and β6 (**Fig. 1.6**). The extended size of the loop is unique to CNNMs and absent in other CBS domain-containing proteins. PRL binding is mainly mediated by an aspartic acid (Asp558 in CNNM2; Asp426 in CNNM3) in the CBS-pair domain that inserts into the catalytic pocket of PRL mimicking a phosphorylated substrate. The interaction is abolished by phosphorylation or oxidation of the catalytic cysteine in PRL (e.g. Cys101 in PRL2), suggesting additional layers of regulation.

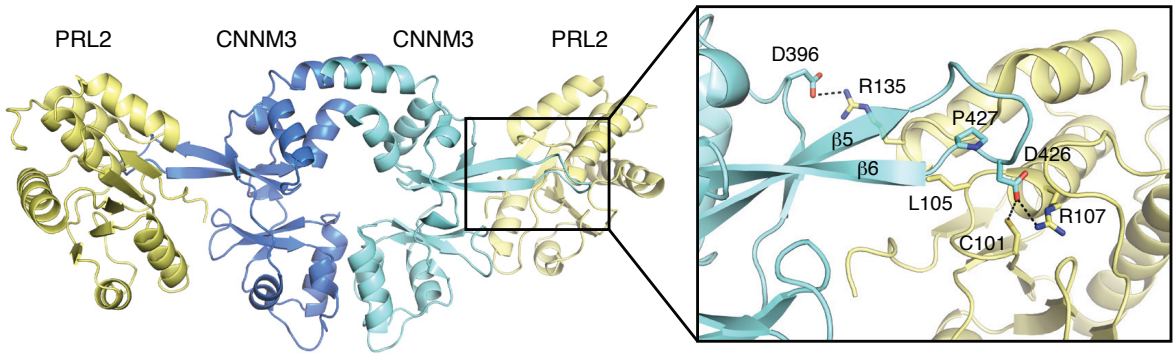

Figure 1.6 Structural basis of CNNM-PRL interaction

Crystal structure of CNNM3 CBS-pair domain in complex with PRL2 (PDB: 5K22 [96]). The interaction is mediated by the extended loop structure from CNNM into the catalytic pocket of PRL.

1.5.3.4 CBS-pair domain of bacterial CNNMs

Several bacterial CNNM orthologs have had their CBS-pair domain structures determined (PDB: 3LV9; 3LHH; 3OCO; 3HF7; 3I8N). The structures resemble those of human CNNMs with the exception of the extended loop that is only present in higher eukaryotes. Some of the bacterial proteins have been crystallized in presence of adenine nucleotides and form dimers.

1.5.4 Cyclic nucleotide-binding homology domain

Eukaryotic CNNMs contain a cyclic nucleotide-binding homology (CNBH) domain after the CBS-pair domain. Little is known about this domain other than its sequence similarity to

cyclic nucleotide-binding (CNB) domains [14]. The CNBH domains of CNNMs are well-conserved across isoforms with the exception of a large variable loop. The similarity to CNB domains suggested that CNNMs could be regulated by cyclic nucleotide binding. The CNBH domain does not interact with CBS-pair domain, nor does it interact with PRLs [98]. Several mutations in the domain has been linked to Jalili syndrome (**Table 1.1**).

1.5.5 CorC domain

In prokaryotes, instead of CNBH domain, the CBS-pair domain is followed by a smaller C-terminal domain called CorC domain. Structures from several CNNM orthologs have been determined (PDB: 2OAI; 2R8D; 2NQW; 3DED; 2P3H; 2PLS; 2RK5). The domain is made up of a five-stranded anti-parallel β-roll and two α-helices. Structure of full-length CorC (PDB: 4HG0), a bacterial CNNM ortholog that lacks the DUF21, has been determined in complex with AMP (**Fig. 1.7**). The CBS-pair domain forms a dimer while the CorC domain hangs on opposite sides, most likely representing the structure of cytosolic region of prokaryotic CNNMs.

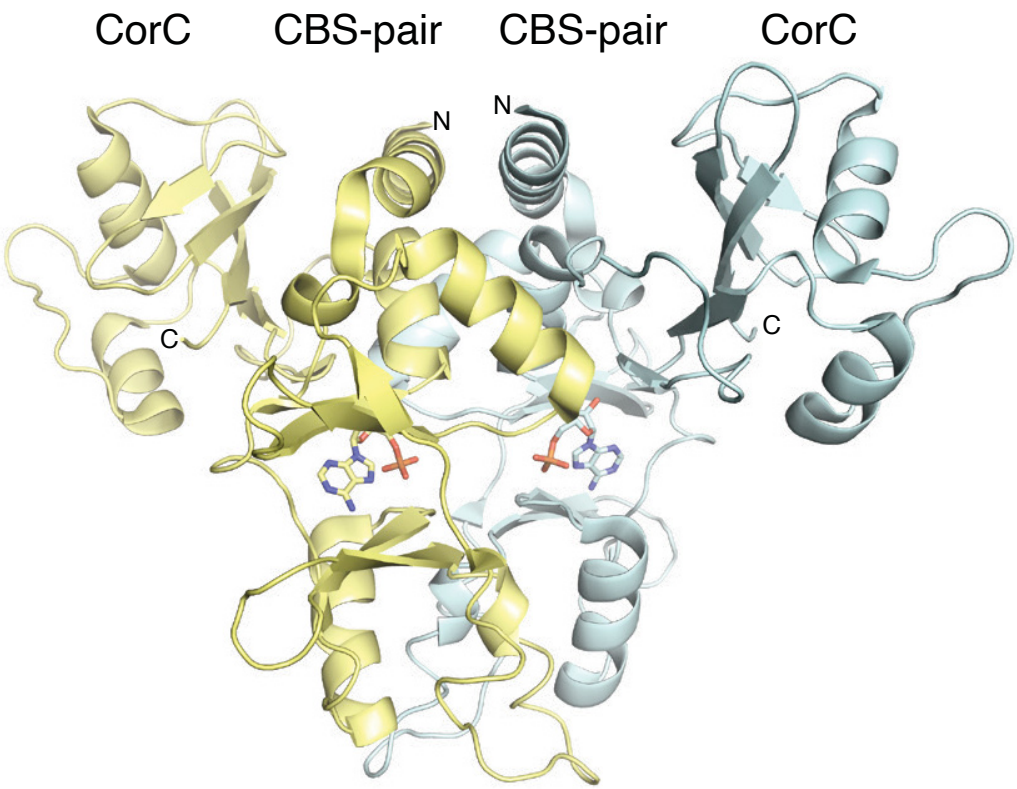

Figure 1.7 Crystal structure of CorC, a bacterial CNNM ortholog that lacks TMD
The CBS-pair domains of CorC bind AMP in the central cavity forming a flat, disc-like homodimer while CorC domains resides on either side of CBS-pair domains (PDB: 4HG0).

1.5.6 Oligomerization state

Since all the CBS-pair domain structures are dimers, it suggests that the oligomerization state of CNNMs is a dimer. Indeed, additional complexes have been observed on immunoblots at ~200 kDa (monomer = 105 kDa), suggesting the functional unit is a dimer [24]. Assuming CNNM forms a dimer, then there would be six transmembrane helices, which is thought to be too few for a transporter [24]. Therefore, some groups suggest CNNM2 might function as a sensor indirectly regulating Mg^{2+} transport instead of performing direct transport [24].

1.6 Thesis objectives and overview

Seventeen years since the discovery of CNNM proteins, the mechanism of Mg^{2+} transport by CNNM remains unknown and actively debated. Is it a direct transporter or a regulator of other transporters? If direct transport, what is the mechanism? Does it form a continuous pore or act as a secondary transporter? Is the transport voltage-dependent, ligand-gated, ATP-driven, or cyclic nucleotide-gated? Prior to this work, only the CBS-pair domain of CNNM proteins had been studied functionally and structurally.

In this thesis, I describe a stepwise structural approach to understand the function and mechanism of Mg^{2+} transport by CNNM proteins. In Chapter 2, I characterized the uncharacterized C-terminal CNBH domain and observed that the domain functions as a dimerization domain and is important for Mg^{2+} efflux. In Chapter 3, I studied the structures of the two cytosolic domains (CBS-pair and CNBH domains) and found that Mg^{2+} efflux function is regulated by conformational changes associated with Mg^{2+}-ATP binding to the CBS-pair domain. Lastly, in Chapter 4, I solved the structure of an archaeal CNNM ortholog by X-ray crystallography. The structure of the transmembrane domain shows a dimeric configuration with negatively charged cavity consistent with a direct function of CNNM in ion transport. To test this, I reconstituted the purified archaeal protein in vesicles and measured Mg^{2+} transport. The results of this work are an improved understanding of the three-dimensional structures and biochemical functions of CNNMs.

Chapter 2 – The cyclic nucleotide–binding homology domain of the integral membrane protein CNNM mediates dimerization and is required for Mg^{2+} efflux activity

Chen, Y. S., Kozlov, G., Fakih, R., Funato, Y., Miki, H., and Gehring, K. (2018). *Journal of Biological Chemistry* **293**, 19998-20007.

2.0 Connecting text

The presence of cyclic nucleotide-binding homology (CNBH) domain suggests CNNM could be regulated by cyclic nucleotides. In this chapter, I carry out structural and functional characterization of the C-terminal CNBH domain to learn about this domain.

2.1 Summary

Proteins of the cyclin M family (CNNMs; also called ancient conserved domain proteins, or ACDPs) are represented by four integral membrane proteins that have been proposed to function as Mg^{2+} transporters. CNNMs are associated with a number of genetic diseases affecting ion movement and cancer via their association with highly oncogenic phosphatases of regenerating liver (PRLs). Structurally, CNNMs contain an N-terminal extracellular domain, a transmembrane domain (DUF21), and a large cytosolic region containing a cystathionine-β-synthase (CBS) domain and a putative cyclic nucleotide–binding homology (CNBH) domain. Although the CBS domain has been extensively characterized, little is known about the CNBH domain. Here, we determined the first crystal structures of the CNBH domains of CNNM2 and CNNM3 at 2.6 and 1.9 Å resolutions. Contrary to expectation, these domains did not bind cyclic nucleotides, but mediated dimerization both in crystals and in solution. Analytical ultracentrifugation experiments revealed an inverse correlation between the propensity of the CNBH domains to dimerize and the ability of CNNMs to mediate Mg^{2+} efflux. CNBH domains from active family members were observed as both dimers and monomers, whereas the inactive member, CNNM3, was observed only as a dimer. Mutational analysis revealed that the CNBH domain was required for Mg^{2+} efflux activity of CNNM4. This work provides a structural basis for understanding the function of CNNM proteins in Mg^{2+} transport and associated diseases.

2.2 Introduction

Magnesium (Mg^{2+}) is the most abundant divalent cation inside cells and essential for a wide variety of biochemical processes, such as energy metabolism, maintenance of genomic stability, protein synthesis, and over 600 enzymatic reactions [2]. In humans, abnormal Mg^{2+} handling is linked to different pathologies, including osteoporosis, diabetes, hypertension, neurological disorders, and immunodeficiency [7, 8]. Mg^{2+} is unique among divalent cations in that it has the smallest ionic radius and largest hydrated radius; therefore, the transport of Mg^{2+} across the membrane requires the action of Mg^{2+} channels and transporters, including CNNM proteins [6].

Originally called cyclin M due to specious sequence similarity with the cyclin family, CNNMs are a conserved family of four integral membrane proteins implicated in maintaining Mg^{2+} homeostasis [14]. CNNM2 and CNNM4 possess Mg^{2+} efflux activity and have been proposed to facilitate renal/intestinal (re)absorption of Mg^{2+} as they localize to the basolateral membrane of renal/intestinal epithelial cells [19, 20]. *CNNM* mutations are associated with a number of genetic diseases affecting Mg^{2+} homeostasis. Mutations in *CNNM2* were found in patients with familial dominant hypomagnesemia accompanied by low Mg^{2+} serum level and symptoms such as muscle weakness, tremor, and headaches [19]. Mutations in *CNNM4* are implicated in Jalili syndrome, characterized by recessive amelogenesis imperfecta and cone-rod dystrophy [44, 48].

More recently, CNNM-associated Mg^{2+} transport was found to be regulated by the binding of phosphatases of regenerating liver (PRLs), which are potent oncogenes with strong association with metastatic cancers [99]. When PRL binds CNNM, intracellular Mg^{2+} level is increased, thereby promoting tumor progression and cellular proliferation [65, 66]. Despite a clear association with Mg^{2+} transport, it is still debated whether CNNM proteins are themselves Mg^{2+} transporters or whether they regulate other proteins that transport Mg^{2+} [31, 32].

Structurally, CNNMs contain an N-terminal extracellular domain, a transmembrane domain (domain of unknown function 21; DUF21), and a large cytosolic region containing a cystathionine-β-synthase (CBS-pair) domain and a cyclic nucleotide–binding homology (CNBH) domain (**Fig. 2.1A**) [24]. Currently, only the CBS-pair domains have been characterized structurally. The CBS-pair domain is the site of PRL binding [96-98] and required for Mg^{2+} efflux [41]. The CBS-pair domains dimerize and are likely a site of regulation through

ATP-Mg^{2+} binding. Nucleotide binding induces a conformational change of the dimer from a twisted to a flat disc-like structure [91].

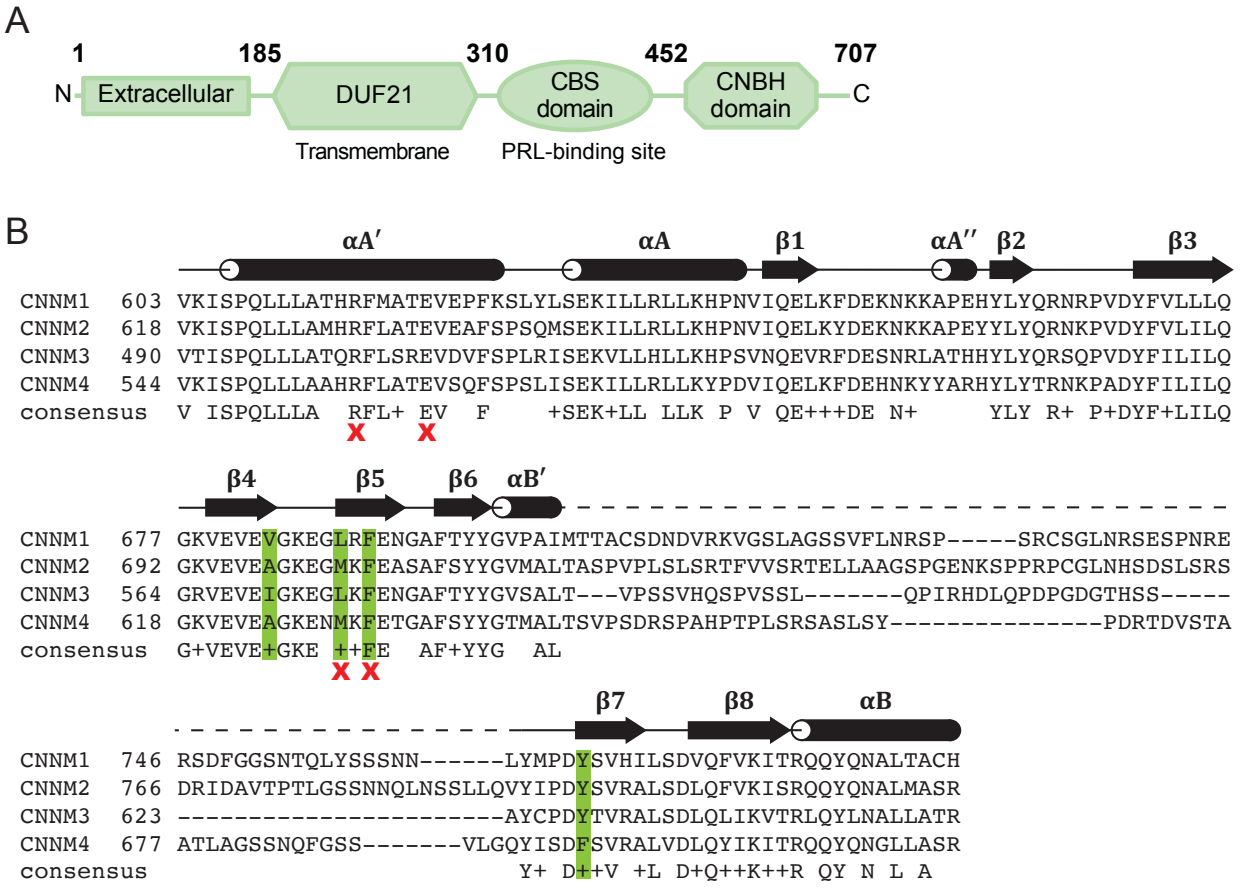

Figure 2.1 CNNM domain organization

(A) CNNM consists of four domains: the extracellular domain, DUF21, CBS domain, and CNBH domain. Residues are *numbered* according to CNNM3. (B) Sequence alignment of CNBH domains of human CNNM proteins. Secondary structure corresponds to the crystal structure of the CNNM3 CNBH domain. The *dashed line* corresponds to a disordered region that was not observed in the electron density map. Hydrophobic residues involved in the dimerization interface are *highlighted* in *green*. Positions tested by mutagenesis for dimerization or efflux activity are marked by a *red X*.

Whereas CBS-pair domains have been extensively characterized, little is known about the CNNM C termini other than the sequence similarity to cyclic nucleotide–binding domains [14].

The CNBH domains of CNNMs are well-conserved across isoforms with the exception of a large variable loop (**Fig. 2.1B**). The similarity to cyclic nucleotide–binding domains suggested that CNNMs could be regulated by cyclic nucleotide binding. The CNBH domain does not interact with CBS-pair domain; nor does it interact with PRLs [98]. One mutation in the domain has been linked to Jalili syndrome [57].

Here, we carried out structural and functional characterization of the CNBH domain of CNNM. We determined the structures of CNBH domains from CNNM2 and CNNM3. We found that, contrary to expectations, the CNBH domains do not bind cyclic nucleotides. Rather, the domains exist as dimers both in the crystal and in solution. Efflux measurements with CNBH mutants showed that deletion of the CNNM4 CNBH domain abrogated activity in an Mg^{2+} efflux assay but that the dimerization was not required. Our results suggest that CNBH dimerization may function to inhibit and thus regulate CNNM activity across the different isoforms.

2.3 Results

2.3.1 Structural determination of CNBH domain of CNNM3 and CNNM2

To gain insight into CNNM proteins, we endeavored to determine the three-dimensional structures of their CNBH domains. We first obtained crystals of the CNBH domain from human CNNM3 (residues 453–707) that diffracted to ~3 Å. Attempts to solve the structure by molecular replacement were unsuccessful; thus, we chose to label the protein with selenomethionine for experimental phasing. This required the introduction of additional methionine residues by site-directed mutagenesis, as there is only one methionine in the CNNM3 CNBH domain and its location was predicted to be in a mobile region. Seven sites (Ile-516, Arg-535, Thr-591, Ala-623, Leu-651, Val-669, and Ile-670) were selected based on the sequence alignment of CNNM proteins from different species. Mutants with three or more additional methionines were screened for expression and solubility. Several mutants produced a significant amount of soluble protein, but the best-diffracting crystals were obtained with a mutant with six artificially introduced methionines (**Fig. 2.2**).

```
SEDYRDTVVKRKPASLMAPLKRKEEFSLFKVSDDEYKVTISPQLLLATQRF
             1                    2
LSREVDVFSPLRISEKVLLHLLKHPSVNQEVRFDESNRLATHHYLYQRSQP
                                    3
VDYFILILQGRVEVEIGKEGLKFENGAFTYYGVSALTVPSSVHQSPVSSLQ
                   4                          5
PIRHDLQPDPGDGTHSSAYCPDYTVRALSDLQLIKVTRLQYLNALLATRAQ
             67
NLPQSPENTDLQVIPGSQTRLLGEKTTTAAGSSHSRPGVPVEGSPGRNPGV
```

Figure 2.2 Methionine substitutions tested for phasing of the CNNM3 CNBH domain
The amino acid sequence of human CNNM3 is shown for residues 453 to 707. The naturally occurring methionine is shown in red. Sites of methionine substitutions are shown in blue and numbered 1 to 7. The best diffracting crystals were obtained with methionines at sites 1, 3, 4, 5, 6, and 7.

The structure of the selenomethionine-labeled CNNM CNBH mutant was solved using the single-wavelength anomalous dispersion (SAD) method to 1.9 Å (**Table 2.1** and **Fig. 2.3A**).

Four of the seven selenomethionines were observed in the electron density and allowed phasing of the diffraction data. The crystal contained two CNBD domains in the asymmetric unit, which could be superposed with an all-heavy atom root mean square deviation (RMSD) of 0.4 Å. Notably, close to 50% of the crystallized protein was not observed in the electron density maps. Specifically, the N terminus (residues 453–488), a long internal loop (residues 592–623), and the C terminus (residues 655–707) were disordered in both molecules (**Fig. 2.1B**).

We subsequently used this structure to design a construct of the CNBH domain of human CNNM2 as longer fragments had not crystallized. Residues 724–767, corresponding to the missing loop in the CNNM3 structure, were deleted. This loop shows little conservation between isoforms and is not predicted to form a regular secondary structure. Crystals of CNNM2 (residues 585–822, Δ724–767) were obtained, and the structure was solved by molecular replacement (**Table 2.1**). The CNNM2 crystals also contained two molecules in the asymmetric unit. The CNBH domains from CNNM2 and CNNM3 were very similar, with an RMSD value of 0.6 Å for 121 Cα atoms (**Fig. 2.3B**).

Table 2.1 Statistics of data collection and refinement

Construct	CNNM3 (453-707)	CNNM2 (585-822) Δ724–767
Data collection		
X-ray source	CHESS A1	CLS 08ID-1
Wavelength (Å)	0.9779	1.0332
Space group	$P4_22_12$	$P3_221$
Cell dimensions		
a, *b*, *c* (Å)	101.28, 101.28, 77.12	110.58, 110.58, 84.60
α, β, γ (°)	90.0, 90.0, 90.0	90.0, 90.0, 120.0
Resolution (Å)	50–1.90 (1.93–1.90)[1]	50–2.60 (2.69–2.60)
Redundancy	28.7 (27.5)	8.7 (5.4)
Completeness (%)	99.9 (100)	96.5 (70.9)
R_{meas} (%)	9 (286)	10 (146)
R_{pim} (%)	2 (53)	4 (48)
$I/\sigma I$	44.2 (1.8)	19.8 (0.8)
$CC_{1/2}$	0.662	0.609
Refinement		
Resolution (Å)	32.5–1.90	47.9–2.60
No. of reflections	32014	14399
R_{work}/R_{free}	0.219/0.239	0.219/0.251
No. of atoms		
Protein	2073	2332
Water	70	23
B-factors		
Protein	61.6	53.9
Water	54.2	26.8
RMSDs		
Bond lengths (Å)	0.004	0.002
Bond angles (°)	0.70	0.48
Ramachandran statistics (%)		
Most favored regions	97.2	96.7
Additional allowed regions	2.8	3.3
Disallowed regions	0.0	0.0
PDB code	6DFD	6DJ3

[1]Values for the highest-resolution shell are shown in parentheses.

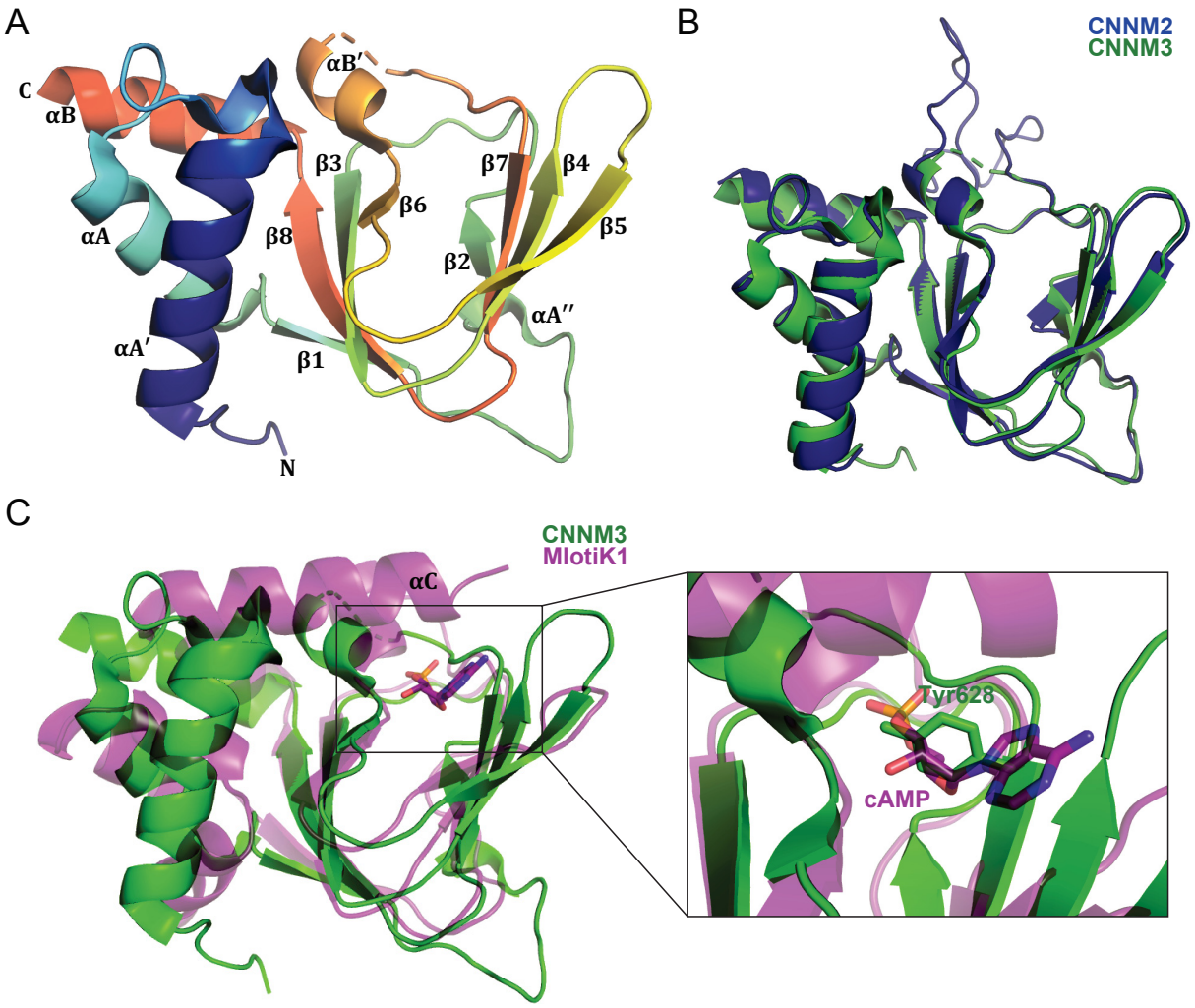

Figure 2.3 Crystal structures of CNBH domain of CNNM proteins

(A) *Cartoon representation* of CNNM3 CNBH domain, *colored blue* (N terminus) to *red* (C terminus). A disordered loop of 31 amino acids is indicated by a *dashed line*. The CNNM3 CNBH domain structure shows the typical fold of a cyclic nucleotide–binding domain: a wide antiparallel β-roll capped by an α-helical bundle. (B) Overlay of *cartoon representations* of CNBH domains of CNNM2 (*blue*) and CNNM3 (*green*). (C) Structural overlay of the CNBH domain of CNNM3 (*green*) with the cyclic nucleotide–binding domain of the bacterial K^+ channel from *Mesorhizobium loti* (*magenta*; PDB code 1VP6). The *M. loti* K^+ channel has an additional C-terminal helix (α*C*) that contacts the bound cAMP ligand. In CNNM3, a tyrosine side chain blocks the nucleotide-binding site.

2.3.2 Crystal structures of CNBH domain of CNNM3 and CNNM2

As expected, the CNBH domain structures are similar to structures of cyclic nucleotide–binding domains [100]. The domain contains an eight-stranded antiparallel β-roll that is capped by an α-helical bundle on the side (**Fig. 2.3A**). For consistency with the literature on cyclic nucleotide–binding domains, we labeled the two helices preceding the β-roll as αA′ and αA, the helix between β6 and β7 as αB′, and the helix following the β-roll as αB. The CNNM CNBH domains contain an additional single-turn α-helix (αA″) located between the β1 and β2 strands (**Fig. 2.1B**).

A major difference between the cyclic nucleotide–binding and CNBH domains is the large loop that was disordered in CNNM3 and partially deleted in CNNM2. In cyclic nucleotide–binding domains, the loop is 5 residues long and connects the αB′ helix and β7 strand (**Fig. 2.3A**). In CNNMs, the loop varies between 30 and 70 residues in length (**Fig. 2.1B**) and likely requires contacts with other domains in the full-length protein to fold properly. In one of the two CNNM2 molecules, weak electron density for the loop could be modeled due to crystal contacts that reduced the loop's mobility. The very high B-factors and the absence of a regular secondary structure suggest that its fold is not physiologically relevant (**Fig. 2.3B**).

A structural similarity search using the CNNM3 CNBH domain and the DALI server [101] identified the most structurally similar protein as the regulatory subunit of cAMP-dependent protein kinase (PDB code 2QVS) with an RMSD of 1.9 Å for 120 Cα atoms (Z-score of 15.1). Other top hits were a regulatory subunit of cGMP-dependent protein kinase (PDB code 5DYL, Z-score 14.0), cyclic nucleotide–binding protein (PDB code 5DLI, Z-score 14.0), and the cyclic nucleotide–binding domain of MlotiK1 potassium ion channel protein (PDB code 3CO2, Z-score 13.5). We used the MlotiK1 cyclic nucleotide–binding domain for detailed structural comparisons with the CNBH domains because it is from an ion channel, and structures are available for both ligand-free and nucleotide-bound forms [102].

Overall structural similarity to the cyclic nucleotide–binding domain of MlotiK1 is very high, particularly in the β-roll region, which is the site of nucleotide binding (**Fig. 2.3C**). The differences largely include slightly different orientations of helices and varied loop conformation. A number of loops are significantly longer in CNNMs. The main difference is the absence of helix αC in the CNBH domain of CNNM3. In cyclic nucleotide–binding domains, this C-terminal helix closes on the bound nucleotide, providing additional contacts and increased

affinity (**Fig. 2.3C**). This region is unstructured in CNNM3 despite being present in the crystallized protein. The amino acid sequence does not contain any predicted secondary structure elements and shows low sequence conservation among CNNM family members, strongly suggesting that the region does not form a helix in CNNMs.

A structural alignment of the CNNM3 CNBH structure with the nucleotide-bound structure of MlotiK1 (PDB code 1VP6) suggests that CNNM3 should not bind nucleotides. CNNM3 contains a tyrosine residue (Tyr-628) in the middle of the putative nucleotide-binding site that would sterically clash with a bound ligand (**Fig. 2.3C**). This residue is an alanine in MlotiK1 but a tyrosine or phenylalanine in all four CNNM members, suggesting that none of the isoforms bind cyclic nucleotides.

2.3.3 CNBH domains of CNNMs do not bind cyclic nucleotides

To test this hypothesis, we used thermal shift assays (TSAs), also known as differential scanning fluorimetry, with purified CNBH domains of CNNM1, CNNM2, CNNM3, and CNNM4 **(Fig. 2.4A** and **Table 2.2**). Protein stability is typically increased upon ligand binding, resulting in a higher melting (denaturation) temperature [103], as illustrated by a positive control that binds cAMP (**Fig. 2.5**) [104]. None of the melting temperatures of CNBH domains changed significantly upon the addition of cAMP or cGMP. Similar results were obtained either in the presence or absence of Mg^{2+} ions.

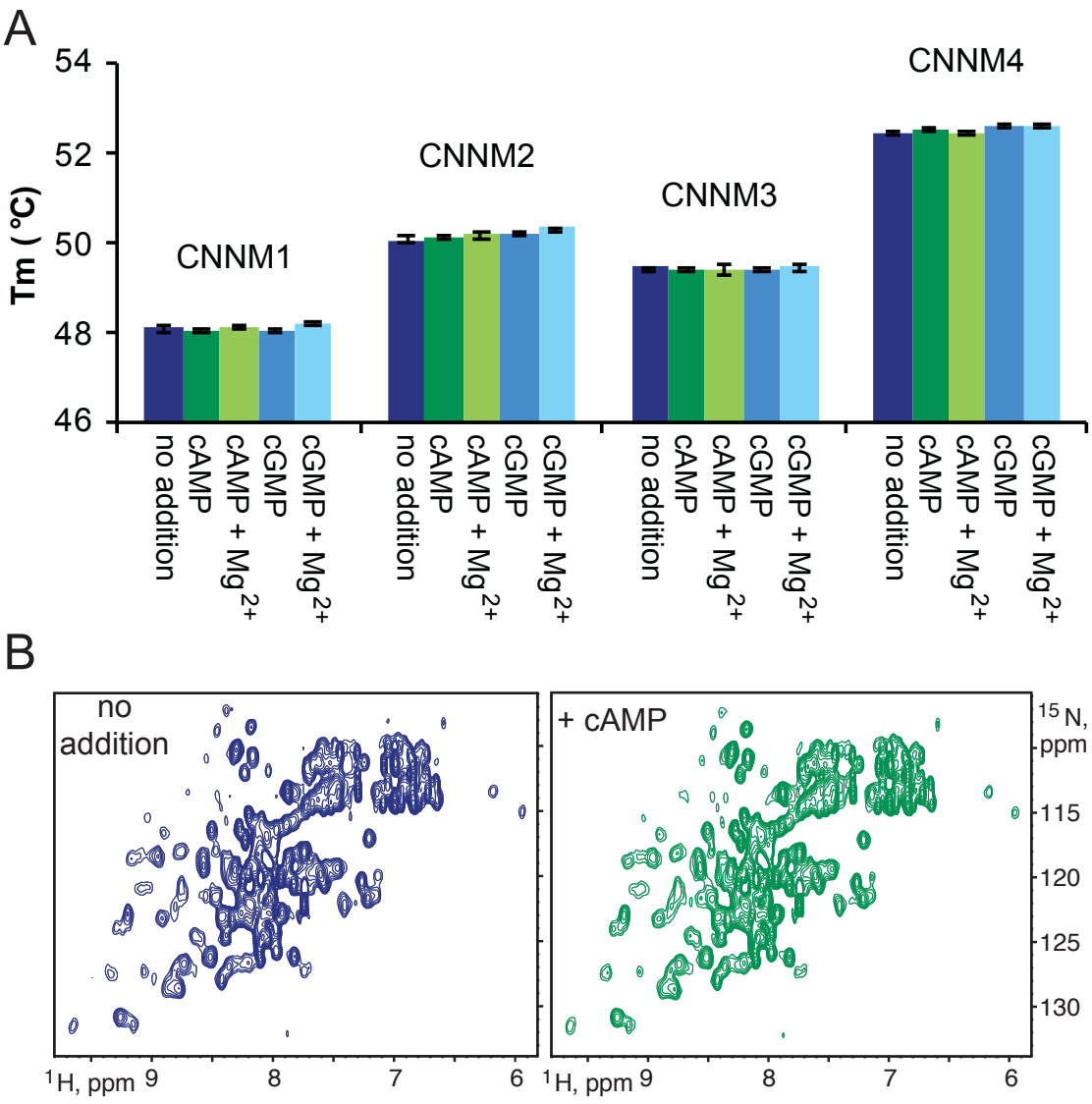

Figure 2.4 CNBH domains of CNNM proteins do not bind cyclic nucleotides

(A) Thermal shift assays of the denaturation of the CNBH domains of CNNM1–4 in the presence and absence of 1 mM cyclic nucleotides and 1 mM Mg^{2+}. Each experiment was performed in triplicates. *Error bars*, S.E. (B) Two-dimensional ^{1}H-^{15}N correlation spectra of CNNM4 CNBH domain without nucleotide or 3 mM cAMP. No significant shifts were observed, indicating no ligand binding.

Table 2.2 Thermal shift assay raw data

Protein	Condition	Tm (°C)				
		Replicate 1	Replicate 2	Replicate 3	Mean	Standard Error
CNNM1_CNBHD	no addition	48.20	48.02	48.11	48.11	0.05
CNNM1_CNBHD	cAMP	48.15	48.01	48.13	48.10	0.05
CNNM1_CNBHD	cAMP + $MgCl_2$	48.16	48.15	48.10	48.14	0.02
CNNM1_CNBHD	cGMP	48.17	48.04	48.01	48.08	0.05
CNNM1_CNBHD	cGMP + $MgCl_2$	48.16	48.18	48.29	48.21	0.04
CNNM2_CNBHD	no addition	50.23	49.94	50.10	50.09	0.09
CNNM2_CNBHD	cAMP	50.12	50.14	50.19	50.15	0.02
CNNM2_CNBHD	cAMP + $MgCl_2$	50.32	50.18	50.07	50.19	0.07
CNNM2_CNBHD	cGMP	50.34	50.21	50.13	50.23	0.06
CNNM2_CNBHD	cGMP + $MgCl_2$	50.39	50.30	50.32	50.34	0.03
CNNM3_CNBHD	no addition	49.49	49.48	49.43	49.47	0.02
CNNM3_CNBHD	cAMP	49.43	49.38	49.43	49.41	0.02
CNNM3_CNBHD	cAMP + $MgCl_2$	49.35	49.69	49.32	49.46	0.12
CNNM3_CNBHD	cGMP	49.54	49.32	49.43	49.43	0.07
CNNM3_CNBHD	cGMP + $MgCl_2$	49.38	49.35	49.67	49.47	0.10
CNNM4_CNBHD	no addition	52.46	52.53	52.36	52.45	0.05
CNNM4_CNBHD	cAMP	52.56	52.50	52.56	52.54	0.02
CNNM4_CNBHD	cAMP + $MgCl_2$	52.50	52.39	52.40	52.43	0.03
CNNM4_CNBHD	cGMP	52.65	52.64	52.53	52.61	0.04
CNNM4_CNBHD	cGMP + $MgCl_2$	52.58	52.64	52.63	52.62	0.02
lpg1496_KLAMP1	no addition	74.08	74.01	74.05	74.05	0.02
lpg1496_KLAMP1	cAMP	74.67	74.67	74.82	74.72	0.05

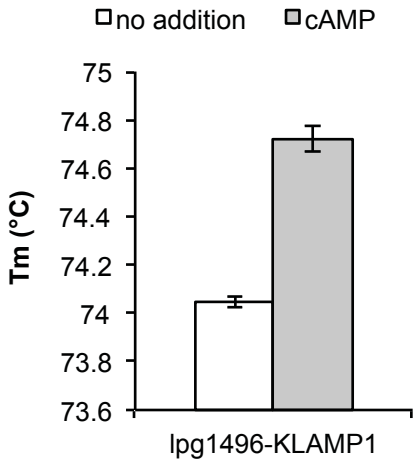

Figure 2.5 Thermal shift assays of positive control protein lpg1496-KLAMP1 in presence and absence of 1 mM cAMP

The melting temperature is increased by 0.7°C with addition of 1 mM cAMP. Each experiment was performed in triplicates. The error bars represent standard error.

As a more sensitive alternative, we used NMR to detect binding of cAMP to CNNM4 (**Fig. 2.4B**). NMR is very sensitive to molecular interactions, allowing for detection of even low-affinity binding in the millimolar range. The ^{1}H-^{15}N correlation spectrum of the ^{15}N-labeled CNNM4 CNBH domain showed good dispersion of signals, characteristic of a well-folded protein. Even at a cAMP concentration of 3 mM, no significant spectral changes were observed. Assuming a detection limit of 10% binding, this yields a lower bound on the affinity of 30 mM. Together, the TSA experiments and crystal structures demonstrate that CNBH domains of CNNM proteins do not bind cyclic nucleotides.

2.3.4 CNBH domains form dimers in solution

During purification, the CNNM3 CNBH domain was observed to elute as a dimer on size exclusion chromatography (**Fig. 2.6A**). To improve the resolution of monomers and dimers, which were poorly separated by size exclusion chromatography, we turned to sedimentation velocity analytical ultracentrifugation (AUC) (**Fig. 2.6B–E**, **Fig. 2.7**, and **Table 2.3**). AUC analysis at different protein concentrations (15–60 μM) revealed a single, dimeric species for the

CNNM3 CNBH domain. On the other hand, the CNNM1, CNNM2, and CNNM4 CNBH domains displayed a mixture of monomer and dimer species in a ratio that varied with protein concentration. At the same concentration, the ratio of dimer to monomer was higher for CNNM2 than that of CNNM1 and CNNM4, with CNNM4 having the least propensity toward dimerization.

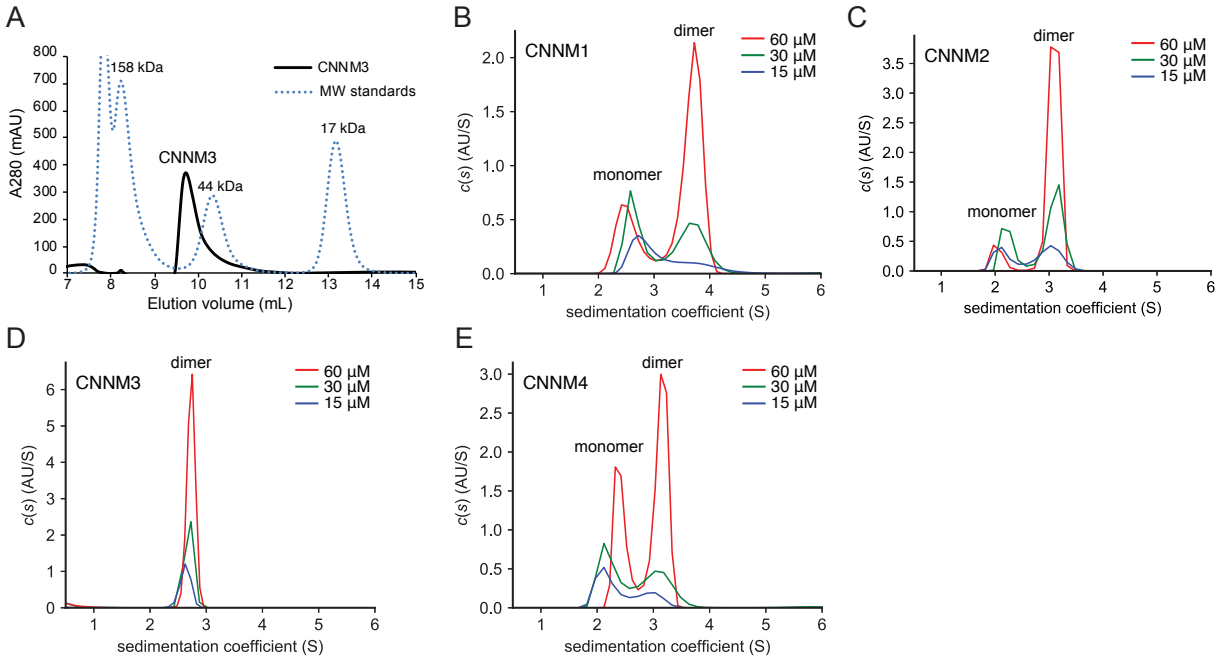

Figure 2.6 CNBH domains of CNNM proteins dimerize in solution

(A) Gel-filtration chromatography of the CNBH domain of CNNM3. The protein elutes as dimer of 47.8 kDa relative to gel-filtration standards (γ-globulin, 158 kDa; ovalbumin, 44 kDa; myoglobin, 17 kDa). (B–E) Sedimentation velocity analytical ultracentrifugation experiments of CNBH domains at three protein concentrations (15, 30, and 60 µM). The CNNM3 CNBH domain sediments as a dimer at all concentrations, whereas the domains from CNNM1, CNNM2, and CNNM4 sediment as mixtures of monomer and dimer forms (see **Table 2.3**).

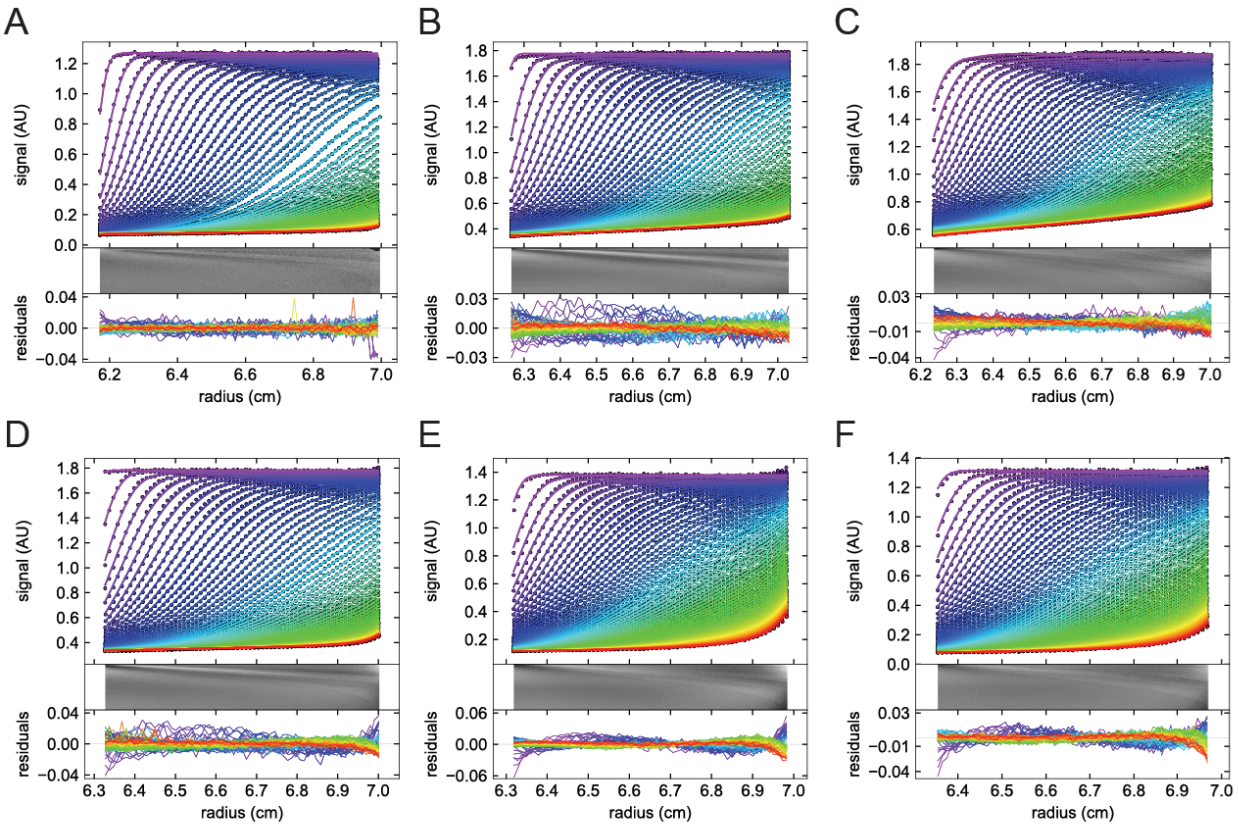

Figure 2.7 Representative sedimentation velocity AUC profile of 60 µM purified CNBH domains

(A) CNNM1 (B) CNNM2 (C) CNNM3 (D) CNNM4 (E) CNNM3 L575K (F) CNNM3 F577K The absorbance of the sample at 280 nm and residuals are plotted against the radial position in the cell. One in every 15 scans is plotted.

Table 2.3 SV-AUC sedimentation coefficients and estimated molecular weights

		Sedimentation coefficient (S)		Estimated MW (kDa)		RMSD	Theoretical MW (kDa)	
CNBH domain	[Protein] (μM)	Peak 1	Peak 2	Peak 1	Peak 2		Monomer	Dimer
CNNM1	60	2.52	3.68	28.1	52.9	0.0051	27.0	54.0
	30	2.62	3.68	30.2	46.7	0.0049		
	15	2.75	3.70	33.3	43.1	0.0043		
CNNM2	60	2.65	3.10	22.3	40.7	0.0053	22.7	45.4
	30	2.19	3.11	24.4	40.9	0.0047		
	15	2.11	3.04	25.8	41.1	0.0028		
CNNM3	60	2.76	-	44.2	-	0.0050	23.9	47.8
	30	2.70	-	37.1	-	0.0031		
	15	2.67	-	35.8	-	0.0025		
CNNM4	60	2.38	3.15	25.5	37.3	0.0053	25.0	50.0
	30	2.25	3.11	25.5	40.2	0.0043		
	15	2.24	3.06	25.3	35.6	0.0031		
CNNM3 L575K	60	2.08	-	20.7	-	0.0054	23.9	47.8
	30	2.04	-	21.5	-	0.0045		
	15	1.99	-	20.5	-	0.0031		
CNNM3 F577K	60	1.95	-	21.3	-	0.0053	23.9	47.8
	30	1.91	-	21.1	-	0.0035		
	15	1.90	-	20.7	-	0.0025		

2.3.5 Mutagenesis identifies the dimerization interface

Analysis of crystal contacts revealed two protein–protein interfaces that could be responsible for CNBH dimerization: one mediated by ionic interactions between the N-terminal helices and one involving hydrophobic contacts between the β-roll elements (**Fig. 2.8A**). To identify the interface responsible for dimerization, we generated four mutants in the CNNM3 CNBH domain and analyzed them by gel-filtration chromatography and AUC. Mutating hydrophobic residue Leu-575 or Phe-577 disrupted dimerization, whereas the loss of either charged residue in the N-terminal helix had no effect (**Fig. 2.8B**). Analogous CNNM4 mutants also disrupted dimerization. The WT domain eluted as a broad peak consisting mostly of dimers, whereas the M629K and F631K mutants eluted as monomers (**Fig. 2.8B**). AUC analysis confirmed that the CNNM3 CNBH mutants L575K and F577K were both monomeric (**Fig. 2.8C**).

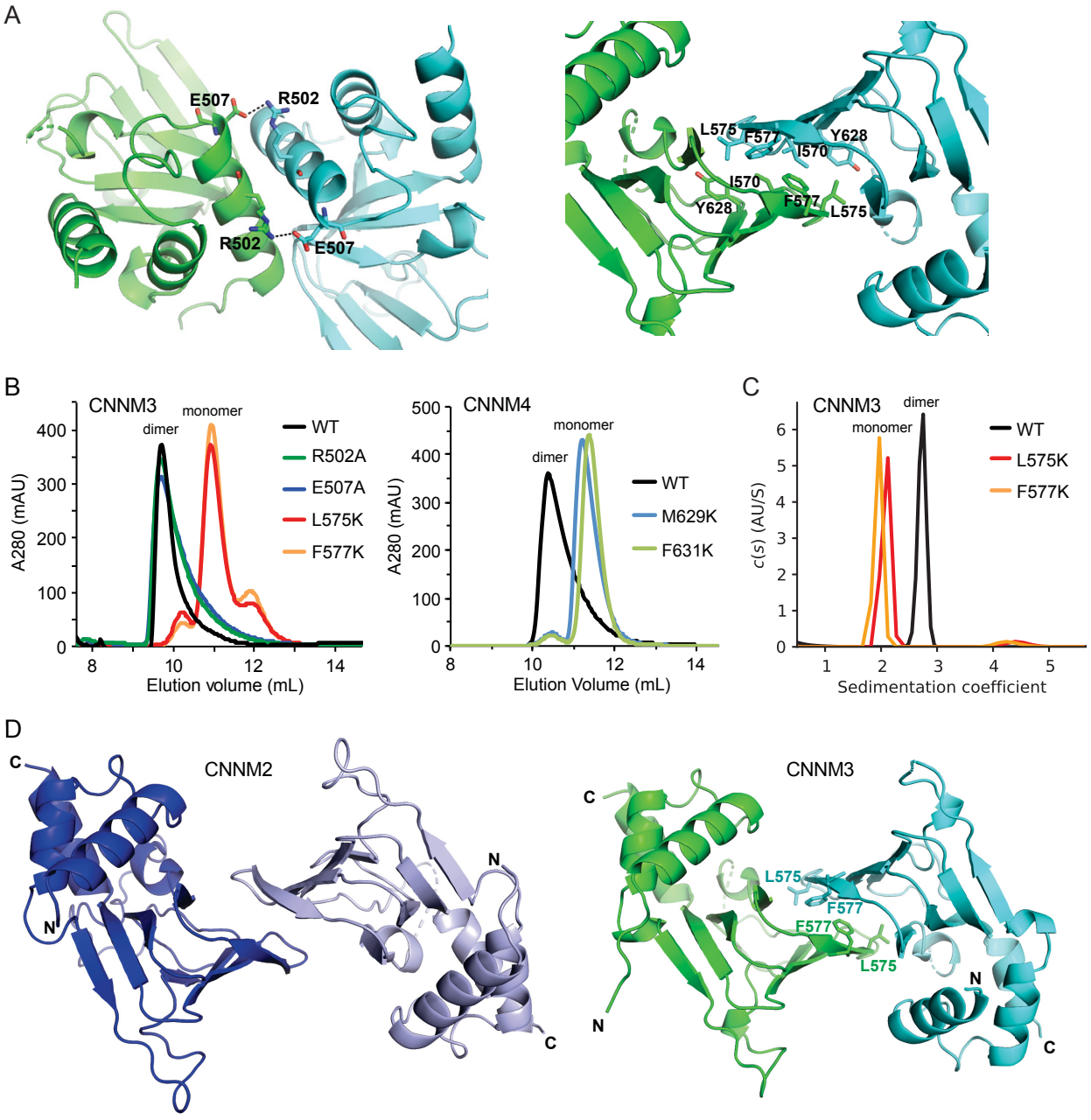

Figure 2.8 Identification of the dimer interface

(A) Two alternative dimerization interfaces observed in the CNNM3 crystals. *Left*, mediated by ionic interactions. *Right*, mediated by hydrophobic contacts. Each chain is colored differently. (B) Gel-filtration chromatograms of WT and mutant CNBH domains. Four mutants were generated: R502A and E507A to disrupt the first interface and L575K and F577K to disrupt the second. The CNNM3 L575K and F577K mutants and analogous CNNM4 M629K and F631K mutants eluted as monomers. (C) Analytical ultracentrifugation of CNNM3 CNBH domain,

confirming that the L575K and F577K mutants behave as monomers at 60 μM. (D) Comparison of the CNNM2 (*left*) and CNNM3 (*right*) CNBH dimers. The dimer interface is formed by a β-roll structure with a buried surface area of 1125 and 1547 $Å^2$ for CNNM2 and CNNM3, respectively. The locations of the CNNM3 residues mutated to disrupt dimerization are indicated. Each chain is colored differently.

The β-roll dimerization surface is conserved in both CNNM2 and CNNM3 structures (**Fig. 2.8D**). The hydrophobic residues Ile-570, Leu-575, Phe-577, and Tyr-628 in CNNM3 are highly conserved across all four CNNM isoforms (**Fig. 2.1B**), which suggests that all of the CNBH domains can dimerize in the same fashion. The weaker dimerization of CNNM2 and CNNM4 could be related to the substitutions of alanine and methionine at positions 570 and 575 of CNNM3 or smaller buried surface areas (**Fig. 2.8D**). Finally, we note that the dimerization further explains the inability of CNBH domains to bind nucleotides; the intermolecular contacts at the dimer interface overlap with the putative ligand-binding site.

2.3.6 CNNM4 CNBH domain is essential for function

To assess the role of the CNBH domain in CNNM function, we measured CNNM-dependent Mg^{2+} efflux in a cellular assay with WT and mutant CNNM4 [20]. Deletion of the CNBH domain completely blocked CNNM4-associated Mg^{2+} efflux but had no effect on protein expression or localization (**Fig. 2.9**). To test the role of CNBH dimerization, we assayed the two CNNM4 point mutants that prevent CNBH dimerization. The mutations, M629K and F631K, had divergent effects on the cellular Mg^{2+} efflux. F631K showed significant impairment, but M629K showed close-to-WT efflux, indicating that CNBH dimerization is not required for Mg^{2+} efflux. This is consistent with the observation that the CNBH domain from the most active CNNM isoform has the least tendency to form dimers.

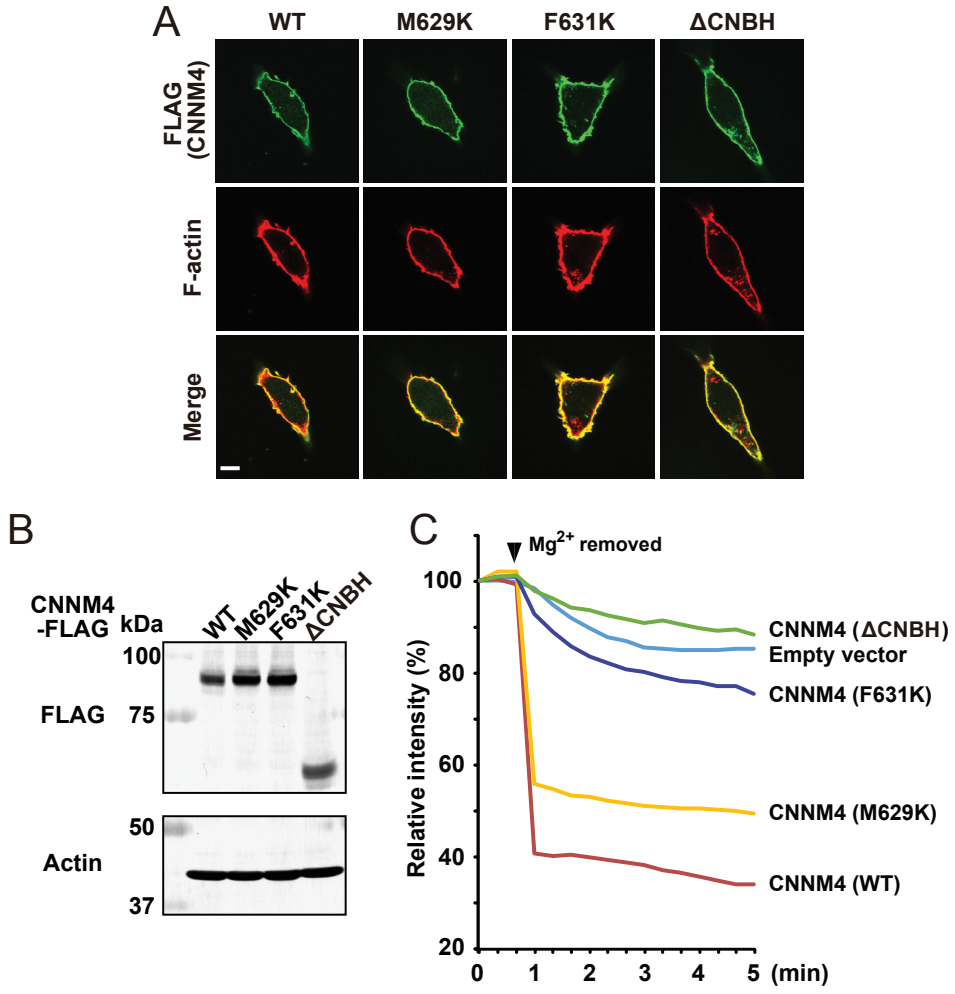

Figure 2.9 CNBH domain is not required for CNNM4 expression or localization but is required for Mg^{2+} efflux

(A) Immunofluorescence images of HEK293 cells with anti-FLAG (*green*) and rhodamine-phalloidin (*red*) showing that CNNM4 WT and mutant proteins are properly colocalized with F-actin adjacent to the cell membrane. The mutations, M629K and F631K, prevent CNBH dimerization. *Bar*, 10 μm. (B) Western blotting showing equal expression of CNNM proteins in lysates of HEK293 cells transfected with the indicated constructs. (C) Mg^{2+} efflux assays showing that deletion of the CNBH domain (ΔCNBH) blocks activity. HEK293 cells transfected with the indicated constructs were loaded with Magnesium Green and then subjected to Mg^{2+} depletion at the indicated time point (*arrowhead*). The mean relative fluorescence intensities of 10 cells are shown in the graph.

2.4 Discussion

A wide variety of presumptive Mg^{2+} transporters exist in bacterial and eukaryotic cells, but the precise molecular function of many is under debate [105]. Atomic structures are known for only two bacterial transporters: CorA and MgtE [106]. CNNM proteins show the greatest sequence similarity to DUF21 domain proteins, a large family of putative Mg^{2+} transporters found in bacteria, plants, and animals. Bacterial DUF21 domain proteins have architectures similar to CNNM proteins, consisting of an integral membrane domain of three transmembrane helices, followed by a CBS-pair domain and a small C-terminal globular protein domain similar in size to CNNM CNBH domains. Crystal structures of the C-terminal domains of several bacterial DUF21 proteins show that they also form dimers (PDB entries 3DED, 2OAI, 2R8D).

The CNBH domain of CNNM proteins are structurally similar to many cyclic nucleotide–binding domains of cyclic nucleotide-gated channels [107-109], but our results demonstrate the inability of these domains to bind cAMP or cGMP. Although co-purification with bacterial cAMP [100] or binding to noncanonical cyclic nucleotides (not tested) is still possible [110], the three-dimensional structures strongly suggest otherwise. The first reason is the presence of a large aromatic residue (Tyr-628 in CNNM3) in the middle of the typical nucleotide-binding site (**Fig. 2.3C**). This is similar to the related domain in the KCNH (ether-à-go-go K^+) channel, which does not bind nucleotide due to blockage of the β-roll binding pocket by an adjacent three-residue β-strand motif [111]. Second, CNBH domains lack the C-terminal αC helix typically involved in cyclic nucleotide binding (**Fig. 2.3C**). Normally, upon nucleotide binding, the αB and αC helices rotate toward the β-roll, allowing the αC helix to interact with the base moiety and cap the binding pocket [107]. In the case of CNNM, the absence of the αC helix prevents the stable binding of the nucleotide. Finally, the would-be nucleotide-binding surface is heavily involved in the intermolecular interaction of the dimer interface (**Fig. 2.8**). Major conformational changes would be required for a nucleotide to bind.

Instead, the function of the CNBH domain appears to be dimerization. Cyclic nucleotide–binding domains mediate dimerization in many proteins. The best-understood example is catabolite gene activator protein, which contains a cAMP-binding domain that is responsible for protein dimerization [112]. The cyclic nucleotide–binding domains of the superfamily of voltage-gated K^+ channel (which includes KCNH channels) form dimers [113]. Like CNNM proteins, KCNH CNBH domains do not bind nucleotides but rather use the β-roll structure to

interact with another protein domain, regulating the channel in a cyclic nucleotide–independent manner [114].

CNNM CNBH domains may play a similar role in regulating CNNM activity. CNNM isoforms show large differences in Mg^{2+} efflux activity, where CNNM4 possesses the highest activity, CNNM2 shows intermediate activity, CNNM1 shows weak activity, and CNNM3 is inactive [41]. The differences in efflux activity inversely correlate with the propensity of CNBH domains to dimerize (**Fig. 2.6**). Whereas the CNBH domain is essential for Mg^{2+} efflux activity, dimerization is not required as the M629K mutation that disrupts the dimer interface has only a modest effect on Mg^{2+} efflux (**Fig. 2.9C**).

Although the exact molecular function of CNNM proteins remains still unclear, the structural and functional characterization of their C-terminal CNBH domains is a valuable piece of the puzzle. However, fully understanding the connections between CNNM and Mg^{2+} metabolism and cancer will require additional functional studies and ultimately structural elucidation of the full-length protein.

2.5 Experimental Procedures

2.5.1 Cloning of CNNM C-terminal domains

Human CNNM1 CNBH domain (residues 569–798), CNNM2 CNBH domain (residues 585–824), CNNM2 $CNBH_{cryst}$ domain (residues 585–822 with a deletion of residues 724–767), CNNM3 CNBH domain (residues 453–707), and CNNM4 CNBH domain (residues 513–728) were codon-optimized for *Escherichia coli* (Bio Basic Inc., Markham, Canada) and subcloned into BamHI and NotI sites of pGEX-6P-1 vector (Amersham Biosciences) with an N-terminal GST tag. Mutagenesis was performed using the QuikChange site-directed/multi-mutagenesis kit (Agilent).

2.5.2 Expression and purification of recombinant proteins

All constructs were verified by DNA sequencing and transformed into *E. coli* strain BL21 (DE3). Cultures were grown at 37 °C in Luria broth to an optical density of 0.8 and induced with 1 mM isopropyl 1-thio-β-D-galactopyranoside for 4 h at 30 °C. Cell pellet was obtained by centrifuging at 5000 × g for 20 min. The pellet was resuspended in buffer A (50 mM HEPES, 500 mM NaCl, 5% glycerol, 5 mM β-mercaptoethanol, pH 7.5) and lysed by sonication. Cellular debris was removed by centrifugation at 44,000 × g for 45 min at 4 °C. The supernatant was loaded onto Pierce GSH-agarose resin, washed with buffer A, and eluted with buffer A containing 20 mM GSH. The GST tag was removed by overnight incubation with PreScission Protease, leaving an N-terminal Gly-Pro-Leu-Gly-Ser extension. The protein was further purified by a Superdex-75 size-exclusion column (GE Healthcare) in HPLC buffer (20 mM HEPES, 100 mM NaCl, 3 mM TCEP, pH 7.5). The final purified protein was concentrated to around 10 mg/mL (measured by NanoDrop), and the purity was verified by SDS-PAGE. For selenomethionine labeling, the plasmid was transformed into a methionine auxotroph strain DL41 (DE3), and the protein was produced using LeMaster medium. The expression and purification protocols were the same as for the native protein. For ^{15}N labeling, the cells were grown in M9 minimal medium supplemented with ^{15}N-ammonium chloride as the sole source of nitrogen. The expression and purification protocols were the same as for the native protein.

2.5.3 Crystallization

Crystals of selenomethionine-labeled CNNM3 CNBH domain with amino acid substitutions I516M, R535M, T591M, A623M, L651M, V669M, and I670M were obtained by equilibrating 0.6 µL of protein (10 mg/mL) with 0.6 µL of reservoir solution (0.8 M succinic acid, pH 7.0) in a hanging-drop vapor diffusion system incubated at 22 °C. Crystals of CNNM2 $CNBH_{cryst}$ domain were obtained by equilibrating 2 µL of protein (10 mg/ml) with 2 µL of reservoir solution (0.1 M BisTris, pH 6.0, 0.5 M sodium citrate, pH 7.0) in a hanging-drop vapor diffusion system incubated at 22 °C.

2.5.4 Data collection, structure determination, and refinement

The crystals were cryoprotected by soaking in mother liquor supplemented with 30% ethylene glycol, picked up in a nylon loop, and flash-cooled in a N_2 cold stream. The CNNM3 CNBH domain SAD data set from a single crystal was collected using a single-wavelength (0.9779 Å) regime at beamline A1 of the Cornell High-Energy Synchrotron Source (CHESS) using an ADSC Quantum-210 CCD detector (Area Detector Systems Corp.). Data processing and scaling were performed with HKL-2000 [115]. The starting phases were obtained by selenium-SAD using PHENIX [116]. Initial model was built using AutoBuild [117] and extended manually with the help of the program Coot [118] and was improved by several cycles of refinement using the program REFMAC5 [119] followed by TLS refinement [120]. The CNNM2 CNBH domain diffraction data set was collected on beamline 08ID-1 with a Rayonix MX300 CCD detector at the Canadian Macromolecular Crystallography Facility (CMCF) of the Canadian Light Source (CLS). Data processing and scaling were performed with HKL-2000 [115]. The CNNM2 CNBH domain structure was solved by molecular replacement using Phaser [121] with the CNNM3 CNBH domain structure as a search model. Refinement was carried out by phenix.refine [122]. Crystallographic data collection and structure refinement statistics are shown in **Table 2.1**. The final models have good stereochemistry with no outliers in the Ramachandran plot computed using PROCHECK [123]. Structural images were prepared with PyMOL, Version 2.0 (Schroedinger LLC, New York).

2.5.5 Thermal shift assays

Each reaction contained 20 µL of solution with 25 µM CNBH domain, 1× Protein Thermal Shift™ dye (Life Technologies), HPLC buffer with and without nucleotides and $MgCl_2$. Samples were heated from 25 to 99 °C at a rate of 1 °C/min, and fluorescence signals were monitored by the StepOne Plus quantitative real-time PCR system (Life Technologies, Inc.). Data were analyzed using Thermal Shift software (Life Technologies). The maximum change of fluorescence with respect to temperature was used to determine the melting temperature (T_m). Each sample was performed in triplicates, and S.E. was calculated for each T_m measured. Positive control protein (lpg1496-KLAMP1) was expressed and purified as described [104].

2.5.6 NMR spectroscopy

^{1}H-^{15}N heteronuclear single-quantum correlation spectroscopy was performed on a Bruker 600-MHz spectrometer using 0.15 mM ^{15}N-labeled CNNM4 CNBH domain in 90% HPLC buffer and 10% D_2O. Testing for cNMP binding was carried by acquiring TROSY spectra before and after the addition of 3 mM cAMP. NMR data were acquired at 40 °C. NMR spectra were processed using NMRPipe [124] and analyzed with SPARKY [125].

2.5.7 Analytical ultracentrifugation

Sedimentation velocity AUC experiments were performed at 20 °C using a Beckman Coulter XL-I analytical ultracentrifuge using an An-60Ti rotor at 98,000 × g (35,000 rpm) for 18 h with scans performed every 60 s. A double-sector cell, equipped with a 12-mm Epon centerpiece and sapphire windows, was loaded with 380 and 400 µL of sample and HPLC buffer, respectively. Samples at concentrations ranging from 15 to 60 µM were monitored with UV at 280 nm. The data were analyzed with Sedfit version 1501b [126] using a continuous *c(s)* distribution. Numerical values for the solvent density, viscosity, and the partial specific volume were determined using Sednterp [127]. Buffer density and viscosity were calculated to be 1.0039 g/cm^3 and 0.01026 millipascals·s, respectively (20 mM HEPES, 100 mM NaCl, 3 mM TCEP, pH 7.5). Partial specific volumes for CNBH domains of CNNM1–4 were calculated to be 0.7172, 0.7419, 0.7416, and 0.7350 cm^3/g, respectively. Frictional ratio (f/f_0) values of CNNM2 and CNNM3 CNBH domains were calculated using US-SOMO [128] to be 1.29 and 1.21, and

the value for CNNM1 and CNNM4 was estimated to be 1.29 based on similarity to CNNM2. Residual and *c(s)* distribution graphs were plotted using GUSSI [129].

2.5.8 Size-exclusion chromatography

Analytical gel-filtration experiments were carried out on an Akta Purifier HPLC system (GE Healthcare) using a 100-µL sample volume on a Superdex 75 Increase 10/300 GL column (GE Healthcare) with a flow rate of 0.8 mL/min at 4 °C using HPLC buffer. Gel-filtration standards were purchased from Bio-Rad (catalogue no. 151-1901).

2.5.9 Constructs used in mammalian culture cells

Human CNNM4 inserted into mammalian expression vector (pCMV tag-4A) was generated in the previous study [20]. M629K, F631K, and ΔCNBH (Δ512–775) mutants were generated using the QuikChange site-directed mutagenesis kit (Agilent).

2.5.10 Mg^{2+}-efflux assays

Mg^{2+}-imaging analyses with Magnesium Green were performed as described in the previous study [20, 96]. Transfected HEK293 cells were incubated under growth media supplemented with 40 mM Mg^{2+} until use, to avoid potential decrease of intracellular Mg^{2+} levels by the expressed proteins. Then the cells were incubated with Mg^{2+}-loading buffer (78.1 mM NaCl, 5.4 mM KCl, 1.8 mM $CaCl_2$, 40 mM $MgCl_2$, 5.5 mM glucose, 5.5 mM HEPES-KOH, pH 7.4), including 2 µM Magnesium Green-AM (Invitrogen), for 30 min at 37 °C. The cells were rinsed once with loading buffer and viewed using a microscope (IX81 (Olympus) equipped with an ORCA-Flash 4.0 CMOS camera (Hamamatsu) and a USH-1030L mercury lamp (Olympus)). Fluorescence was measured every 20 s (excitation at 470–490 nm and emission at 505–545 nm) under the control of the Metamorph software (Molecular Devices). Then the buffer was changed to remove Mg^{2+} buffer ($MgCl_2$ in the loading buffer was replaced with 60 mM NaCl). The data are presented as line plots of the mean fluorescence of 10 cells. After imaging analyses, cells were fixed with PBS containing 3.7% formaldehyde and subjected to immunofluorescence microscopy to confirm protein expression.

2.5.11 Immunofluorescence microscopy

Cells cultured on coverslips were stained and observed according to the previous study [20]. Cells were fixed with 3.7% formaldehyde in PBS for 20 min and permeabilized with 0.2% Triton X-100 in PBS for 5 min. After blocking with PBS containing 3% fetal bovine serum and 10% BSA (blocking buffer) for 1 h, cells were incubated for 1 h with rabbit anti-FLAG antibody (Sigma F7425) diluted in blocking buffer. Cells were washed three times with PBS and incubated for 30 min with Alexa 488–conjugated anti-rabbit IgG (Invitrogen A-11034) and rhodamine-phalloidin (for F-actin visualization, Wako 165-21641) diluted in blocking buffer. After three washes with PBS, coverslips were mounted on slides and observed with a confocal scanning laser microscope (FLUOVIEW FV1000, Olympus).

2.6 Acknowledgements

We thank Véronique Sauvé and Jean-François Trempe for assistance with crystallographic data collection, Nadeem Siddiqui for advice on AUC data processing, and Alexei Gorelik for advice on crystallographic data processing. Crystallographic data were acquired at the Canadian Light Source (CLS) and at the Macromolecular Diffraction (MacCHESS) facility at the Cornell High-Energy Synchrotron Source (CHESS). CHESS is supported by National Science Foundation award DMR-0225180 and National Institutes of Health/NCRR Grant RR-01646.

Chapter 3 – Mg^{2+}-ATP sensing in CNNM, a putative magnesium transporter

Chen, Y. S., Kozlov, G., Fakih, R., Yang, M., Zhang, Z., Kovrigin, E. L., and Gehring, K. (2020). *Structure* **28**, 324-335.

3.0 Connecting text

Even though the CNBH domain structure has been determined, some questions still remain unanswered. For example, why is the CNBH domain required for Mg^{2+} efflux function? The structures of both cytosolic domains (CBS-pair and CNBH domains) have been determined individually, but what is the interplay between them? In this chapter, I attempt to answer these two questions.

3.1 Summary

The family of cystathionine-β-synthase (CBS)-pair domain divalent metal cation transport mediators (CNNMs) is composed of four integral membrane proteins associated with Mg^{2+} transport. Structurally, CNNMs contain large cytosolic regions composed of a CBS-pair and a cyclic nucleotide-binding homology (CNBH) domain. How these regulate Mg^{2+} transport activity is unknown. Here, we determined the crystal structures of cytosolic fragments in two conformations: Mg^{2+}-ATP-analog bound and ligand free. The structures reveal open and closed conformations with functionally important contacts not observed in structures of the individual domains. We also identified a second Mg^{2+}-binding region in the CBS-pair domain and a different dimerization interface for the CNBH domain. Analytical ultracentrifugation and isothermal titration calorimetry experiments revealed a tight correlation between Mg^{2+}-ATP binding and protein dimerization. Mutations that blocked either function prevented cellular Mg^{2+} efflux activity. The results suggest Mg^{2+} efflux is regulated by conformational changes associated with Mg^{2+}-ATP binding to CNNM CBS-pair domains.

3.2 Introduction

Cystathionine-β-synthase (CBS)-pair domain divalent metal cation transport mediators (CNNMs), also called ancient conserved domain proteins (ACDPs), are an evolutionarily conserved family of four integral membrane proteins implicated in maintaining Mg^{2+} homeostasis [14, 130]. *CNNM* mutations are associated with a number of genetic diseases. Mutations in *CNNM2* are found in patients with familial dominant hypomagnesemia accompanied by low Mg^{2+} serum level and symptoms such as muscle weakness, tremor, and headaches [19]. Mutations in *CNNM4* are implicated in Jalili syndrome, characterized by recessive amelogenesis imperfecta and cone-rod dystrophy [44, 48]. The CNNM2 and CNNM4 proteins possess Mg^{2+} efflux activity and have been shown to facilitate renal/intestinal (re)absorption of Mg^{2+} as they localize to the basolateral membrane of renal/intestinal epithelial cells [19, 20].

More recently, CNNM-associated Mg^{2+} transport was shown to be regulated by the binding of phosphatases of regenerating liver (PRLs) [65, 66]. PRLs are potent oncogenes with strong association with metastatic cancers [99]. When PRLs bind CNNMs, the intracellular Mg^{2+} level is increased, thereby promoting tumor progression and cellular proliferation [65, 66]. Despite the association with Mg^{2+} transport, it is still debated whether CNNM proteins are themselves Mg^{2+} transporters or whether they regulate other proteins that transport Mg^{2+} [31, 32].

Structurally, CNNMs contain an N-terminal extracellular domain, a transmembrane domain (domain of unknown function 21 [DUF21]), and a large cytosolic region containing a CBS-pair domain and a cyclic nucleotide-binding homology (CNBH) domain (**Fig. 3.1A**) [24]. CBS-pair domains, also known as Bateman modules, consist of two repeated 60-residue CBS motifs that fold together to form a domain found in many proteins, such as AMP-activated protein kinase (AMPK), inosine-5′-monophosphate dehydrogenase (IMPDH), chloride channel (ClC), and bacterial Mg^{2+} transporter MgtE [92, 93]. The CBS-pair domain in CNNM dimerize in a head-to-head manner forming disc-like structures that enclose central nucleotide-binding sites for Mg^{2+}-ATP [91]. CBS-pair domain structures have also been elucidated with PRL phosphatases bound [96-98]. Binding is mediated by a loop from CBS-pair domain that extends into the phosphatase active site.

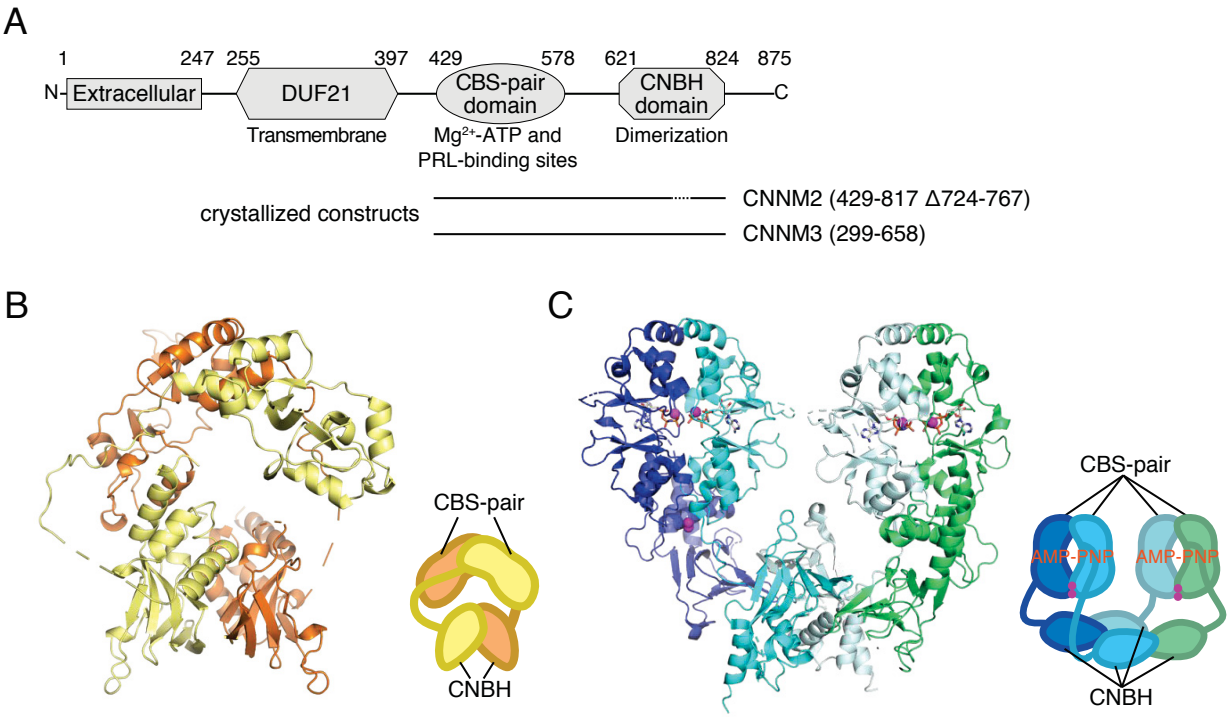

Figure 3.1 Crystal structures of cytosolic fragments of CNNM proteins in nucleotide-free or Mg^{2+}-AMP-PNP-bound states

(A) CNNM consists of four domains: the extracellular domain, DUF21, CBS-pair domain, and CNBH domain. Residues are numbered according to CNNM2. (B) CNNM3 cytosolic fragments form an open homodimer in the nucleotide-free state. Each chain is colored differently. (C) Four molecules of the CNNM2 cytosolic fragments associate in the crystal asymmetric unit. Each chain is colored differently. Each CBS-pair domain binds Mg^{2+}-AMP-PNP with additional Mg^{2+} ions (*magenta*) present at the dimer interface.

The structures of CNBH domains from CNNM2 and CNNM3 have also been determined [131]. The domains are structurally similar to cyclic nucleotide-binding domains but do not bind cyclic nucleotides; instead, they form dimers [131]. Disrupting dimerization of CNBH domain reduced Mg^{2+} efflux activity while deletion of the domain abrogated the efflux activity entirely, indicating that the domain is required for function [131]. However, it remains unclear how dimerization function of this domain affects functions, and the interplay between CBS-pair and CNBH domains remains to be elucidated.

Here, we determined the crystal structures of cytosolic fragments of two CNNM proteins containing both CBS-pairs and CNBH domains. The structures captured two states: unliganded and Mg^{2+}-ATP-analog bound. Structural comparisons reveal large conformational changes in both the CBS-pair and CNBH domains and a different dimerization interface for the C-terminal CNBH domain. Analytical ultracentrifugation (AUC) experiments showed dimerization of CNNM CBS-pair domains in solution depends on Mg^{2+}-ATP binding and is further enhanced by PRL binding. Isothermal titration calorimetry (ITC) experiments confirmed the correlation of Mg^{2+}-ATP binding and dimerization and showed disease-related mutations abrogate Mg^{2+}-ATP binding. The results suggest that CNNM protein activity is regulated by conformational changes in the CBS-pair domain associated with Mg^{2+}-ATP binding.

3.3 Results

3.3.1 Crystal structures of the cytosolic fragments reveal interplay between the cytosolic CBS-pair and CNBH domains

We determined the crystal structures of the cytosolic fragments of CNNM2 and CNNM3 with and without Mg^{2+} and a non-hydrolyzable ATP analog (AMP-PNP; adenosine 5'-(β,γ-imido)triphosphate) (**Table 3.1**). The two structures show significant differences, likely related to the presence of Mg^{2+}-AMP-PNP in the CNNM2 structure (**Fig. 3.1B & C**). The CNNM2 cytosolic fragments crystallized with four molecules in the asymmetric unit arranged as two sets of crossed dimers (**Fig. 3.1C**). The dimer interfaces are similar to those observed in studies of the isolated CBS-pair and CNBH domains [91, 96-98, 131]. In contrast, the ligand-free CNNM3 cytosolic fragment crystallized in an open conformation as a weakly associated dimer with previously unreported protein-protein contacts (**Fig. 3.1B**). To address the possibility that CNNM cytosolic fragments may form tetramers, we performed sedimentation velocity (SV)AUC experiments with CNNM2-4. We observed no evidence of tetramers (**Fig. 3.2**), indicating that the observed dimer of dimer in the asymmetric unit most likely arises from crystal packing.

Table 3.1 Statistics of data collection and refinement

Construct	CNNM2 (429-817) Δ724–767	CNNM3 (299-658)
Data collection		
X-ray source	CLS 08ID-1	CHESS A1
Wavelength (Å)	0.9796	0.6235
Space group	C2	$P3_221$
Cell dimensions		
a, *b*, *c* (Å)	290.58, 111.14, 103.52	128.06, 128.06, 111.32
α, β, γ (°)	90.0, 101.01, 90.0	90.0, 90.0, 120.0
Resolution (Å)	50–3.50 (3.56–3.50)[1]	50–3.36 (3.42–3.36)
Redundancy	3.4 (3.3)	12.1 (11.5)
Completeness (%)	99.9 (100.0)	100.0 (100.0)
$I/\sigma I$	19.6 (1.0)	14.6 (0.7)
$CC_{1/2}$	0.369	0.351
Refinement		
Resolution (Å)	48.8–3.50	49.8–3.36
No. of reflections	36990	12603
R_{work}/R_{free}	0.241/0.282	0.217/0.263
No. of atoms		
Protein	9279	4551
AMP-PNP[2]	124	N/A
Mg^{2+}	8	N/A
water	4	N/A
B-factors		
Protein	65.3	56.5
AMP-PNP	85.0	N/A
Mg^{2+}	54.1	N/A
water	10.6	N/A
RMSDs		
Bond lengths (Å)	0.002	0.003
Bond angles (°)	0.51	0.57
Ramachandran statistics (%)		
Most favored regions	95.0	95.0
Additional allowed regions	5.0	5.0
Disallowed regions	0.0	0.0
PDB code	6N7E	6MN6

[1]Highest resolution shell is shown in parentheses

[2]Adenosine 5'-(*β,γ*-imido)triphosphate

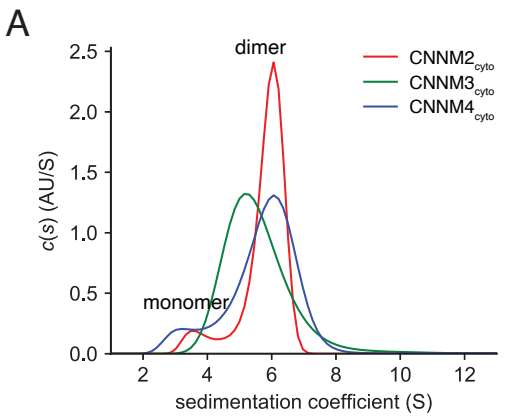

B

	Sedimentation coefficient (S)		Estimated MW (kDa)		RMSD	Theoretical MW (kDa)	
Cytosolic fragment	Peak 1	Peak 2	Peak 1	Peak 2		Monomer	Dimer
CNNM2	3.62	5.94	44.7	87.0	0.0051	40.7	81.4
CNNM3	-	5.35	-	84.0	0.0053	41.4	82.8
CNNM4	3.29	5.98	42.2	88.9	0.0049	40.2	80.4

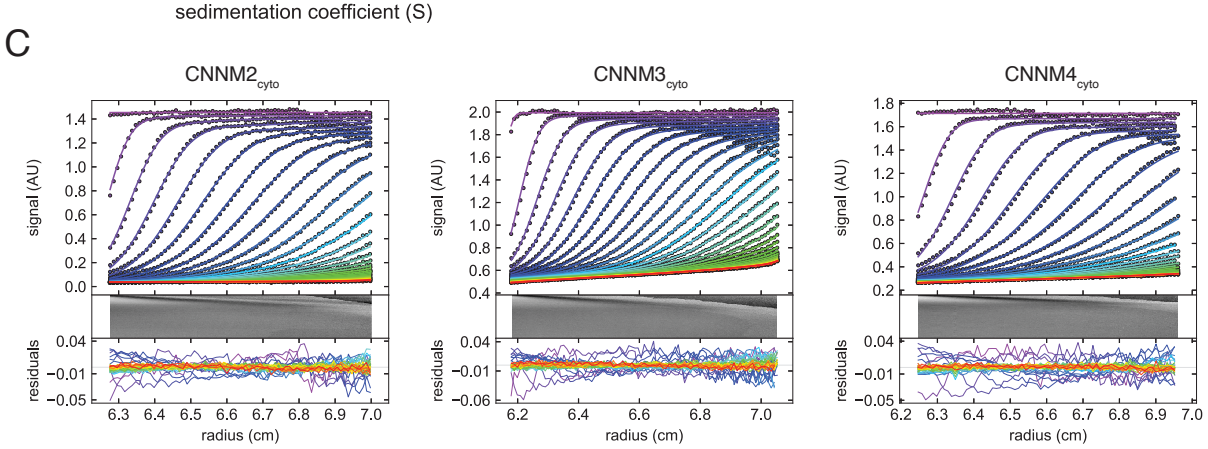

Figure 3.2 Oligomerization analysis of cytosolic fragments of CNNM2-4

(A) Sedimentation velocity analytical ultracentrifugation (SV-AUC) experiments of cytosolic fragments of CNNM2-4. All three cytosolic fragments sediment mostly as dimers. (B) Summary of experimental sedimentation coefficients and estimated molecular weights. (C) Representative SV-AUC profiles. The absorbance of the sample at 280 nm and residuals are plotted against the radial position of the cell. One in every 15 scans is plotted.

In both structures, the CBS-pair domains form dimers, but the angle between the protomers differs by a 90° rotation (**Fig. 3.3A**). Dimerization in CNNM3 CBS-pair domain is mediated by only the second CBS motif and the contact surface is half (980 Å^2) that of the CNNM2 dimer (1880 Å^2). Despite the different dimer shapes, the protomers from the two structures are very similar with differences limited to two helices, α0 and α4 (**Fig. 3.3B**). In the unliganded CNNM3 structure, helix α4 mediates all of the dimerization contacts; the four hydrophobic residues (L437, I441, I445, and I449) of α4 interact with the same residues from

another protomer in a complementary order (**Fig. 3.3C**). While novel for CNNM proteins, the open V-shaped dimer is similar to the CBS-pair domain dimer observed in ClCs [132-137].

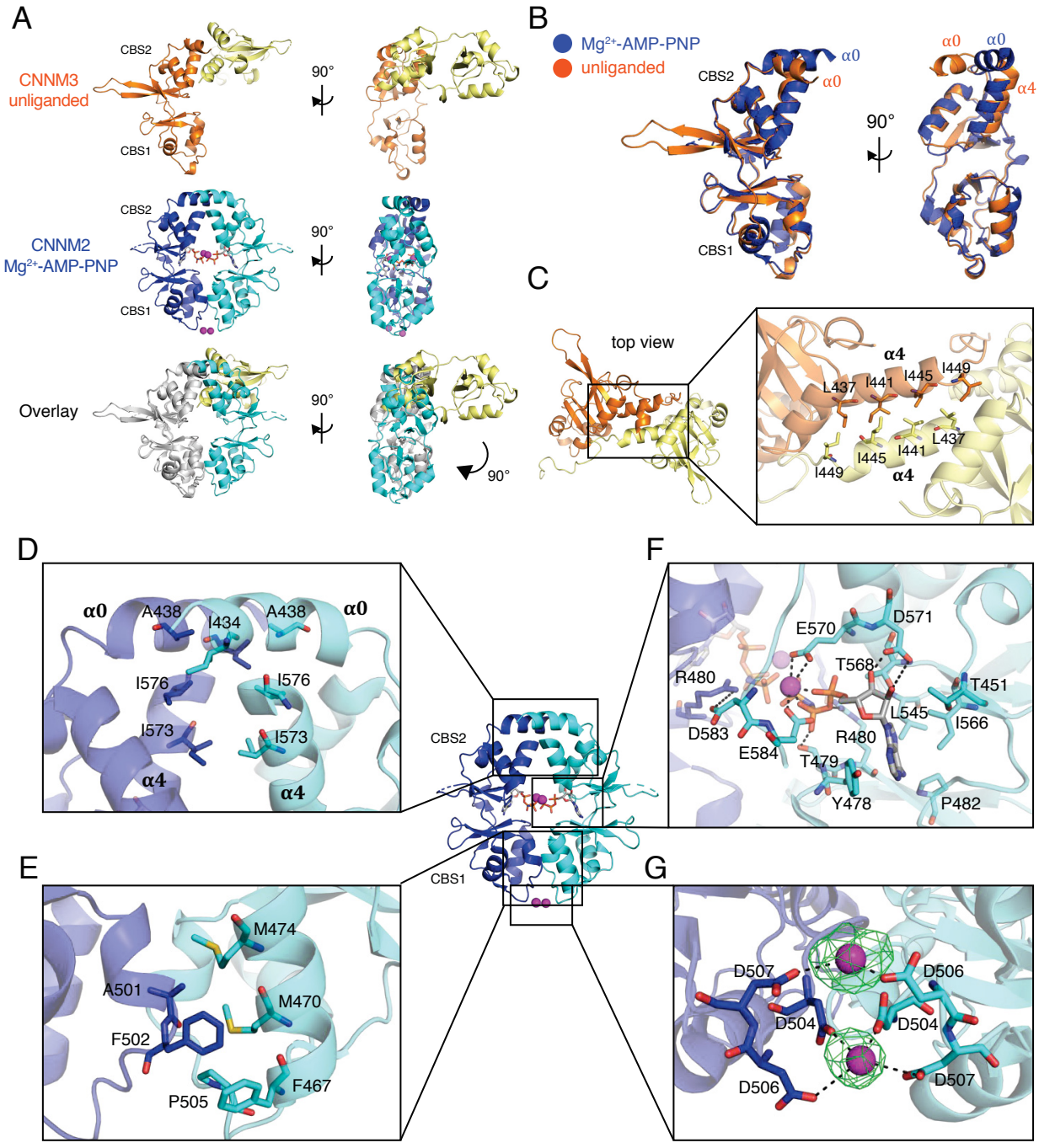

Figure 3.3 CBS modules undergo conformational changes upon Mg^{2+}-AMP-PNP binding

(A) Structural comparison of the CNNM3 and CNNM2 CBS-pair domains. The CBS-pair domain dimerization interface undergoes a 90° rotation upon Mg^{2+}-AMP-PNP binding. (B)

Structural overlay of CBS-pair domain of CNNM3 (*orange*) and CNNM2 (*blue*) showing a shift in the α0 helix. (C) CBS-pair dimerization in CNNM3 is mediated by hydrophobic contacts of α4 helix in CBS2 motif. (D and E) Close-up view of the dimerization interface in CBS2 and CBS1 motifs. CBS-pair dimerization in CNNM2 is mediated by hydrophobic contacts of α0 and α4 helices in CBS2 and hydrophobic contacts in CBS1 motifs. (F) Mg^{2+}-AMP-PNP binds to the canonical nucleotide-binding site. (G) Two Mg^{2+} ions (*magenta*) found in the second Mg^{2+}-binding region. The electron density F_o-F_c omit map is contoured at 3.0 σ.

The CNNM2 CBS-pair domain forms a flat disc-like dimeric structure involving extensive contacts between both CBS motifs (**Fig. 3.3D & E**). The structure is similar to the structure of the isolated CBS-pair domain with Mg^{2+}-ATP [91] but flatter due to a 10° rotation around the dimer interface (**Fig. 3.4**). Contacts in the α0 helix are mediated by I434 and A438 and in the α4 helix by residue I573 (**Fig. 3.3D**). Since the α0 helix leads directly to the N-terminal transmembrane domain, the conformational differences between the two states are likely to translate to the transmembrane helices and affect transport activity. Additional dimerization contacts are mediated by residues A501 and F502 of one protomer interacting with F467, M470, M474, and P505 of the other (**Fig. 3.3E**). Mg^{2+}-AMP-PNP is bound in the canonical nucleotide-binding site observed in other CBS-pair domains (**Fig. 3.3F** and **Fig. 3.5A**). The adenine base of AMP-PNP is positioned by L545, T451, and Y478. The ribose moiety of ATP is stabilized by D571 and T568. The phosphate groups interact with R480 and T479. The Mg^{2+} is coordinated by E570 from the α4 helix and the three phosphates of ATP.

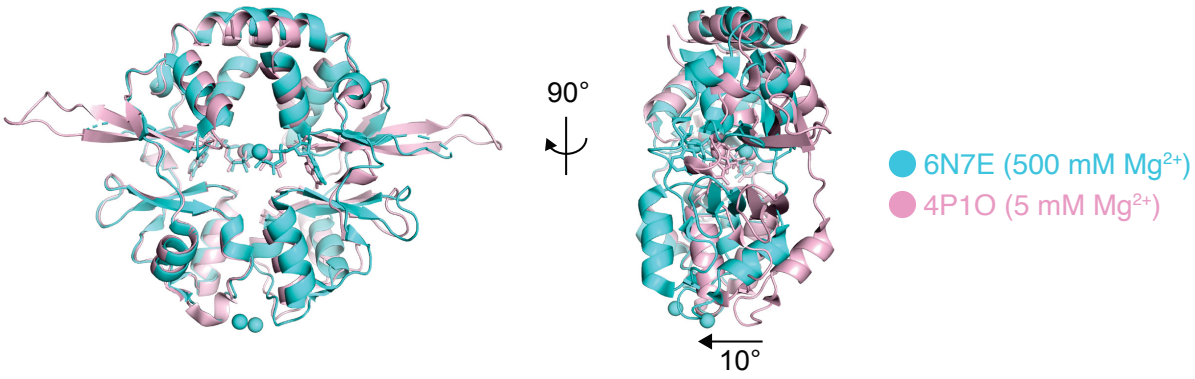

Figure 3.4 Structural comparison of CNNM2 CBS module structures

CNNM2 CBS module from this study (*cyan*) shows a 10° shift at the dimer interface relative to the previously reported structure (*pink*).

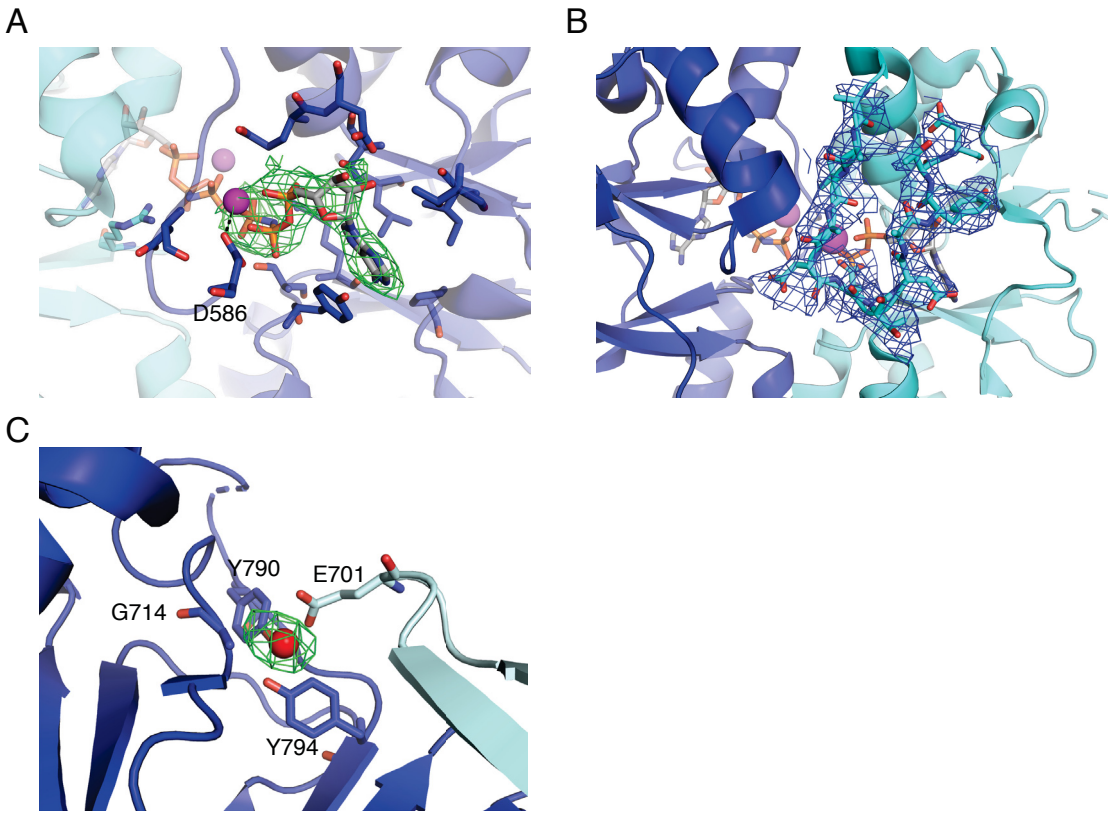

Figure 3.5 Electron density in CNNM2 cytosolic fragment structure

(A) Representative F_o-F_c omit map for Mg^{2+}-AMP-PNP, contoured at 3.0 σ. (B) Representative $2F_o$-F_c map for the linker around Mg^{2+}-AMP-PNP site, contoured at 1.0 σ. (C) Representative F_o-F_c omit map for a water molecule, contoured at 3.0 σ.

3.3.2 Novel features of the closed CBS-pair domain dimer of CNNM2

Two new densities were observed around acidic residues D504, D506, and D507 at the bottom of CBS1 motif of both protomers (**Fig. 3.3G**). As this cluster of acidic residues had previously been hypothesized to bind Mg^{2+} ions [91], we modeled Mg^{2+} ions into the densities. The high concentration of Mg^{2+} (500 mM) in the CNNM2 crystallization buffer likely promotes binding to these weak Mg^{2+}-binding sites and may additionally be responsible for flattening the dimer (**Fig. 3.4**).

We also observed electron density for the interdomain linker connecting CBS-pair and CNBH domains of CNNM2 (**Fig. 3.5B**). The linker residues were absent in the previous structures of CNNM CBS-pair domains with bound nucleotides [91]. We observed that acidic residues, E584 and D586, in the linker make interactions with the ATP-coordinated Mg^{2+} ion (**Fig. 3.3F** and **Fig. 3.5A**). Additionally, acidic aspartate residue D583 interacts with R480 from another protomer, further strengthening the dimerization contact.

3.3.3 Mutagenesis of the CBS-pair domain

To validate the importance of residues from the CBS-pair domain structures, we first established an ATP binding assay by ITC. In presence of constant concentration of Mg^{2+}, the cytosolic fragment of CNNM4 has highest affinity for ATP (2.8 μM), followed by CNNM2 (4.3 μM), while CNNM3 shows no binding (**Fig. 3.6A** and **Table 3.2**). These results agree with previous observations [41]. To test the effect of mutations, we chose to use CNNM4, which has the highest binding affinity and activity in a cellular Mg^{2+} assay [41]. The CBS-pair domains of the CNNM proteins are very similar (90% identity, 97% similar), so there is no ambiguity identifying residues in CNNM4 that correspond to features in the crystal structures (**Fig. 3.7** and **Table 3.3**). As expected, mutation of the majority of residues in the ATP-binding site completely abolished ATP binding (**Table 3.2** and **Fig. 3.8**). The sole exception was E497A, which had only a mild effect. The disease-causing mutations, R407L, P409L, and T495I, all prevented ATP binding.

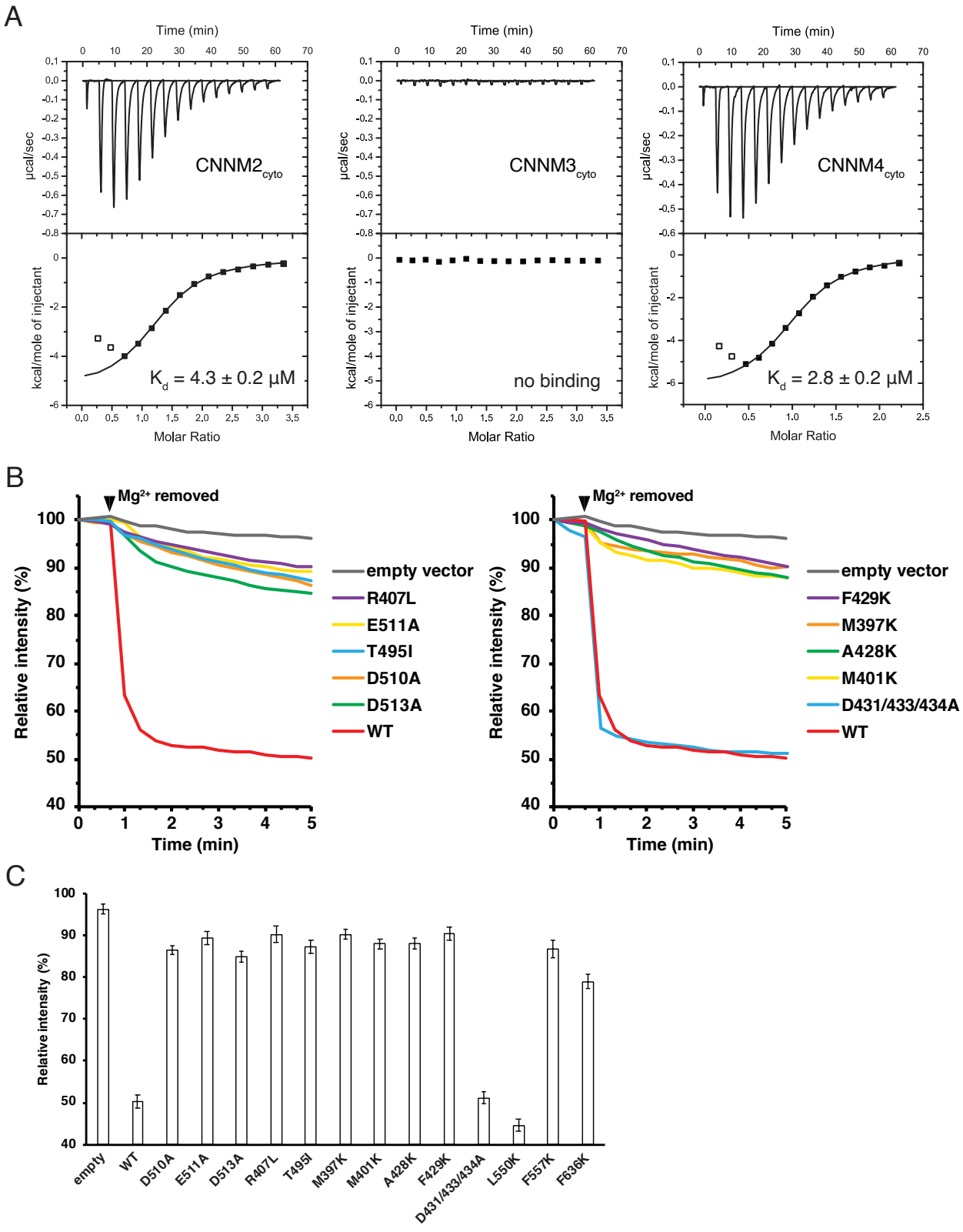

Figure 3.6 Functional characterization of CBS-pair domain mutants by ITC and Mg^{2+} efflux assays

(A) ITC experiments of cytosolic fragments of CNNM2-4 (30 μM) binding to ATP (450, 450, and 300 μM) in presence of Mg^{2+}. The upper panel shows the thermogram. The lower panel shows the integrated areas from the injection peaks (*squares*) and a fitting assuming single set of identical binding sites. The open squares were not included in the fit. (B) HEK293T cells transfected with the indicated constructs were loaded with Magnesium Green and then subjected to Mg^{2+} depletion at the indicated time point (*arrowhead*). The mean relative fluorescence intensities of ten cells are shown in the graph. Mutating acidic residues in the linker (D510, E511, and D513), disease-relevant residues (R407 and T495), and residues in the CBS1 dimerization interface (M397, M401, A428, and F429) in CBS-pair domain abolished Mg^{2+} efflux activity. Mutating acidic residues in the second Mg^{2+}-binding region (D431, D433, and D434) had no effect. (C) Comparison of relative fluorescence intensities of ten cells for all mutants after 5 min of Mg^{2+} depletion. The data are shown as mean ± standard error of mean. Values for L550K, F557K, and F636K are from **Fig. 3.13D**.

Table 3.2 Summary of estimated ATP binding affinities for CNNM cytosolic fragments in presence of 50 mM Mg^{2+} by ITC

Cytosolic fragments	K_d (μM)	
CNNM2	4.3 ± 0.2	
CNNM3	-[1]	
CNNM4	2.8 ± 0.2	
$CNNM4_{cyto}$ mutants		Location
T378A (T451)[2]	-	Mg^{2+}-ATP binding site
Y405A (Y478)	-	
R407L[3] (R480)	-	
P409L[3] (P482)	-	
L493A (I566)	-	
T495I[3] (T568[3])	-	
E497A (E570)	18 ± 2	
D498A (D571)	-	
D510A (D583)	250 ± 10	
E511A (E584)	250 ± 20	
D513A (D586)	300 ± 60	
M397K (M470)	240 ± 40	CBS1 dimerization interface
M401K (M474)	240 ± 30	
A428K (A501)	170 ± 20	
F429K (F502)	220 ± 20	
D431A/D433A/D434A (D504/D506/D507)	5.5 ± 0.3	

Raw thermograms are shown in **Fig. 3.8**
[1]no binding detected
[2]CNNM2 residue numbers in parentheses
[3]disease-causing mutation

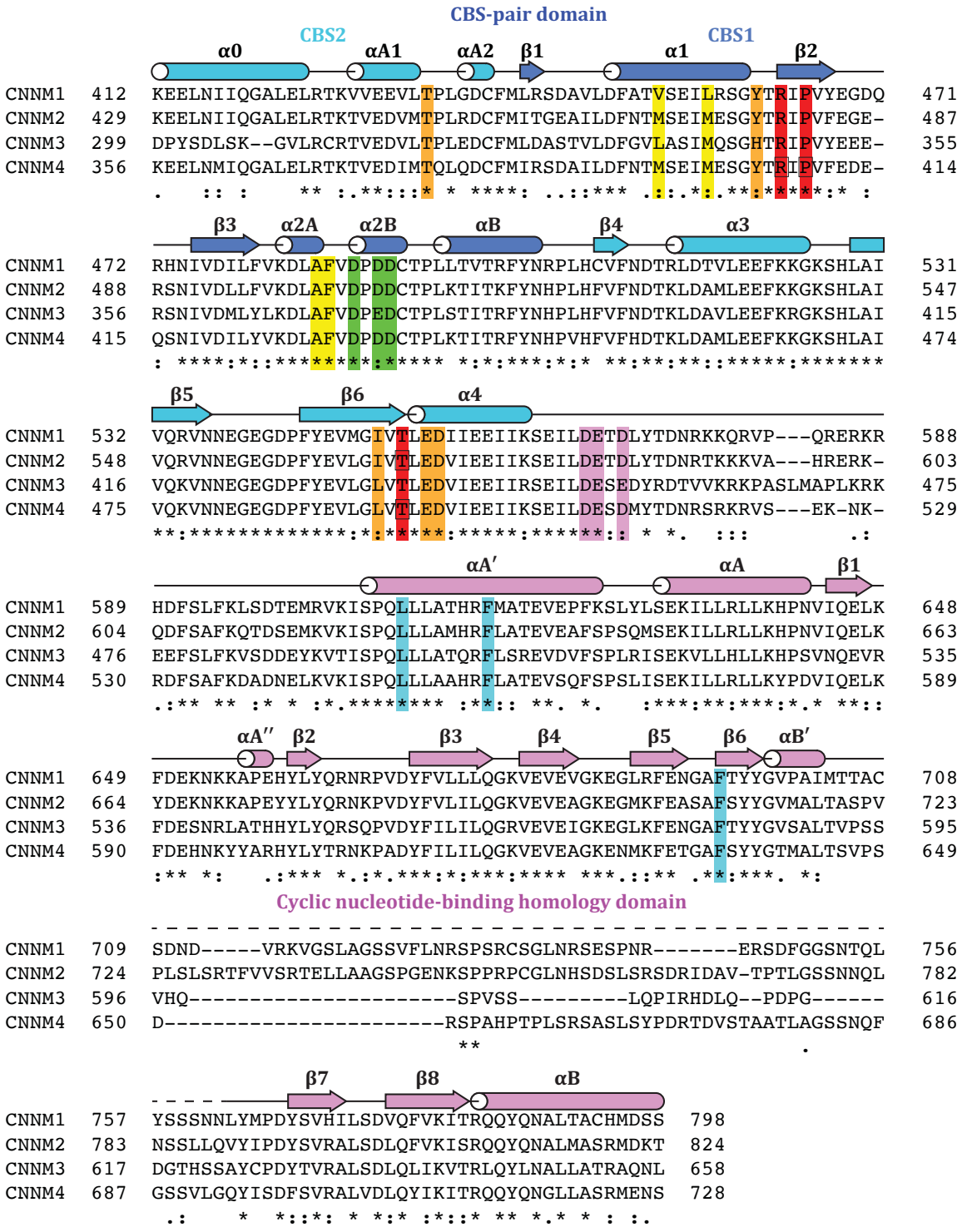

Figure 3.7 Sequence alignment of cytosolic fragment of human CNNM proteins

Secondary structure corresponds to the crystal structure of CNNM2 cytosolic fragment. Highlighted residues: canonical Mg^{2+}-ATP binding site (*orange*), acidic residues in newly observed Mg^{2+} binding site (*green*), disease associated mutations (*red*; associated isoform is

boxed), linker residues involved in Mg^{2+}-ATP binding (*pink*), residues lining CBS1 dimerization interface (*yellow*), and residues in the new CNBH dimerization interface (*cyan*).

Table 3.3 Residue correspondence for mutants tested between different CNNM isoforms

Location	CNNM2		CNNM3		CNNM4	
	Residue	Number	Residue	Number	Residue	Number
Mg^{2+}-ATP binding site	T	451	T	319	T	378
	Y	478	H	346	Y	405
	R	480	R	348	R	407
	P	482	P	350	P	409
	I	566	L	434	L	493
	T	568	T	436	T	495
	E	570	E	438	E	497
	D	571	D	439	D	498
	D	583	D	451	D	510
	E	584	E	452	E	511
	D	586	D	454	D	513
CBS1 dimerization interface	M	470	L	338	M	397
	M	474	M	342	M	401
	A	501	A	369	A	428
	F	502	F	370	F	429
	D	504	D	372	D	431
	D	506	E	374	D	433
	D	507	D	375	D	434
V-shaped CNBH dimerization interface	L	624	L	496	L	550
	F	631	F	503	F	557
	F	710	F	582	F	636
Flat-shaped CNBH dimerization interface	A	698	I	570	A	624
	M	703	L	575	M	629
	F	705	F	577	F	631

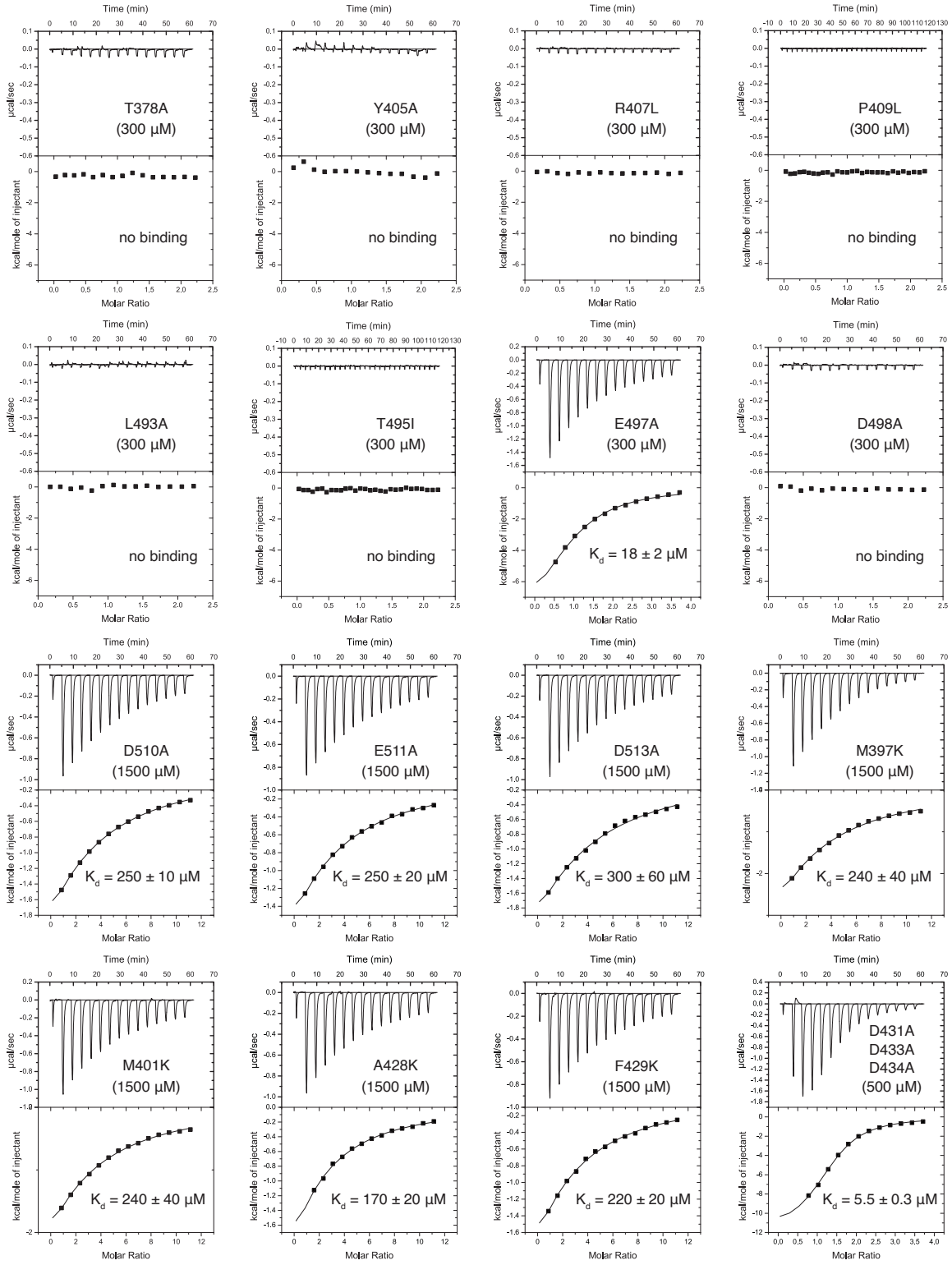

Figure 3.8 ITC thermograms of various CNNM4$_{cyto}$ mutants (30 µM) binding to ATP in presence of 50 mM Mg^{2+}

The concentrations of ATP are indicated in parentheses.

As suggested previously, the residues lining the ATP-binding cavity resemble those of ABC transporters [91]. To test whether CNNM proteins possess ATPase activity, we performed an ATP hydrolysis assay on cytosolic fragments of CNNM2-4 along with apyrase, an ATP-diphosphohydrolase (**Fig. 3.9**). We did not detect ATPase activity with all three CNNM members, suggesting that while ATP can bind to CNNM proteins, they lack or have very low ATPase activity.

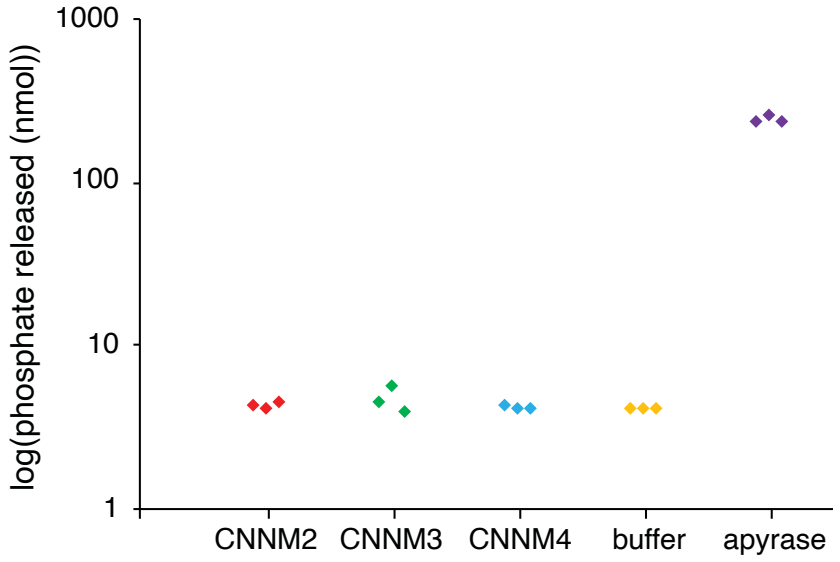

Figure 3.9 ATP hydrolysis assay of cytosolic fragments of CNNM2-4 (1µM), buffer only, and apyrase (0.1 unit, positive control)

All assays were performed in triplicate. Individual measurements are plotted.

To interrogate the importance of the interdomain linker for binding Mg^{2+}-ATP, we mutated D510, E511, or D513 in CNNM4 (equivalent to D583, E584, and D586 in CNNM2) to alanine. All three mutations reduced the affinity for Mg^{2+}-ATP by 100-fold (**Table 3.2** and **Fig. 3.8**), confirming that the interdomain linker plays a significant role in binding and stabilizing Mg^{2+}-ATP.

Furthermore, to investigate the importance of dimerization of CBS1 interface for binding Mg^{2+}-ATP, we mutated the hydrophobic residues lining the interface (**Fig. 3.3E**). Surprisingly, when the CNNM4 residues, M397, M401, A428, and F429, were mutated to lysine, the affinity for ATP was strongly reduced (**Table 3.2** and **Fig. 3.8**), although the mutated residues do not directly interact with ATP. We also tested the second Mg^{2+}-binding region (**Fig. 3.3G**). Simultaneous mutation of all three CNNM4 aspartate residues, D431, D433, and D434, to alanine had only a small 2-fold effect on ATP binding (**Table 3.2** and **Fig. 3.8**).

3.3.4 CNNM activity in cells

We used a cellular Mg^{2+} efflux assay to assess the effect of mutations on CNNM transport activity [20]. The assay measures the change in the intracellular free Mg^{2+} upon removal of Mg^{2+} from the extracellular milieu (**Fig. 3.6B**). CNNM4 has the highest activity of the four members [41] and was used to test the effects of the mutations. As controls, immunofluorescence imaging was used to confirm that the mutant proteins were correctly localized on the cell membrane (**Fig. 3.10A**) and western blotting was used to confirm protein expression of the mutants (**Fig. 3.10B**).

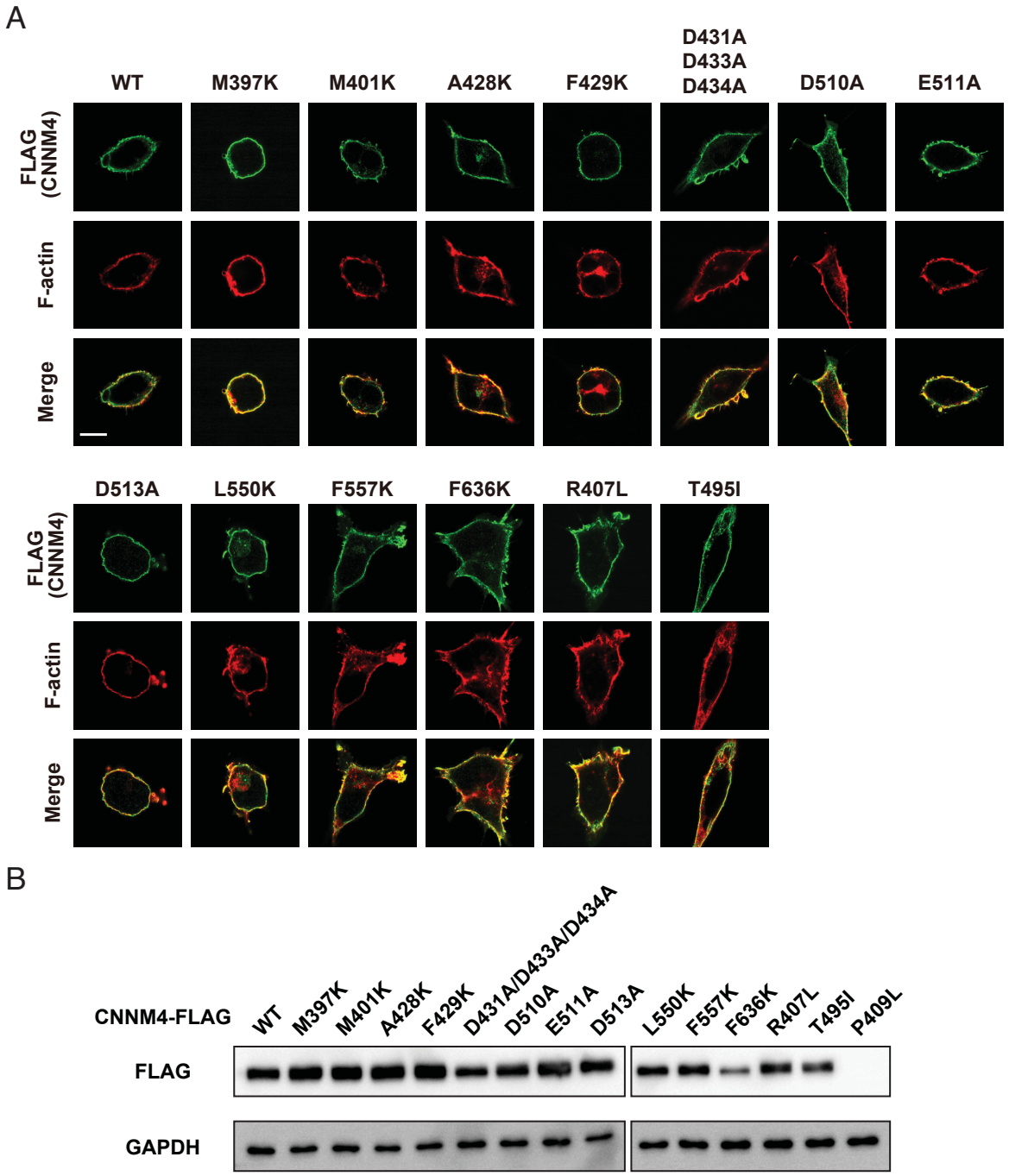

Figure 3.10 Mg^{2+} efflux assay control experiments

(A) Immunofluorescence images of HEK293T cells with anti-FLAG (*green*) and rhodamine-phalloidin (*red*) showing that CNNM4 WT and mutant proteins are properly colocalized with F-actin adjacent to the cell membrane. *Bar*, 10 μm. (B) Western blotting showing expression of CNNM proteins in lysates of HEK293T cells transfected with the indicated constructs.

All of the mutations that disrupted ATP binding also severely impaired Mg^{2+} efflux activity (**Fig. 3.6B & C**). This includes mutants of acidic linker residues, disease-causing mutations, and the four mutants that disrupt CBS1 dimerization interface. Although correlative, the results strongly suggest that Mg^{2+}-ATP binding is required for CNNM Mg^{2+} efflux. On the other hand, loss of the three aspartic acid residues that constitute the second Mg^{2+}-binding region had no effect on cellular Mg^{2+} efflux, demonstrating that the bound Mg^{2+} ions are not required.

3.3.5 Correlation of CBS-pair dimerization and Mg^{2+}-ATP binding

The loss of binding affinity in dimerization mutants suggested that the two activities may be linked. To test this, we analyzed oligomerization of CBS-pair domains of CNNMs by SV-AUC. We first performed AUC experiments with CBS-pair domains of CNNM1-4 in absence of any ligand and found that they all behaved as monomers (**Fig. 3.11A**, **Fig. 3.12** and **Table 3.4**). When Mg^{2+}-ATP was added to $CNNM4_{CBS}$, the member with the highest affinity, we observed the presence of a dimeric species (**Fig. 3.11B**). Addition of Mg^{2+}-AMP or Mg^{2+}-ADP did not induce dimer formation. The presence of a dimer was easier to detect in the presence of PRL2, which binds to CNNM CBS-pair domains with high affinity [96]. Addition of Mg^{2+}-ATP but not Mg^{2+} or ATP alone led to the formation of a dimeric species (**Fig. 3.11C**). Similarly, disease-causing mutations in the CBS-pair domain that prevent Mg^{2+}-ATP also prevented dimer formation (**Fig. 3.11D**).

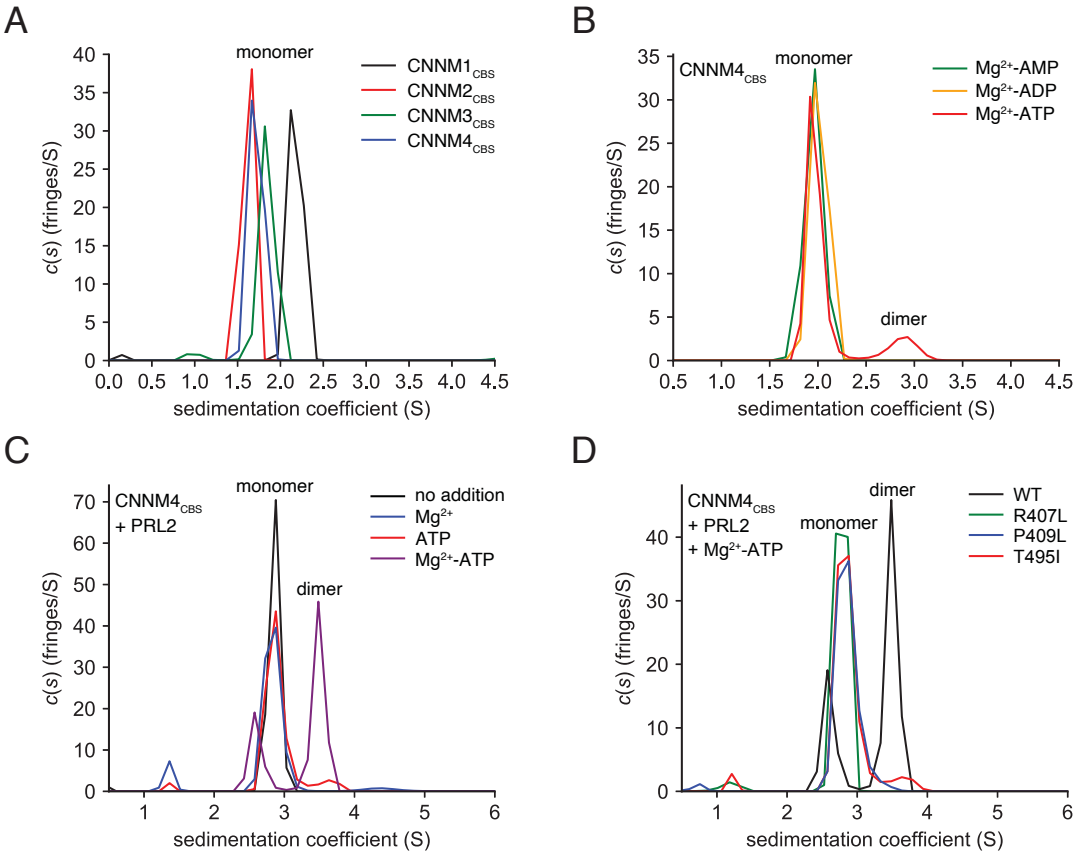

Figure 3.11 CBS-pair domain dimerization depends on Mg^{2+}-ATP binding and is enhanced by PRL binding

(A) Sedimentation velocity analytical ultracentrifugation (SV-AUC) experiments of CBS-pair domains of CNNM1-4. All sediment as a monomer. (B) SV-AUC experiments of $CNNM4_{CBS}$ with 1 mM AMP, ADP, or ATP in presence of 10 mM $MgCl_2$. A dimeric species is observed only in presence of Mg^{2+}-ATP. (C) SV-AUC experiments of $CNNM4_{CBS}$-PRL2 complex in presence of 1 mM ATP and/or 10 mM $MgCl_2$. A dimeric species is observed only in presence of Mg^{2+}-ATP. The dimer/monomer ratio is higher in presence of PRL. (D) SV-AUC experiments of CBS4-PRL2 complexes with CNNM4 disease-associated mutants (R407L, P409L, and T495I) in presence of 1 mM ATP and 10 mM $MgCl_2$. All three mutants prevented dimer formation.

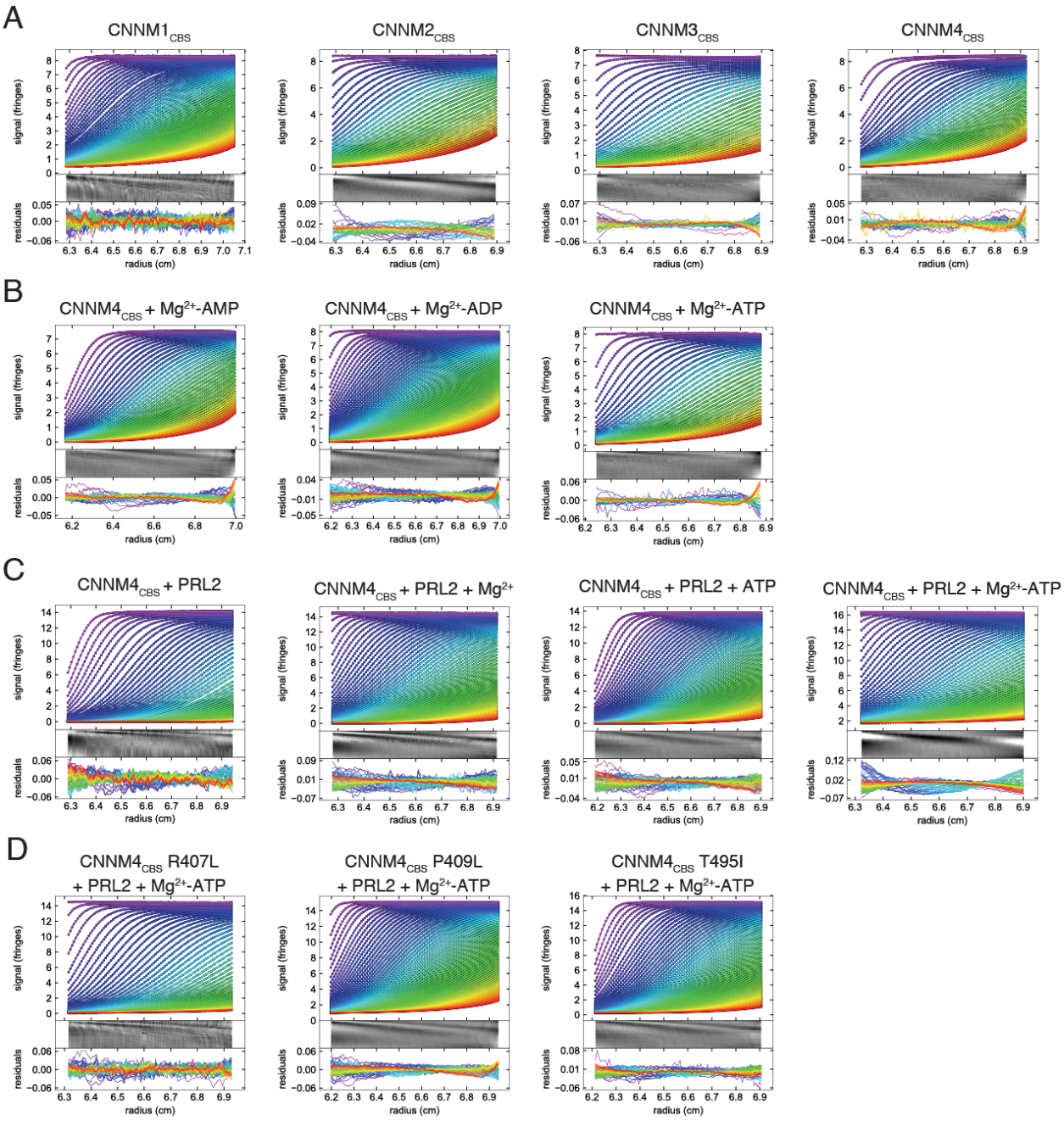

Figure 3.12 Sedimentation velocity AUC profiles of 100 µM purified proteins

Interference of the sample are plotted against the radial position in the cell. One in every 15 scans is plotted. (A) CBS-pair domain of CNNM1-4. (B) CBS-pair domain of CNNM4 with Mg^{2+}-AMP, Mg^{2+}-ADP or Mg^{2+}-ATP. (C) CBS-pair domain of CNNM4 and PRL2 in different conditions (no addition, Mg^{2+}, ATP, or Mg^{2+}-ATP). (D) CBS-pair domain of CNNM4 mutants (R407L, P409L & T495I) and PRL2 with Mg^{2+}-ATP.

Table 3.4 SV-AUC sedimentation coefficients and estimated molecular weights

		Sedimentation coefficient (S)		Estimated MW (kDa)		RMSD	Theoretical MW (kDa)	
Protein	Condition	Peak 1	Peak 2	Peak 1	Peak 2		Monomer	Dimer
$CNNM1_{CBS}$	no addition	2.09	-	18.8	-	0.0051	18.0	36.1
$CNNM2_{CBS}$	no addition	1.83	-	17.7	-	0.0039	17.9	35.9
$CNNM3_{CBS}$	no addition	1.86	-	18.7	-	0.0049	17.6	35.2
$CNNM4_{CBS}$	no addition	1.73	-	18.3	-	0.0037	18.1	36.2
	Mg^{2+}-ATP	1.96	2.87	19.1	42.1	0.0045		
	Mg^{2+}-ADP	2.02	-	17.8	-	0.0042		
	Mg^{2+}-AMP	1.97	-	18.3	-	0.0050		
$CNNM4_{CBS}$ + PRL2	no addition	2.85	-	38.2	-	0.0034	38.8	77.7
	Mg^{2+}	2.83	-	38.9	-	0.0040		
	ATP	2.85	-	37.7	-	0.0041		
	Mg^{2+}-ATP	2.61	3.61	39.9	73.1	0.0054		
$CNNM4_{CBS}$ R407L + PRL2	Mg^{2+}-ATP	2.78	-	36.9	-	0.0051	38.8	77.7
$CNNM4_{CBS}$ P409L + PRL2	Mg^{2+}-ATP	2.84	-	39.4	-	0.0051	38.8	77.7
$CNNM4_{CBS}$ T495I + PRL2	Mg^{2+}-ATP	2.83	-	36.9	-	0.0055	38.8	77.7

3.3.6 Structures of the CNBH domain

In fashion similar to the CBS-pair domains, the CNHB domains in the two crystal structures show differences in their mode of dimerization (**Fig. 3.13A**). The CNBH domain in the CNNM3 crystals displays a previously unreported, V-shaped mode of dimerization with an interface formed by β4 and β5 of one protomer (residues I570, L575, F577) and αA′ (L496, F503) and β6 (F582) of the other protomer (**Fig. 3.13B**). In contrast, the domains in CNNM2 crystals dimerize using the flat-shaped dimerization interface seen in crystals of the isolated CNBH domains from CNNM2 and CNNM3 [131]. This involves hydrophobic residues (A698, M703, and F705) from strands β4 and β5 of both protomers (**Fig. 3.13C**). The result is a 90° rotation between the relative orientations of protomers in the two CNBH dimers (**Fig. 3.13A**).

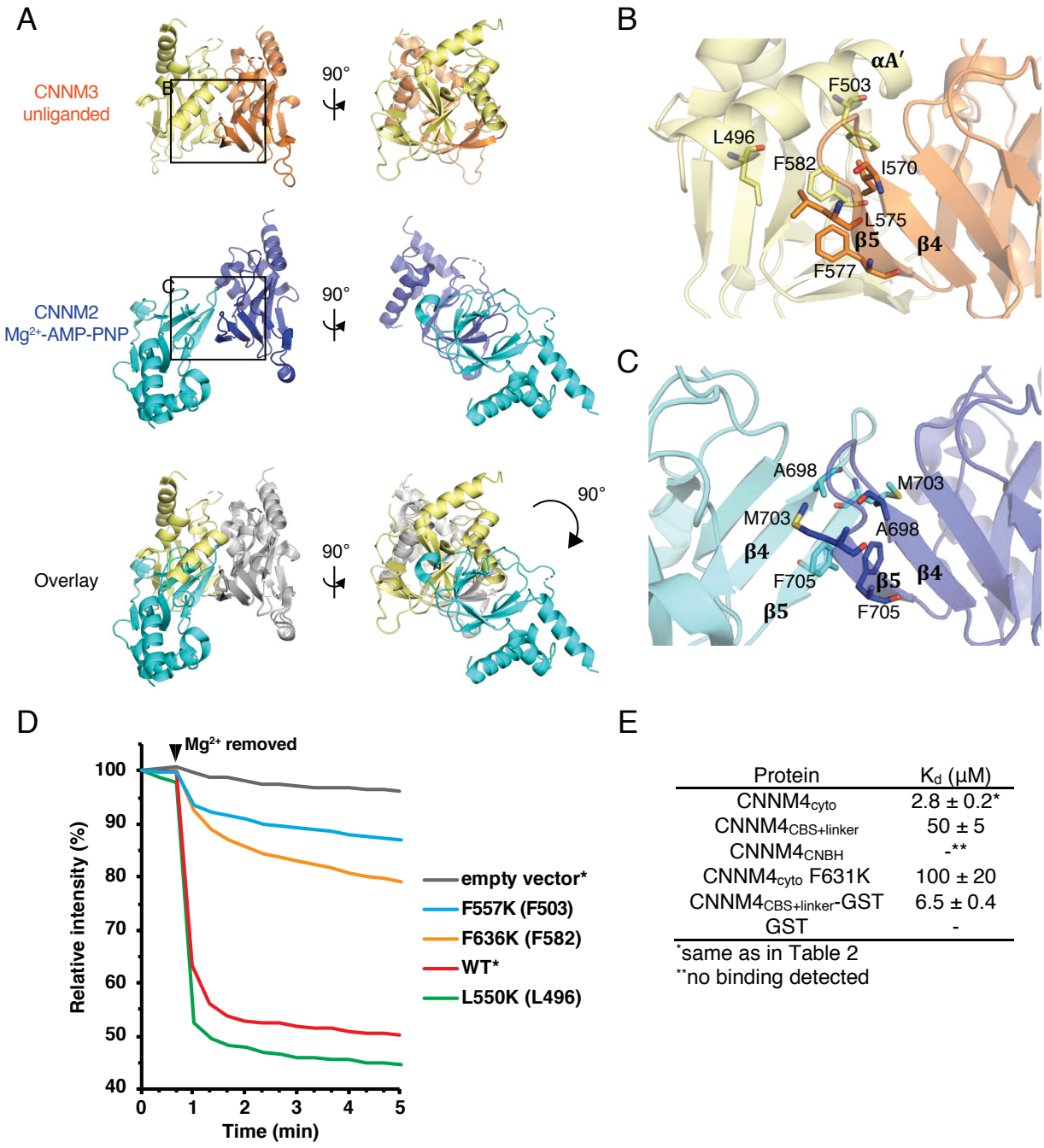

Protein	K_d (μM)
$CNNM4_{cyto}$	2.8 ± 0.2*
$CNNM4_{CBS+linker}$	50 ± 5
$CNNM4_{CNBH}$	-**
$CNNM4_{cyto}$ F631K	100 ± 20
$CNNM4_{CBS+linker}$-GST	6.5 ± 0.4
GST	-

*same as in Table 2
**no binding detected

Figure 3.13 Conformational changes in CBS-pair domain are translated to the CNBH domain

(A) Structural comparison of the CNBH domains in the two structures. The CNBH domain also undergoes a 90° rotation upon Mg^{2+}-AMP-PNP binding. (B) Dimerization is mediated through hydrophobic contacts of β-roll of one protomer and αA' helix of the other protomer. (C) Dimerization is mediated through hydrophobic contacts of β-roll of both protomers. (D)

HEK293T cells transfected with the indicated constructs were loaded with Magnesium Green and then subjected to Mg^{2+} depletion at the indicated time point (arrowhead). The mean relative fluorescence intensities of 10 cells are shown in the graph. Mutating hydrophobic residues (F557 and F636) in the V-shaped CNBH dimerization interface abolished Mg^{2+} efflux activity. Residue numbers in CNNM3 are in parentheses. Curves marked by an asterisk (*) are taken from **Fig. 3.6B** for comparison. (E) The CNBH domain increases ATP-binding affinity of the CBS-pair domain. The raw thermograms are shown in **Fig. 3.14**.

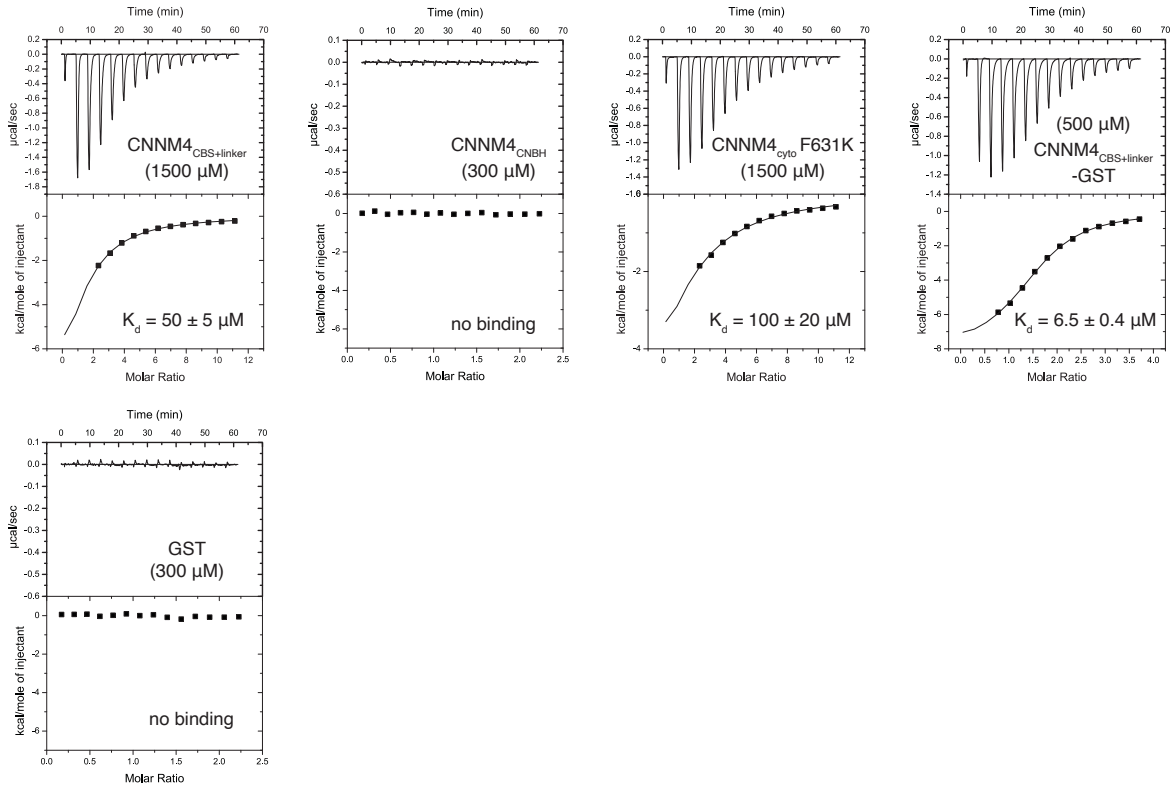

Figure 3.14 ITC thermograms of various proteins (30 µM) binding to ATP in presence of 50 mM Mg^{2+}

The concentrations of ATP are indicated in parentheses.

We used mutagenesis to test the significance of the V-shaped dimerization interface. Mutating CNNM4 F557K (equivalent to CNNM3 F503K) and CNNM4 F636K (F582K) each

reduced Mg^{2+} efflux activity (**Fig. 3.6C**, **Fig. 3.13D**, and **Fig. 3.10**). The reduction for F636K could be due to lower protein expression (**Fig. 3.10**). On the other hand, CNNM4 L550K (L496K) consistently showed a slight increase in efflux. Previous mutagenesis of the CNBH domain showed similar divergent effects [131]. CNNM4 mutations M629K (L575K) and F631K (F577K) both blocked CNBH dimerization but M629K showed normal efflux while F631K was impaired.

3.3.7 CBS-pair dimerization is required for high-affinity Mg^{2+}-ATP binding

Previous studies of CNNM CBS-pair domains reported significantly weaker ATP binding affinities than the low micromolar affinity measured by ITC [41, 91]. As our experiments used the CNNM4 cytosolic fragment containing both CBS-pair and CNBH domains, we hypothesized that presence of the CNBH domain increased the affinity of the CBS-pair domain for Mg^{2+}-ATP. To test this, we measured the ATP-binding affinity for the CBS-pair and CNBH domains separately (**Fig. 3.13E** and **Fig. 3.14**). Without the CNBH domain, the K_d for the CBS-pair domain increased from 2.8 μM to 50 μM. The CNBH domain alone showed no binding. The correlation between dimerization and Mg^{2+}-ATP binding suggested that the effect of the CNBH domains is to promote CBS-pair domain dimerization. To test this, we measured the affinity of CNNM4 cytosolic fragment with a F631K mutation that prevents CNBH dimerization [131]. The mutant protein showed the same reduction in ATP affinity, suggesting that CNBH dimerization is required for high-affinity ATP binding (**Fig. 3.13E** and **Fig. 3.14**). Finally, we replaced CNBH domain with glutathione-S-transferase (GST), another dimerizing domain with no ATP-binding activity. The affinity of the resulting fusion protein was close to that of the original CNNM4 fragment, confirming that dimerization is sufficient to increase the affinity of the CBS-pair domain.

3.3.8 Detailed analysis of the ITC thermograms

Additional evidence for the coupling between dimerization and Mg^{2+}-ATP binding can be derived from the shape of the ITC thermograms. We observed that the titration curves cannot be completely fit using a binding model of independent, identical sites. Specifically, the ITC profile for the wild-type CNNM4 cytosolic fragment displays a significant increase in heat evolution in the first four titration points before declining due to saturation of the binding sites

(**Fig. 3.6A**, top panel). While the first injection is expected to show a smaller integrated area because of the reduced volume injected and dilution prior to the start of the experiment, the increase for the following injections is unusual. In order to extract an estimate of the affinity, the initial data points were removed, and the remaining titration profile was fit with a simple 1:1 binding model (**Fig. 3.6A**, bottom panel). Thus, the ITC fitting results in **Table 3.2** and **Fig. 3.13E** should be treated as relative measures of Mg^{2+}-ATP-binding affinity.

To better understand the anomalous titrations, we performed a series of ITC experiments at different Mg^{2+} concentrations (**Fig. 3.15A**). The shapes of the titration profiles varied strongly depending on the Mg^{2+} concentration. The thermogram at 50 mM Mg^{2+} (red symbols in **Fig. 3.15A**) showed an initial dip and started to saturate at a one-to-one stoichiometric ratio of ATP to protein. At lower Mg^{2+} concentrations, the dip is less pronounced and much higher concentrations of ATP are required to achieve saturation.

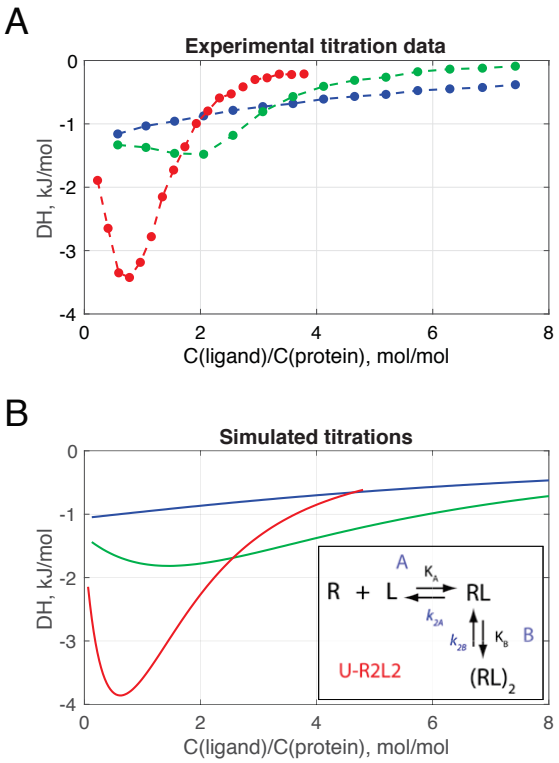

Figure 3.15 Qualitative analysis of Mg^{2+}-ATP binding

(A) ITC thermograms for titrations of 30 µM $CNNM4_{cyto}$ with ATP in the presence of 10 mM (*blue*), 20 mM (*green*), and 50 mM $MgCl_2$ (*red*) show complex behavior indicative of multiple states. (B) Titration curves, simulated for a U-R2L2 model with dissociation constants K_A =

333 μM and K_B = 333 μM (*blue*), K_A = 250 μM and K_B = 33 μM (*green*), K_A = 200 μM and K_B = 2 μM (*red*).

As a possible explanation for the anomalous behavior, we simulated the titrations using a ligand-binding, receptor-dimerization (U-R2L2) model in the LineShapeKin Simulation software [138] (**Fig. 3.15B**). This model stipulates that the ligand-receptor complex can dimerize, which then blocks ligand dissociation [139]. To compare predictions of this model with experimental data, we simulated the titration profiles while adjusting the affinity constants for the two steps of the binding process (**Fig. 3.15B**). While the U-R2L2 model is an oversimplification of our system, it still closely reproduced the most salient features of the experimental titrations. Of particular note, increasing the Mg^{2+} concentrations increased CBS-pair dimerization, in agreement with a role of the domains in Mg^{2+} sensing. In future work, we will refine the model to include separate binding constants for ATP and Mg^{2+} and the possibility of other states such as CBS-pair dimerization with only one ligand bound (R2L1).

3.4 Discussion

Genetic studies show that eukaryotic CNNM proteins are involved in divalent cation transport in organisms from bacteria to yeast and humans. Loss of CNNM proteins decreases Co^{2+} toxicity in bacteria [37] and yeast [36], and mutations in *CNNM2* cause hypomagnesemia in humans [19, 42]. However, the precise biochemical function of CNNM proteins remains unknown. The number of transmembrane helices (six for a dimer) in the CNNM DUF21 transmembrane region is lower than that in typical Mg^{2+} channels/transporters, which has been suggested to indicate that CNNM proteins regulate other transporters rather than acting as transporters themselves [32]. On the other hand, the deep conservation of CNNM-like proteins throughout the bacterial, plant, and animal kingdoms implies conservation of function, which would require co-conservation of any partner transporter – an unlikely proposition.

Across all kingdoms, DUF21 transmembrane domains are almost invariantly followed by a CBS-pair domain, a regulatory domain originally identified in CBS [92]. CBS-pair domains typically self-associate to form disc-like assemblies classified as parallel, anti-parallel, and V-shaped dimers, depending on the orientation of the two protomers [140]. All previous structures of CNNM CBS-pair domains except for one have adopted the compact, parallel conformation that we observe for CNNM2 [91, 96-98]. The open, V-shaped CNNM3 dimer is the first for a CNNM CBS-pair domain (**Fig. 3.3A**). CBS-pair domains are found in a wide variety of proteins and typically act as sensors for nucleotides or metal ions [140]. For instance, through conformational changes, the CBS-pair domains of the bacterial Mg^{2+} transporter MgtE act as Mg^{2+} sensor: under low-Mg^{2+} conditions, the dimer interface between the CBS2-CBS2′ motifs of MgtE is loosened by the repulsive forces of conserved acidic residues, leading to an open conformation [141-143]. In contrast, under high-Mg^{2+} conditions, Mg^{2+} ions bind to these acidic clusters, promoting the CBS module to a closed dimeric assembly [141-143]. These structural changes are transmitted to the transmembrane domain, thereby controlling the gating of the ion-conducting pore [143].

In CNNMs, the CBS-pair domain likely plays a similar regulatory role with an open-to-closed conformational change driven by Mg^{2+}-ATP binding (**Fig. 3.16**). Our crystal structures revealed a loose dimeric assembly in the ligand-free state and a closed assembly with Mg^{2+}-ATP binding (**Fig. 3.3A**). The closed conformation appears to be required for Mg^{2+} efflux activity as all the mutations that abolished Mg^{2+}-ATP binding also prevented Mg^{2+} efflux (**Table 3.2** and

Fig. 3.6B). The cellular concentration of ATP is roughly millimolar [95], which is much higher than the CNNM4 affinity measured by ITC (**Fig. 3.6A**) or filter binding assays [41], suggesting that the binding site would always be occupied *in vivo*. Nonetheless, we observed that affinity for ATP is strongly influenced by the protein context (**Fig. 3.13E**) and free Mg^{2+} concentration (**Fig. 3.15**). These likely alter the physiological affinity of the intact protein in cells. The structural mechanism by which millimolar Mg^{2+} affects ATP binding is unclear. The affinity of Mg^{2+} for ATP is in the micromolar range [144, 145], making formation of Mg^{2+}-ATP an unlikely source for the Mg^{2+} effect. Similarly, while we observed Mg^{2+} ions weakly bound at the interface between the CNNM2 CBS1 motifs (**Fig. 3.3G**), loss of the Mg^{2+} binding sites had only a 2-fold effect on ATP binding both at 10 mM (data not shown) and 50 mM Mg^{2+} (**Table 3.2**). Additional functional and structural studies are required.

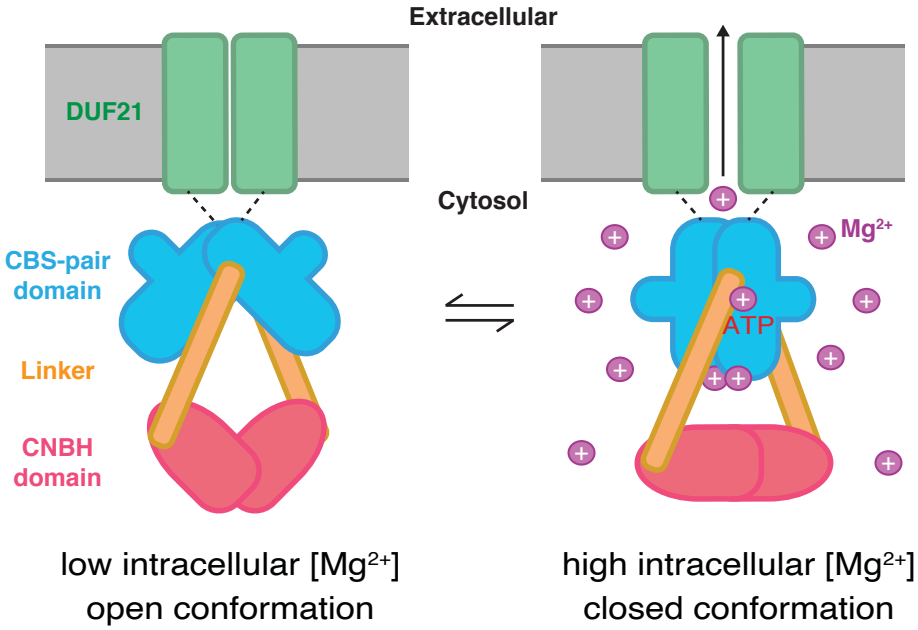

Figure 3.16 Proposed model for regulation of CNNM activity by Mg^{2+}

In low intracellular Mg^{2+} concentrations, the CBS-pair domain is in open conformation and CNBH domain is in V conformation. In high intracellular Mg^{2+} concentrations, the CBS-pair domain is in closed conformation with Mg^{2+}-ATP bound and CNBH domain is in a flat-conformation. These conformational changes affect the DUF21 domain and regulate Mg^{2+} transport.

Our structures provide additional insights into disease-associated mutations in the CNNM CBS-pair domains. T568I in CNNM2 and its equivalent in CNNM4 (T495I) are respectively associated with dominant hypomagnesemia and Jalili syndrome [19, 55]. CNNM4 R407L and P409L are found in Jalili syndrome patients [50, 53]. These mutations all lie within the Mg^{2+}-ATP-binding site (**Fig. 3.3F**) and all three completely abolish ATP binding (**Table 3.2**). T568I and R407L completely abolished Mg^{2+} efflux activity (**Fig. 3.6B**). The effect of P409L mutant could not be investigated due to lack of expression (**Fig. 3.10B**). Additionally, we showed that all three mutants were unable to form dimers in presence of Mg^{2+}-ATP (**Fig. 3.11D**). As previously suggested for the T568I mutation [91], these results confirm the essential role of the CNNM CBS-pair domains in Mg^{2+}-ATP sensing.

The CNBH domain of CNNM proteins are most similar to the domain in the potassium channel MloK1 [131]. Surprisingly, while the MloK1 CNBH domains were observed to crystallize in a variety of dimeric forms [100], they are not dimers in the intact protein [146]. A significant difference is that the CNNM CNBH domains do not bind cyclic nucleotides [131], which makes their physiological function less clear. *In vitro*, the CNNM CNBH domains promote CBS-pair domain dimerization and increase the affinity of Mg^{2+}-ATP binding (**Fig. 3.13E**), perhaps through restraining the linker between the two domains allowing its acidic residues to participate in Mg^{2+}-ATP binding (**Fig. 3.3F** and **Table 3.2**). However, functional studies paint a more nuanced picture. The CNNM4 mutations M629K and F631K both prevent CNBH dimerization but only F631K impairs efflux [131]. Similarly, mutations at the V-shaped CNBH dimerization interface have mixed effects on Mg^{2+} efflux (**Fig. 3.13D**). Therefore, understanding the role of the CNBH domain in CNNM function will require a structure of the intact protein.

3.5 Experimental Procedures

3.5.1 Cloning of CNNM cytosolic fragments and CBS-pair domains

All DNA sequences were codon-optimized for *E. coli* (Bio Basic Inc., Markham, Canada). Human CNNM2 cytosolic fragment (residues 429-817 Δ724-767) was sub-cloned into NdeI and XhoI sites of pET29a vector (Millipore Sigma) with a C-terminal His6-tag. Human CNNM3 cytosolic fragment (residues 299-658) was sub-cloned into BamHI and NotI sites of pGEX-6P-1 vector (GE Healthcare) with an N-terminal GST-tag. Human CNNM4 cytosolic fragment (residues 356-726 Δ649-670) was sub-cloned into BamHI and NotI sites of pSMT3 vector [147] with an N-terminal His6-SUMO-tag. CBS-pair domains of human CNNM1 (residues 412-568), CNNM2 (residues 429-584), CNNM3 (residues 299-452), CNNM4 ($CNNM4_{CBS}$; residues 356-511) and CNNM4 ($CNNM4_{CBS+linker}$; residues 356-546) were sub-cloned into BamHI and NotI sites of pSMT3 vector [147] with an N-terminal His6-SUMO-tag. $CNNM4_{CBS+linker}$-GST construct was made by sub-cloning human CNNM4 (residues 356-546) and GST (residues 1-218) into BamHI and XhoI sites of pSMT3 vector [147] with an N-terminal His6-SUMO-tag. Human $CNNM4_{CNBH}$ construct (residues 513-728) was described previously [131]. Human PRL2 construct (C95A, C96A, C119A, ΔCCVQ) was described previously [96]. Mutagenesis was performed using the QuikChange Lightning Site-Directed Mutagenesis Kit (Agilent).

3.5.2 Expression and purification of recombinant proteins

All constructs were verified by DNA sequencing and transformed into *Escherichia coli* strain BL21 (DE3). Cytosolic fragments were expressed at 37°C in Luria Broth (LB) to an optical density of 0.6 and induced with 1 mM IPTG overnight at 18°C, while CBS-pair domains were induced with 1 mM IPTG for 4 hours at 30°C. Cell pellet was obtained by centrifuging at 5000 g for 20 min. The pellet was re-suspended in buffer A (50 mM HEPES, 500 mM NaCl, 5% glycerol, 5 mM BME, pH 7.5) and lysed by sonication. Cellular debris was removed by centrifugation at 44,000 g for 45 min at 4°C. For GST constructs, the supernatant was loaded onto Glutathione Sepharose resin (GE Healthcare), washed with buffer A and eluted with buffer A containing 20 mM glutathione. The GST-tag was removed by overnight incubation with PreScission Protease, leaving an N-terminal Gly-Pro-Leu-Gly-Ser extension. For His-tag constructs, the supernatant was loaded onto Qiagen Ni-NTA resin, washed with buffer A

containing 30 mM imidazole and eluted with buffer A containing 500 mM imidazole. For SUMO-containing constructs, the SUMO-tag was removed by overnight incubation with His-Ulp, leaving an N-terminal Ser extension. The affinity-purified protein was applied onto an anion exchange column (BioSuite Q 13 μm AXC) equilibrated with buffer B (50 mM HEPES, 10 mM NaCl, 1 mM EDTA, pH 7.5) and eluted using a linear gradient of buffer C (50 mM HEPES, 1 M NaCl, 1 mM EDTA, pH 7.5). The protein was further purified by Superdex-200 (cytosolic fragments) or -75 (CBS-pair domains) size-exclusion column (GE Healthcare) in HPLC buffer (20 mM HEPES, 100 mM NaCl, 3 mM TCEP, pH 7.5). The final purified protein was concentrated to around 10 mg/mL (measured by NanoDrop), and the purity verified by SDS-PAGE.

3.5.3 Crystallization

Crystals of the CNNM3 cytosolic fragment were obtained by equilibrating 1 μL of protein (10 mg/mL) with 1 μL of reservoir solution (0.1 M Tris, pH 8.5; 0.5 M succinic acid, pH 7.0) in hanging-drop vapor diffusion system incubated at 22°C. Crystals of CNNM2 cytosolic fragment co-crystallized with 5 mM adenosine 5'-(β,γ-imido)triphosphate (AMP-PNP) were obtained by equilibrating 0.5 μL of protein (16 mg/mL) with 0.5 μL of reservoir solution (0.1 M Bis-Tris, pH 6.5; 0.5 M magnesium formate) in sitting-drop vapor diffusion system incubated at 22°C.

3.5.4 Data collection, structure determination and refinement

The crystals were cryoprotected by soaking in mother liquor supplemented with 25% ethylene glycol, picked up in a nylon loop and flash-cooled in a N_2 cold stream.

The CNNM3 cytosolic fragment dataset from a single crystal was collected at beam-line A1 of Cornell High-Energy Synchrotron Source (CHESS) using an ADSC Quantum-210 CCD detector (Area Detector Systems Corp.). The CNNM2 cytosolic fragment dataset from a single crystal was collected on beam-line 08ID-1 with a Pilatus3 S 6M detector at the Canadian Macromolecular Crystallography Facility (CMCF) of the Canadian Light Source (CLS). Data processing and scaling were performed with HKL-2000 [115] with auto-corrections enabled. Resolution cut-off is based on $CC_{1/2} = 0.3$ [148]. Initial phases of CNNM3 and CNNM2 cytosolic fragments were obtained by molecular replacement with Phaser [121] in PHENIX

[116] using previously determined structures of CNNM3 CBS-pair & CNBH domains (PDB: 5K23 [96] & 6DFD [131]) and CNNM2 CBS-pair & CNBH domains (PDB: 4P1O [91] & 6DJ3 [131]) as search models, respectively. The models were subsequently improved through iterative cycles of manual building with Coot [118] and refinement with phenix.refine [122]. TLS parameters were included at later stages of refinement [120]. The final structures were validated with MolProbity [149]. Crystallographic data collection and structure refinement statistics are shown in **Table 3.1**. Structural images were prepared with PyMOL, Version 2.0 (Schrödinger LLC, New York).

3.5.5 Analytical ultracentrifugation

Sedimentation velocity AUC experiments were performed at 20°C using a Beckman Coulter XL-I analytical ultracentrifuge using an An-60Ti rotor at 98,000 g (35,000 rpm) for 18 hours with scans performed every 60 seconds. A double-sector cell, equipped with a 12 mm Epon centerpiece and sapphire windows, was loaded with 380 and 400 µL of sample (100 µM) and HPLC buffer, respectively. Cytosolic fragments were monitored with UV at 280 nm, and the CBS-pair domains were monitored using interference optics. The data were analyzed with Sedfit v1501b [126] using a continuous c(s) distribution. Numerical values for the solvent density, viscosity, and the partial specific volume were determined using Sednterp [127]. Buffer density and viscosity were calculated to be 1.0039 g/cm^3 and 0.01026 mPa·s, respectively (20 mM HEPES, 100 mM NaCl, 3 mM TCEP, pH 7.5). Partial specific volumes for cytosolic fragments of CNNM2-4, CBS-pair domains of CNNM1-4 and CBS4·PRL2 complex were calculated to be 0.747247, 0.740825, 0.732722, 0.743489, 0.744818, 0.739639, 0.741420, and 0.739071 cm^3/g, respectively. Frictional ratio (f/f_0) values of CNNM CBS-pair domains alone and in complex with PRL2 were calculated using US-SOMO [128] to be 1.25 and 1.33, respectively. Default values were used for cytosolic fragments. Residual and c(s) distribution graphs were plotted using GUSSI [129].

3.5.6 Isothermal titration calorimetry

ITC experiments were performed on a MicroCal VP-ITC titration calorimeter (Malvern Instruments Ltd) at 20°C with stirring at 310 rpm. Protein (30 µM final concentration) and ligands were prepared in HPLC buffer containing 50 mM $MgCl_2$. The ligands were injected 15

times (5 μL for the first injection, 20 μL for subsequent injections), with 4 min intervals between injections. Results were analyzed using ORIGIN software (MicroCal) and fitted to a binding model with a single set of identical sites to estimate relative apparent affinities. The titration in **Fig. 3.15** with 50 mM Mg^{2+} was performed with 29 injections (5 μL for first injection, 10 μL for others) with 10 min intervals between the injections. Simulations of isothermal calorimetry profiles using a U-R2L2 model were performed with LineShapeKin Simulation ver. 4.1.8 [138]. For further discussion of the three-state ITC profiles, see [139].

3.5.7 ATP hydrolysis assay

The ATP hydrolysis assay was performed using Malachite Green Phosphatase Assay Kit (Sigma-Aldrich Inc). The assays were performed in a 100 μl final reaction volume consisting of 1 μM cytosolic fragments of CNNM2-4 or 0.03 μM (0.1 unit) of apyrase protein (SIGMA A6535) in HPLC buffer with 20 mM $MgCl_2$ and 1 mM ATP. The reaction was performed at RT for 30 min. Afterwards, the reaction mixture was diluted and mixed with 5X Working Reagent on a 96-well plate. After incubation for 30 min at RT, absorbance at 620 nm is recorded on SpectraMax Paradigm (Molecular Devices). The standard curve for inorganic phosphate was established with phosphate standard provided by the kit. All samples and standards were performed in triplicates.

3.5.8 Constructs used in mammalian culture cells

Human CNNM4 inserted into mammalian expression vector (pCMV-Tag 4A) was generated in the previous study [20]. All the mutants were generated using the QuikChange Lightning site-directed mutagenesis kit (Agilent).

3.5.9 Mg^{2+} efflux assays

Mg^{2+}-imaging analyses with Magnesium Green were performed as described in the previous study [20, 96]. Transfected HEK293T cells were incubated under growth media supplemented with 40 mM Mg^{2+} until use, to avoid potential decrease of intracellular Mg^{2+} levels by the expressed proteins. Then the cells were incubated with Mg^{2+}-loading buffer (78.1 mM NaCl, 5.4 mM KCl, 1.8 mM $CaCl_2$, 40 mM $MgCl_2$, 5.5 mM glucose, 5.5 mM HEPES-KOH, pH 7.4), including 2 μM Magnesium Green-AM (Invitrogen), for 30 min at 37°C. The

cells were rinsed once with loading buffer and viewed using ZEISS Axiovert 200M microscope equipped with ZEISS Axiocam 506 mono camera and X-Cite 120 LED light source. Fluorescence was measured every 20 s (excitation at 470–490 nm and emission at 505–545 nm) under the control of the ZEN software (ZEISS). Then the buffer was changed to remove Mg^{2+} buffer ($MgCl_2$ in the loading buffer was replaced with 60 mM NaCl). The data are presented as line plots of the mean fluorescence of 10 cells. After imaging analyses, cells were fixed with PBS containing 3.7% formaldehyde and subjected to immunofluorescence microscopy to confirm protein expression.

3.5.10 Immunofluorescence microscopy

Cells cultured on coverslips were stained and observed according to the previous study [20]. Cells were fixed with 3.7% formaldehyde in PBS for 20 min and permeabilized with 0.2% Triton X-100 in PBS for 5 min. After blocking with PBS containing 3% fetal bovine serum and 10% BSA (blocking buffer) for 1 h, cells were incubated for 1 h with rabbit anti-FLAG antibody (Sigma F7425) diluted in blocking buffer. Cells were washed three times with PBS and incubated for 30 min with Alexa 488–conjugated anti-rabbit IgG (Invitrogen A-11034) and rhodamine-phalloidin (for F-actin visualization, Invitrogen R415) diluted in blocking buffer. After three washes with PBS, coverslips were mounted on slides and observed with a confocal laser scanning microscope (ZEISS LSM 710).

3.5.11 Western blotting

Transfected HEK293T cells were harvested and lysed with lysis buffer (0.5% Triton X-100, 20 mM Tris pH 7.5, 150 mM NaCl, 2 mM EDTA). The lysates were centrifuged at 16,000 g. Equal amounts of total protein were loaded onto 8% SDS-PAGE. After electrophoresis, transfer and blot, membranes were probed with mouse anti-FLAG (SIGMA F1804) at 1:5,000 or rabbit anti-GAPDH (BioLegend 631401) at 1:1,000 for CNNM4-FLAG and GAPDH, respectively. This is followed by probing with peroxidase-conjugated goat anti-mouse IgG (Jackson ImmunoResearch 115-035-062) at 1:10,000 or peroxidase-conjugated goat anti-rabbit IgG (Jackson ImmunoResearch 111-035-144) at 1:10,000. The membranes were treated with ECL Prime (GE Healthcare RPN2232) and imaged using Bio-Rad ChemiDoc Imaging System.

3.6 Acknowledgements

We thank Véronique Sauvé and Jean-François Trempe for assistance with crystallographic data collection; Alexei Gorelik for advice on crystallographic data processing; Hiroaki Miki, Yosuke Funato, and Katalin Illes for assistance with Mg^{2+} efflux assays; Mehdi Amiri for the HEK293T cells; and Nelly Vuillemin and Erika Wee at the McGill University Advanced BioImaging Facility (ABIF) for microscope trainings. Crystallographic data were acquired at the Canadian Light Source (CLS) and at the Macromolecular Diffraction (MacCHESS) facility at the Cornell High-Energy Synchrotron Source (CHESS). CLS is supported by the Canada Foundation for Innovation, the Natural Sciences and Engineering Research Council (NSERC), the National Research Council, the Canadian Institutes of Health Research (CIHR), the Government of Saskatchewan, and the University of Saskatchewan. CHESS is supported by NSF award DMR-1332208, and the MacCHESS is supported by NIGMS award GM-103485. Y.S.C. is supported by a CIHR Doctoral Research Award (GSD-167011). This work was supported by NSERC grant RGPIN-2014-04686 to K.G.

Chapter 4 – Crystal structure of an archaeal CNNM magnesium transporter

Chen, Y. S., Kozlov, G., Armitano, J., Moeller, B. E., Fakih, R., Burke, J. E., Gehring, K. *Manuscript in preparation.*

4.0 Connecting Text

As shown from Chapter 3, nucleotide binding results in structural changes in the CBS-pair domain, and these changes are hypothesized to propagate to the neighboring transmembrane domain. Here, in Chapter 4, I perform structural and functional characterization of the CNNM transmembrane domain using an archaeal CNNM ortholog.

4.1 Summary

CBS-pair domain divalent metal cation transport mediators (CNNMs) represent an anciently conserved family of integral membrane proteins associated with Mg^{2+} transport. Here, we demonstrated direct Mg^{2+} transport of CNNM from *Methanoculleus thermophilus* (MtCNNM) and determined its crystal structure bound to Mg^{2+}-ATP. The structure reveals a novel transmembrane fold, representing the largest family of domains of unknown function, DUF21. The TMD exists in an inward-facing conformation with a highly acidic cavity and a conserved pi-helix that coordinates a Na^{+} ion. An acidic helical bundle between the transmembrane and cytosolic domains suggests involvement in Mg^{2+} sensing. Together, our results suggest MtCNNM is a Na^{+}/Mg^{2+} exchanger with a rocker-switch transport mechanism.

4.2 Introduction

Magnesium (Mg^{2+}), the most abundant divalent cation inside cells, is essential for a wide variety of biochemical processes, such as energy metabolism, maintenance of genomic stability, protein synthesis, and over 600 enzymatic reactions [2]. CNNMs (CBS-pair domain divalent cation transport mediators) represent a conserved family of integral membrane proteins implicated in Mg^{2+} homeostasis and divalent cation transport [130]. CNNMs are associated with a myriad of genetic diseases linked to abnormal Mg^{2+} handling. Mutations in *CNNM2* are found in dominant hypomagnesemia patients with symptoms such as cerebral seizures, mental retardation and brain malformations [19, 29]. Mutations in *CNNM4* are associated with Jalili syndrome, characterized by recessive amelogenesis imperfecta and cone-rod dystrophy [150]. CNNMs are also implicated in cancer through direct binding of oncogenic phosphatase of regenerating liver (PRL) [65, 66]. In addition, CNNMs have been associated with hypertension, infertility and schizophrenia [21, 77, 84, 85].

CNNM2 and CNNM4 are found abundantly in the basolateral membrane of kidney and colon epithelial cells, where renal/intestinal (re)absorption of Mg^{2+} occurs [19, 20]. Despite the clear association with Mg^{2+} transport, the field has not yet reached a consensus on the transport mechanism of CNNMs [31-33]. Some results support direct transport of Mg^{2+} through Na^{+}-coupled Mg^{2+} efflux [20] or direct Mg^{2+} influx [28, 66], while others support indirect transport through regulation of other Mg^{2+} channels (e.g. TRPM6/7) [29]. Since the transport assays were done through overexpression of CNNMs in cells, it is unclear whether CNNMs are themselves Mg^{2+} transporters or regulators of other Mg^{2+} transporters.

CNNMs are also known as ancient conserved domain proteins (ACDPs) because they contain a domain found in species ranging from bacteria, yeast, plants and animals (**Fig. 4.1A**) [14]. The conservation across evolutionarily divergent species suggests an ancient, conserved function. CNNM orthologs from various species demonstrate evidence of metal handling. MpfA, a CNNM ortholog in *Staphylococcus aureus*, is proposed to function as a Mg^{2+} exporter as ΔMpfA mutants are unable to grow in the presence of high concentrations of Mg^{2+} [39, 40]. Disruption of the gene in *Bacillus subtilis* leads to increased cellular Mg^{2+} content, again supporting a role in Mg^{2+} efflux [151]. Deletion of the yeast CNNM ortholog, Mam3, confers resistance to high levels of manganese, cobalt and zinc, possibly due to protection from elevated

cytosolic Mg^{2+} levels [36]. These reports strongly support the conservation of function in CNNM orthologs.

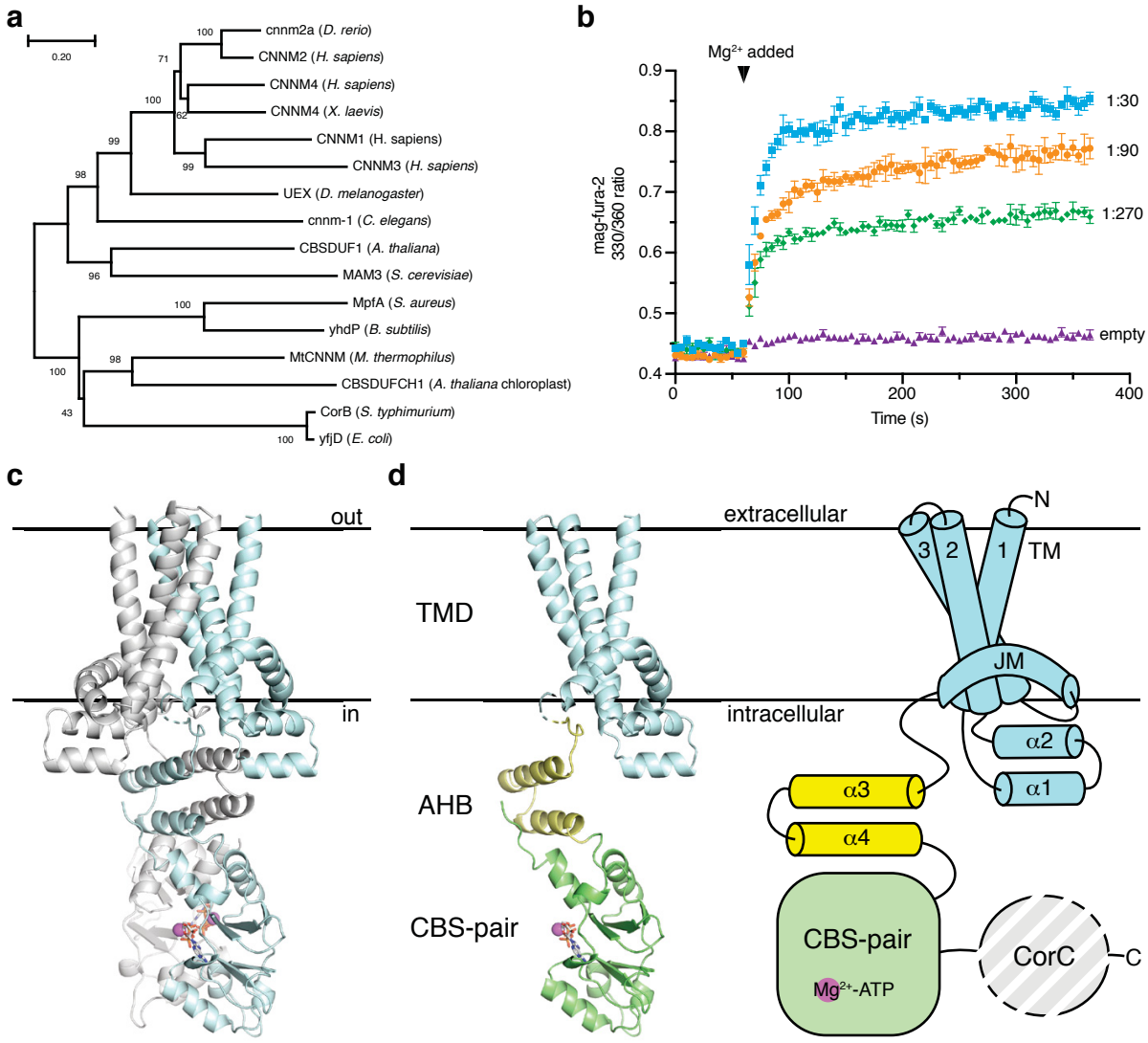

Figure 4.1 Crystal structure of MtCNNMΔ$C_{\Delta loop}$ bound to Mg^{2+}-ATP

(a) Phylogenetic analyses of representative CNNM orthologs generated using neighbor-joining method. The number beside the branches reflect the confidence level from bootstrapping of 1,000 replications. (b) Liposomal assay showing direct transport of Mg^{2+} by MtCNNM. MtCNNM-incorporated liposomes (1:30 to 1:270 wt/wt protein-to-lipid ratios) or empty liposomes containing mag-fura-2 were equilibrated in buffer for 1 min. Then 5 mM $MgCl_2$ was added (arrowhead) to initiate the Mg^{2+} uptake, and mag-fura-2 fluorescence at 330 and 360 nm were monitored overtime. The data points represent mean ± standard error of the mean of three

independent liposome preps. (c) Overall structure of a dimer of MtCNNMΔC$_{\Delta loop}$ bound to Mg^{2+}-ATP. Each chain is colored differently. (d) Topology of a MtCNNM monomer. Transmembrane domain (TMD; *cyan*) consists of three transmembrane (TM) helices, one juxtamembrane (JM) helix, and a helix-turn-helix motif between TM1 and TM2. This is followed by an acidic helical bundle (AHB; *yellow*) that makes a four-helix bundle in the dimer. This is followed by two soluble domains, CBS-pair (*green*) and CorC (*grey*) domain.

Structurally, CNNMs are defined by a conserved transmembrane and a cytosolic cystathionine-β-synthase (CBS)-pair domain. The transmembrane domain is called domain of unknown function 21 (DUF21), constituting the largest family of protein domains of unknown function (DUFs) on the Pfam database [90]. Prokaryotic CNNMs contain an additional C-terminal domain, called CorC_HlyC domain, also found at C-terminus of some Na^+/H^+ antiporters [152]. Currently, only the cytosolic domains have been characterized structurally. CBS-pair domain of human CNNMs acts as a Mg^{2+}-ATP sensing domain that undergoes large conformational changes upon Mg^{2+}-ATP binding [153]. These conformational changes are expected to be translated to the transmembrane DUF21 and affect transport. Despite being the largest family of DUF, consisting of close to 20,000 protein sequences from over 7000 species ranging from bacteria to plants and animals, the structure and function of DUF21 remain unknown.

Here, we determined the crystal structure of an archaeal CNNM in presence of Mg^{2+}-ATP, including the transmembrane DUF21. The structure reveals a highly acidic cavity and a Na^+ binding site. An acidic helical bundle connects TMD to CBS-pair domain and may be involved in Mg^{2+} sensing. We validated the functional importance of conserved residues using *in vitro* liposome assay and *in vivo* complementation assays. Our results suggest MtCNNM is a Na^+/Mg^{2+} antiporter with a rocker-switch transport mechanism.

4.3 Results

4.3.1 Functional characterization of MtCNNM

To identify CNNM orthologs with suitable properties for structural studies, we performed small-scale screening of 20 prokaryotic CNNMs from diverse species (**Fig. 4.2A**). Each construct was expressed as a GFP-fusion protein and purified in six different detergents (DDM, LMNG, OGNG, LDAO, C12E9, and OG). CNNM from *Methanoculleus thermophilus* (MtCNNM), a thermophilic archaeon, emerged as the most promising ortholog. MtCNNM is highly homologous to human CNNM2, sharing 29% identity and 48% similarity in the transmembrane and CBS-pair domains (**Fig. 4.3**). Size-exclusion chromatography analysis of MtCNNM showed a single mono-dispersed peak when purified with DDM, LMNG, and C12E9 (**Fig. 4.2B**), giving a pure protein sample as confirmed by SDS-PAGE (**Fig. 4.2C**).

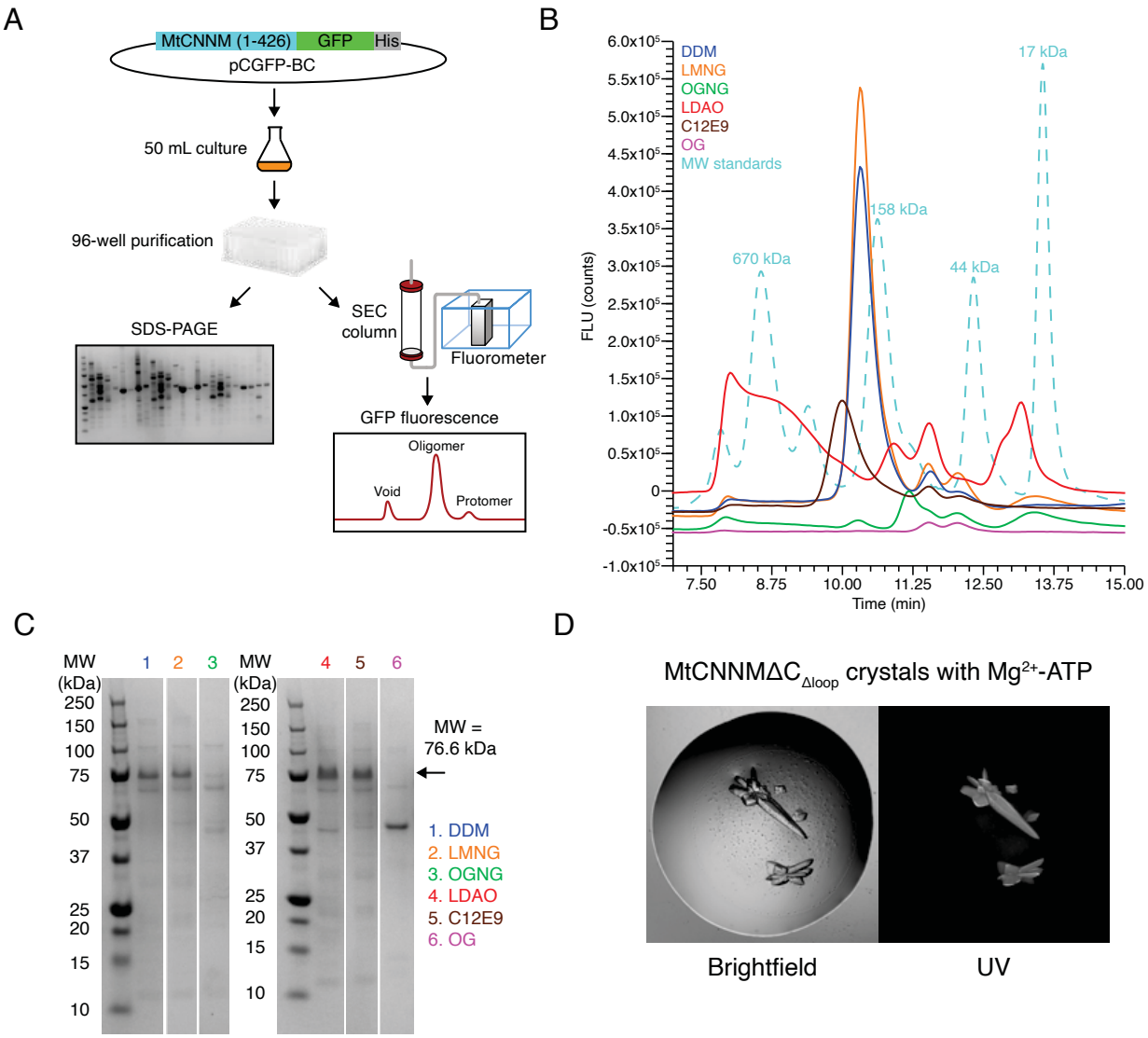

Figure 4.2 Detergent screening and crystallization of MtCNNM

(A) Schematic of high-throughput screening process. (B) Size-exclusion chromatography (SEC) profile of GFP-MtCNNM purified in different detergents. The dashed line shows molecular weight (MW) standards. (C) SDS-PAGE analysis of GFP-MtCNNM purified in 6 detergents. (D) MtCNNMΔC$_{\Delta loop}$ crystals in complex with Mg^{2+}-ATP taken with brightfield (*left*) and UV (*right*) camera.

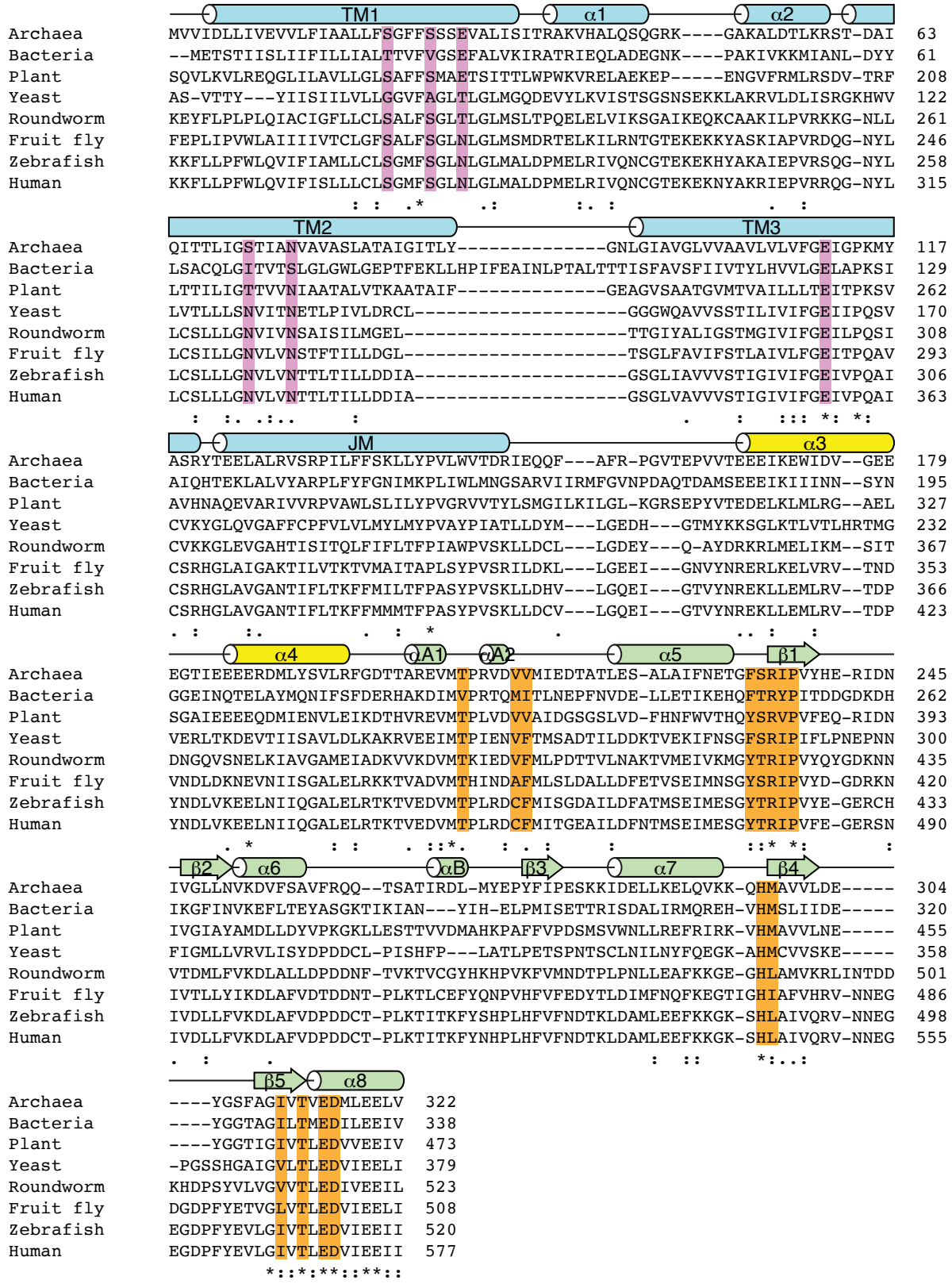

Figure 4.3 Sequence alignment of CNNM orthologs from eight representative species

The listed CNNM orthologs and their UniProt accession numbers are: *Methanoculleus thermophilus* (A0A1G8XA46), *Staphylococcus aureus* (A0A0H3JL60), *Arabidopsis thaliana* (Q84R21), *Saccharomyces cerevisiae* (Q12296), *Caenorhabditis elegans* (A3QM97), *Drosophila melanogaster* (A0A0B7P9G0), *Danio rerio* (A2ATX7), and *Homo sapiens* (Q9H8M5). Secondary structure corresponds to the crystal structure of *Mt*CNNMΔC$_{\Delta loop}$. Highlighted residues: polar residues in acidic cavity (*magenta*), ATP-binding site residues (*orange*).

We carried out functional characterization of MtCNNM reconstituted in liposome using ratiometric magnesium indicator, mag-fura-2 (**Fig. 4.1B**). We observed a time-dependent increase of fluorescence after the addition of Mg^{2+}, indicating transport of Mg^{2+} into proteoliposomes, whereas no fluorescence change was observed for liposome devoid of protein. These results demonstrate direct Mg^{2+} transport by MtCNNM, similar to the human CNNM proteins, suggesting conservation of function.

4.3.2 Structure determination

Attempt in crystallizing full-length MtCNNM yielded no suitable crystals. Therefore, several deletion mutants were generated. One of which has the C-terminal CorC domain deleted (MtCNNMΔC). MtCNNMΔC purified in DDM yielded diffracting crystals when crystallized with Mg^{2+}-ATP. It was processed to 2.2Å and solved by molecular replacement with CBS-pair domain from CorC (PDB: 5YZ2); however, the unit cell only contained the CBS-pair domain (**Table 4.1**).

Table 4.1 Statistics of data collection and refinement

Construct	MtCNNM (199-322)	MtCNNM (1-322) Δ259-262
Data collection		
X-ray source	ALS 5.0.2	CLS 08ID-1
Wavelength (Å)	1.00003	0.97996
Space group	$P4_122$	$P2_12_12_1$
Cell dimensions		
a, *b*, *c* (Å)	52.1, 52.1, 112.283	61.05, 118.676, 177.305
α, β, γ (°)	90.0, 90.0, 90.0	90.0, 90.0, 90.0
Resolution (Å)	50–2.20 (2.24–2.20)[1]	50–3.25 (3.31–3.25)[1]
Redundancy	21.5 (11.2)	11.9 (9.1)
Completeness (%)	99.0 (89.7)	99.2 (96.9)
$I/\sigma I$	40.6 (2.0)	22.0 (1.0)
$CC_{1/2}$	0.780	0.430
Refinement		
Resolution (Å)	35.00–2.20	49.31–3.25
No. of reflections	7746	14835
R_{work}/R_{free}	0.215/0.246	0.242/0.279
No. of atoms		
Protein	929	4786
Ligands	33	300
Water	51	NA
B-factors		
Protein	38.8	24.6
Ligands	26.5	41.3
Water	39.5	NA
RMSDs		
Bond lengths (Å)	0.002	0.002
Bond angles (°)	0.42	0.53
Ramachandran statistics (%)		
Most favored regions	97.5	96.4
Additional allowed regions	2.5	3.6
Disallowed regions	0.0	0.0

[1]Highest resolution shell is shown in parentheses

The in-situ cleavage suggests instability in DDM. Therefore, we tried purifying and crystallizing in other detergents, including maltosides with shorter alkyl chain. In addition, analysis of $MtCNNM_{CBS}$ structure showed missing density in a mobile loop from residue 260 to 261; thus, a new construct ($MtCNNM\Delta C_{\Delta loop}$) was generated. Together with detergent and construct modification, we were able to obtain diffracting crystals with UDM-purified $MtCNNM\Delta C_{\Delta loop}$ in complex with Mg^{2+}-ATP (**Fig. 4.2D**). The crystals diffracted anisotropically to 3.25 Å (**Table 4.1**). Initial phases were determined by molecular replacement using $MtCNNM_{CBS}$ structure solved earlier, which represented 40% of the crystallized construct (residues 199-322). Two α-helices (residues 166-198) preceding the CBS-pair domain were built in manually, then PHENIX AutoBuild [117] was used to place idealized helical fragments in the missing sections (residues 1-166). The resulting phases were of great quality that allowed tracing of most of the molecule, guided by strong densities of bulky residues (**Fig. 4.4A**). The final structure, consisting of chain A (residues 5-322) and chain B (residues 4-154 and 160-322), is refined to 3.25 Å with R-free of 0.279 (**Table 4.1**).

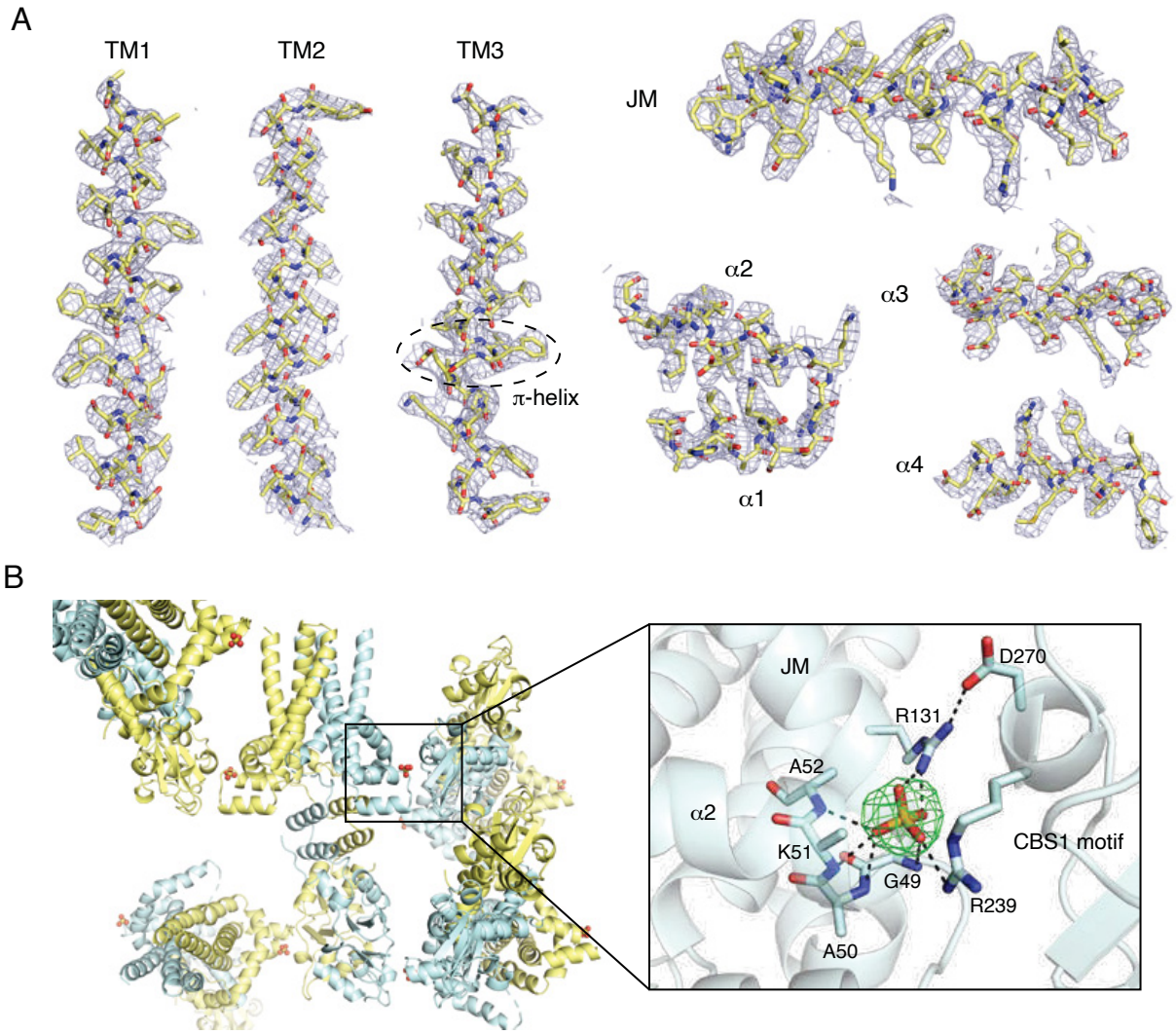

Figure 4.4 Representative electron density

(A) Representative $2F_o$-F_c map for TMD and AHB, contoured at 1.0 σ. (B) Representative F_o-F_c omit map for a sulfate ion between crystal packing surface, contoured at 5.0 σ.

4.3.3 Architecture and domain organization

MtCNNMΔC crystallizes as a homodimer with each protomer consisting of three distinct domains: transmembrane domain (TMD), acidic helical bundle (AHB), and CBS-pair domain (**Fig. 4.1C & D**). The TMD and AHB represent the previously unknown structural region with no homologous structures. Viewed from the membrane plane, MtCNNMΔC is approximately

110 Å tall with a 44 Å high transmembrane region and a 66 Å cytosolic region extending out of the membrane.

The TMD is made of three transmembrane helices (TM1-3) and one juxtamembrane helix (JM) (**Fig. 4.1D**). TM1, starting from the extracellular side, connects to TM2 through an intracellular helix-turn-helix motif (α1 & α2). Then, TM2 spans across the membrane and connects to TM3 through a short extracellular linker. TM3 traverses towards the cytosol and connects to the JM helix, which then wraps around the outer surface of TM1 and TM2, forming a belt-like structure. To our knowledge, TMD adopts a fold that is novel among available protein structures as querying the protein structure database for structural homologs with DALI server [101] returned only weak hits.

The TMD is followed by a helical bundle made of alpha helices α3 and α4, which we termed the acidic helical bundle (AHB) (**Fig. 4.1D**). AHB from each protomer dimerizes to form a four-helical bundle, connecting TMD to CBS-pair domain. The CBS-pair domain, as previously shown, dimerizes in a head-to-head fashion forming disc-like structure, accommodating Mg^{2+}-ATP in the central cavity [91, 153]. The C-terminal CorC domain, not present in the crystallized construct, is hypothesized to reside on either side of the CBS module based on existing structure of CorC (PDB: 4HG0), a soluble protein that resembles the intracellular region of MtCNNM.

Although MtCNNM exists as a homodimer, the two protomers do not share a C2 symmetry (**Fig. 4.5A**). The individual TMD and CBS-pair domains are symmetric on their own, but the arrangement of the two domains is not symmetric. By overlaying the TMD of each protomer, the cytosolic domains exist in two different conformations with respect to TMD (**Fig. 4.5B**). This suggests that the cytosolic domains have a certain degree of flexibility. Therefore, the current asymmetric arrangement most likely arises from crystal packing and has no physiological relevance.

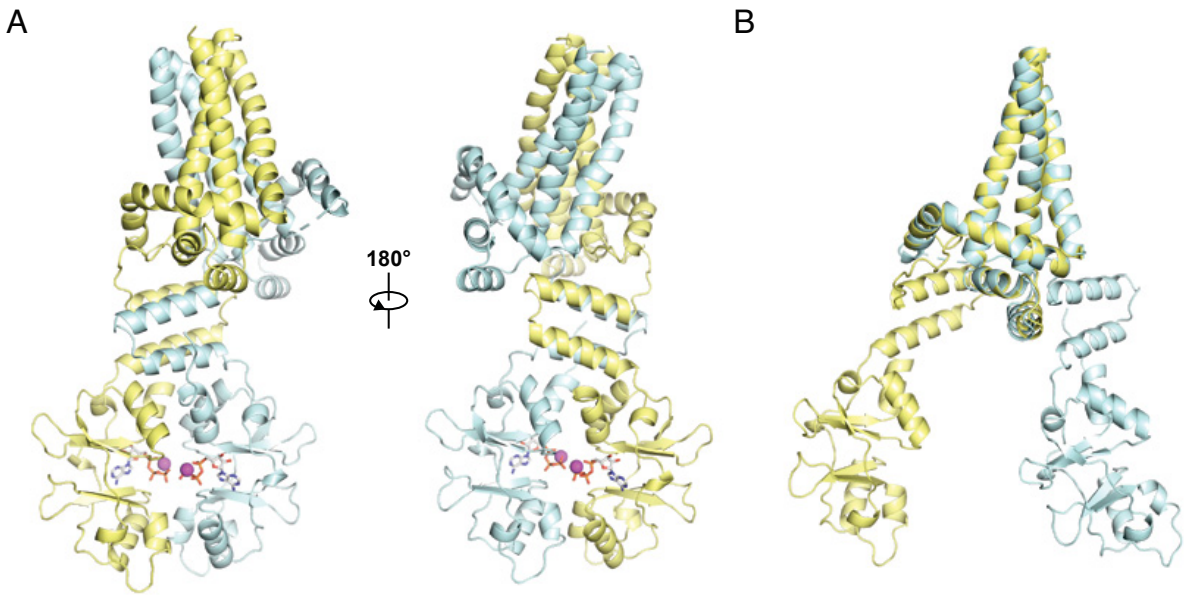

Figure 4.5 Asymmetry between the two polypeptide chains in the MtCNNMΔC structure. (A) Front and rear view of the MtCNNMΔC homodimer showing asymmetry between TMD and cytosolic domains. (B) Overlay of two protomers.

4.3.4 TMD in an inward-facing conformation with an acidic cavity and Na^+ binding site

The transmembrane domain exists as a homodimer in an inward-facing conformation. The dimerization interface is predominantly formed by hydrophobic contacts of TM2 and TM3 of each protomer (**Fig. 4.6A**). Electrostatic surface potential analysis reveals a highly negatively charged cavity with TM2 and TM3 interlacing around the central cavity (**Fig. 4.6B**). The central cavity, with a maximum diameter of approximately 10 Å, is lined with many polar residues (**Fig. 4.6C).** Sequence-conservation analysis revealed that residues forming the negatively charged pocket are highly conserved among CNNM orthologs (**Fig. 4.3**).

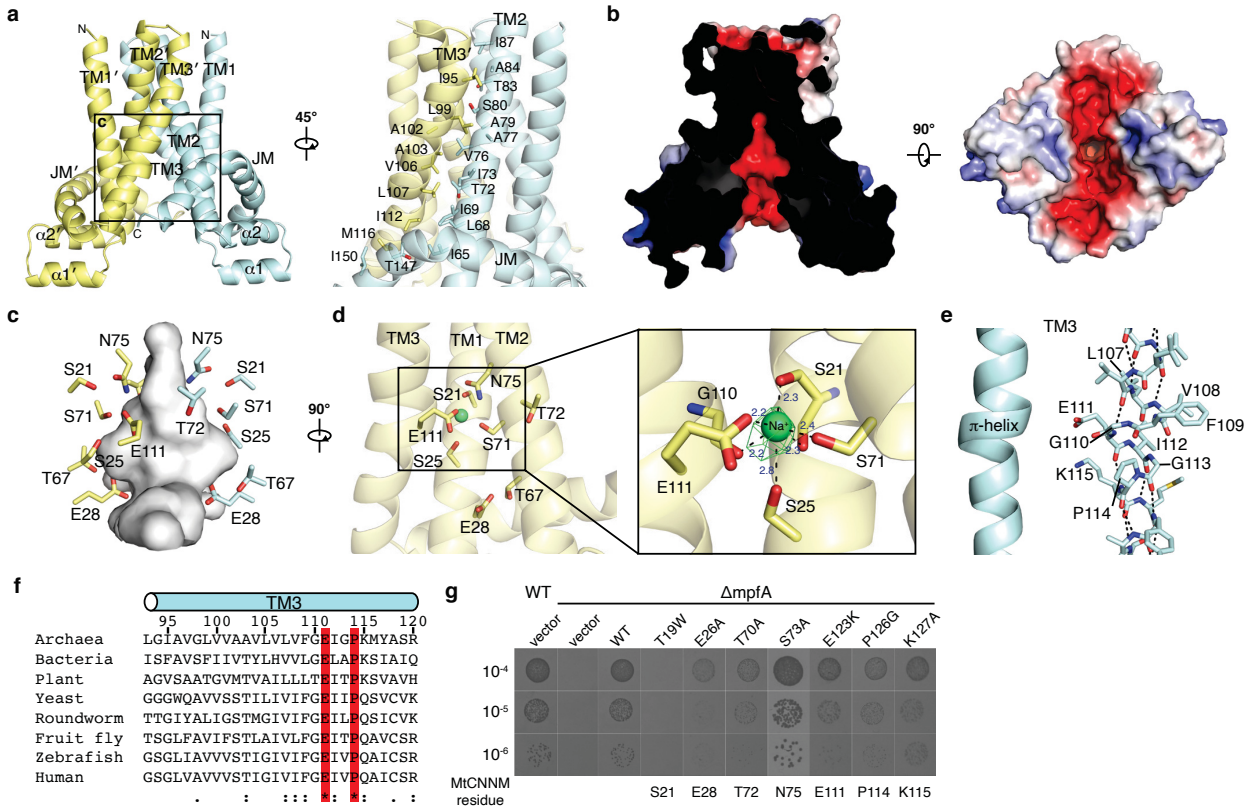

Figure 4.6 TM domain exists in an inward-facing conformation with a highly acidic cavity

(A) TM domain homodimerizes with interface formed by TM2 and TM3 of each protomer. (B) Electrostatic surface potential representation of MtCNNM TM domain shows a highly negative cavity, cross-sectional (*left*) and intracellular (*right*) views. (C) Close-up view of the residues forming the acidic cavity. (D) A sodium ion (Na^+) is bound at the negative cavity. The F_o-F_c omit map is contoured at 4.0 σ. (E) TM3 contains a π-helical turn resulted from a helix-breaker, Pro114. (F) The π-helix region is highly conserved in various CNNM orthologs. It is numbered according to MtCNNM. (G) Probing the effect of mutations in the acidic cavity of MpfA, a CNNM ortholog in *S. aureus*, by *in vivo* complementation of *S. aureus* ΔmpfA strain with indicated plasmids. Serially diluted overnight cultures were spotted on plates with 140 mM $MgCl_2$. Inactive mutants are unable to grow under high magnesium condition.

The central cavity is highly negatively charged, suggestive of a potential site for Na^+ and Mg^{2+} binding. Indeed, a well-defined electron density is observed in the cavity around residues Ser21, Ser25, Ser71, and Glu111. Analysis of crystallization condition suggests possibility of

Mg^{2+} or Na^{+}. Based on valance screening analysis and unlikelihood of binding of dehydrated Mg^{2+} [154], we placed a Na^{+} ion at this position (**Fig. 4.6D**). The Na^{+} is coordinated by hydroxyl groups of Ser21, Ser25, and Ser71; carboxyl group of Glu111; and the main-chain carbonyl groups of Ser21 and Gly110. Interestingly, this electron density is only observed in one of the protomer. Residues contributing to ion-side chain interactions are strongly conserved across species, suggesting a conserved binding mode for Na^{+}.

Another feature of the TMD is the presence of a π-helical turn in TM3, in which the helix is composed of i+5 instead of i+4 configuration, making a larger turn (**Fig. 4.6E**). This is supported by clear electron density during model building (**Fig. 4.4A**). Interestingly, the residues surrounding this helical turn are highly conserved from archaea to humans (**Fig. 4.6F**). Glu111 and Pro114 are invariant across the eight representative CNNM orthologs. Glu111 points toward the negative cavity and is involved in Na^{+} coordination, whereas Pro114 acts as a helix-breaker that allows the break in hydrogen-bonding.

In order to ascertain the importance of these cavity-lining residues, we used an *in vivo* complementation assay previously developed for MpfA, a CNNM ortholog in *Staphylococcus aureus* [39, 40]. Wild-type strain is able to grow under high Mg^{2+} conditions, while ΔMpfA strain cannot, and this can be rescued by complementation of vector expressing wild-type MpfA, whereas an empty vector cannot (**Fig. 4.6G**). Thus, the assay serves as a functional read-out of MpfA activity. Mutants T70A, S73A, E123K, P126G and K127A completely restored the growth defect; E26A partially restored; and T19W could not restore, illustrating the functional importance of Ser21 and Glu28 in MtCNNM.

4.3.5 A re-entrant juxtamembrane helix encircles TM helices

The re-entrant JM helix following TM3 wraps around TM1 and TM2 like a belt through several hydrophobic contacts. The JM helix resides close to the cytoplasmic membrane; thus, it may be involved in interacting with phospholipid headgroups. Indeed, we have observed several electron densities surrounding the JM helix, in which we modelled as UDM detergent molecules from the protein buffer (**Fig. 4.7A & B**). In total, we observed ten UDM molecules interacting with the two JM helices through several hydrophobic and aromatic residues, illustrating the potential binding mode with phospholipids.

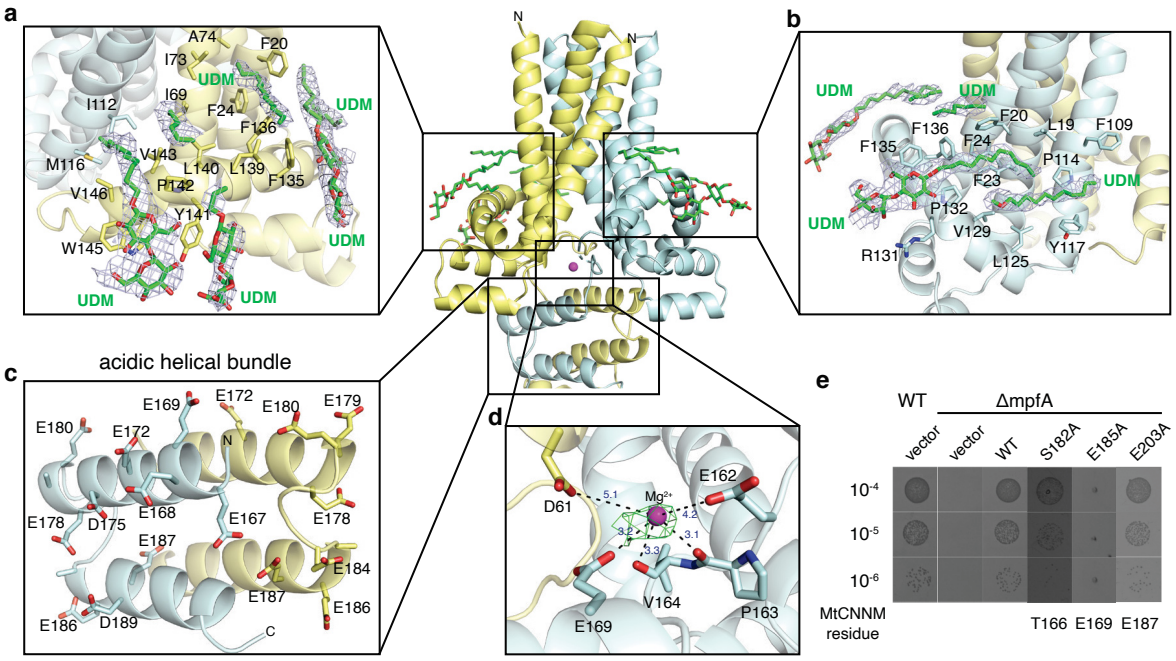

Figure 4.7 Juxtamembrane helix and acidic helical bundle

(A-B) Juxtamembrane helix binds many UDM detergent molecules. The $2F_o$-F_c map is contoured at 1.0 σ. (C) Acidic helical bundle contains many conserved acidic residues. (D) A hydrated magnesium ion binds between TMD and AHB. The F_o-F_c omit map is contoured at 3 σ. (E) Probing the effect of conserved acidic residue mutants in AHB by *in vivo* complementation of S. aureus ΔmpfA strain with indicated plasmids. Serially diluted overnight cultures were spotted on plates with 140 mM $MgCl_2$. Inactive mutants are unable to grow under high magnesium condition.

Underneath the JM helix resides the helix-turn-helix motif (α1 & α2) that connects TM1 and TM2. The two helices interact with JM helix through hydrophobic contacts. The solvent-exposed portions contain several basic residues, which may be involved in binding phospholipid headgroups. In fact, a strong density was observed in this region and was assigned as a sulfate molecule due to presence of Li_2SO_4 in crystallization condition (**Fig. 4.4B**). The sulfate ion seems to be involved in the crystal packing.

4.3.6 Acidic helical bundle

The acidic helical bundle between TM and CBS-pair domains is decorated with many acidic residues (13 out of 31 residues), which could serve as potential Mg^{2+} binding sites (**Fig. 4.7C**). Indeed, we found a density around Glu169, in which we modelled tentatively as a hydrated Mg^{2+} ion (**Fig. 4.7D**). The Mg^{2+} ion is anchored by carboxylate groups of three acidic residues (Asp61, Glu162, and Glu169) and by the backbone carbonyl atoms of Pro163 and Val164. The Mg^{2+}-O bond distances are between 3.1 Å and 5.1 Å, suggesting that the ion is in a hydrated state. Complementation assay of conserved acidic residues in the AHB showed the Glu169 is important whereas Thr166 and Glu187 are not (**Fig. 4.7E**).

4.3.7 Structural basis of Mg^{2+}-ATP binding by CBS-pair domain

We observed Mg^{2+}-ATP binding to the central cavity of CBS-pair domain as previously reported for human CNNMs (**Fig. 4.8A**) [91, 153]. The adenine is sandwiched between Phe233 and Ile311 in a hydrophobic pocket comprising Met298, Phe237, Ile236, Val212, and Val213, while the ribose ring forms hydrogen bonds with the side chains of Thr207, Asp316, and Thr313. The phosphate groups are stabilized with Arg235 and Ser234. The Mg^{2+} is coordinated in an octahedral arrangement by the three phosphates and three water molecules.

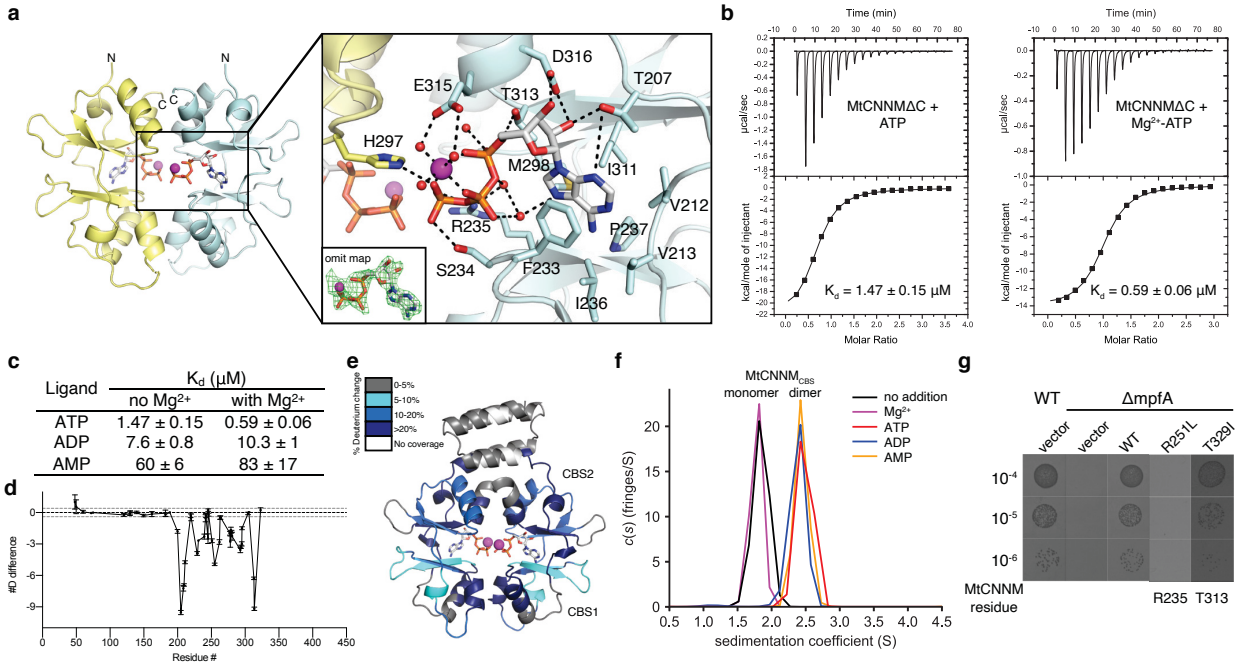

Figure 4.8 CBS-pair domain binds Mg^{2+}-ATP

(A) Structural basis of Mg^{2+}-ATP binding. Mg^{2+} ions and water molecules are shown as magenta and red spheres, respectively. F_o-F_c omit map contoured at 3.0 σ for Mg^{2+}-ATP. (B) ITC experiments of MtCNNMΔC (15 µM) binding to ATP (250 & 150 µM) in presence and absence of 50 mM Mg^{2+}. (C) Table summarizing affinities of MtCNNMΔC to adenine nucleotides with and without 50 mM Mg^{2+}. (D) The sum of the # of deuterons protected from exchange in the presence of Mg^{2+}-ATP across all timepoints is shown. Each point represents a single peptide, with them being graphed on the x-axis according to its central residue. Error bars represent standard deviation (n = 3). (E) HDX-MS analysis of MtCNNMΔC in presence and absence of Mg^{2+}-ATP. Regions in cytosolic regions that showed significant decreases in exchange (defined as >5%, 0.3 kDa, and a Student's t test $p<0.01$) in the presence of Mg^{2+}-ATP are colored in blue according to the legend. Peptides around the Mg^{2+}-ATP binding site show the most protection from deuterium exchange. (F) SV-AUC experiments of $MtCNNM_{CBS}$ with 1 mM adenine nucleotides or 10 mM Mg^{2+}. A dimeric species is observed in presence of adenine nucleotides. (G) Probing the effect of ATP-binding site mutants by *in vivo* complementation of S. aureus ΔmpfA strain with indicated plasmids. Serially diluted overnight cultures were spotted on plates with 140 mM $MgCl_2$. Inactive mutants are unable to grow under high magnesium condition.

We characterized the affinity of adenine nucleotides by isothermal titration calorimetry (ITC) with MtCNNMΔC. In absence of Mg^{2+}, the affinity for ATP is 1.47 μM while in presence of Mg^{2+}, the affinity is increased three-fold to 0.59 μM (**Fig. 4.8B**). MtCNNMΔC has the highest affinity for ATP, followed by ADP and AMP (**Fig. 4.8C** and **Fig. 4.9**). This is different from the human CNNMs, in which ATP binding is magnesium-dependent [41].

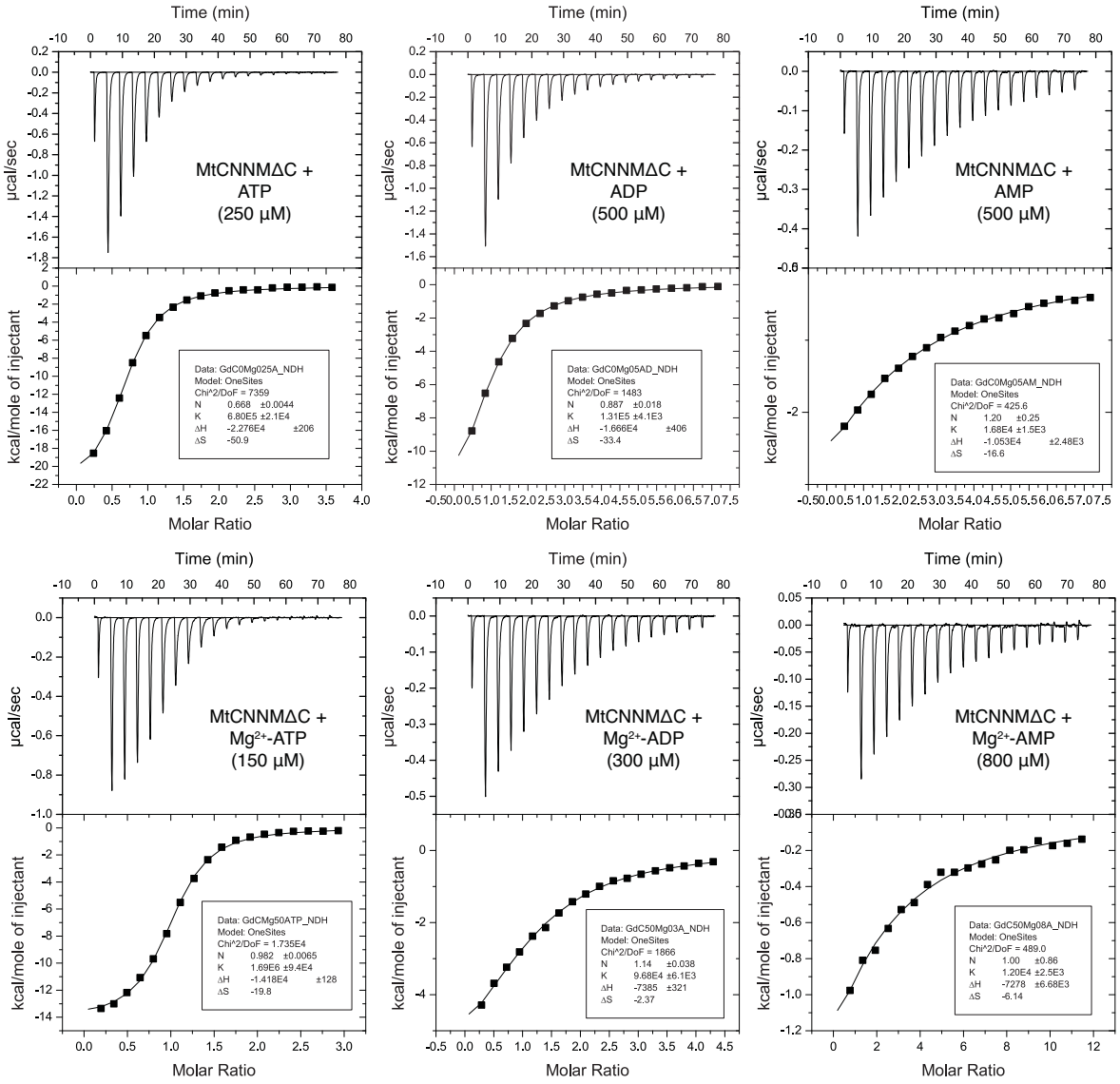

Figure 4.9 Raw ITC thermograms.

ITC thermograms showing MtCNNMΔC (15 μM) binding to various adenine nucleotides (concentrations indicated in parentheses) in absence or presence of 50 mM $MgCl_2$.

To characterize the structural effects of Mg^{2+}-ATP binding, we have reconstituted MtCNNMΔC into nanodiscs for analysis by hydrogen deuterium exchange mass spectrometry (HDX-MS) (**Fig. 4.10A**). Upon Mg^{2+}-ATP binding, we see an increased stabilization in the ATP binding site as well as the dimerization interface in CBS1 motif (**Fig. 4.8D & E**). However, no differences were observed for AHB and TMD, which has limited coverage (**Fig. 4.10B**). To validate the dimerization dependency of Mg^{2+}-ATP binding, we analyzed $MtCNNM_{CBS}$ by sedimentation velocity analytical ultracentrifugation (SV-AUC). Binding of adenine nucleotides trigger dimerization of CBS-pair domain while Mg^{2+} alone does not (**Fig. 4.8F** and **Fig. 4.11**). To probe the functional relevance of the ATP-binding site, we tested the effect of two disease-associated mutants in this region with the in vivo complementation assay. The results demonstrated the importance of Arg235 but Thr313 for rescuing the Mg^{2+}-dependent growth defect (**Fig. 4.8G**).

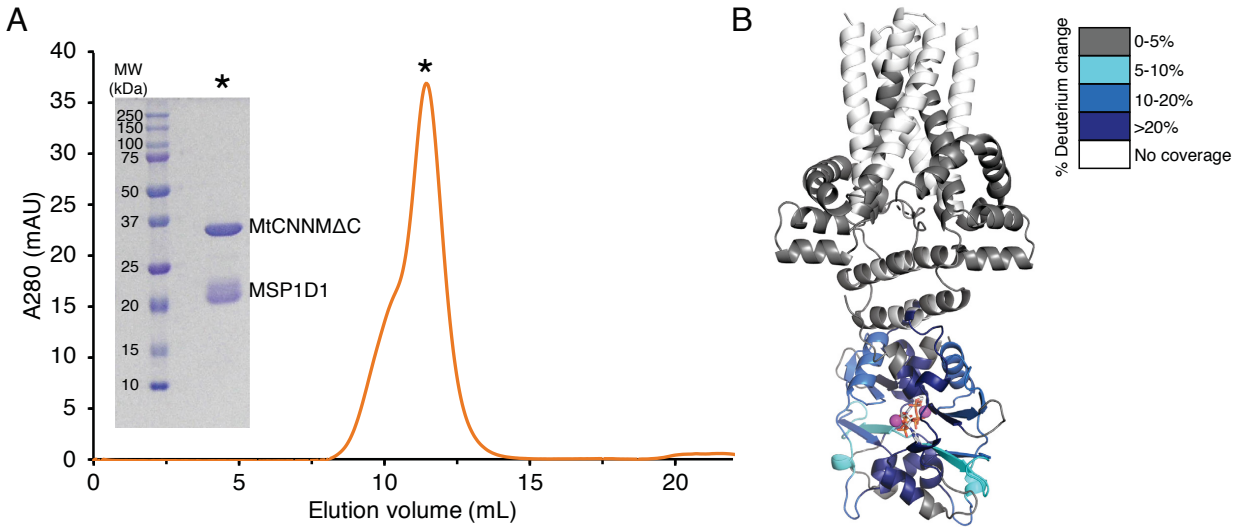

Figure 4.10 Reconstitution of MtCNNMΔC into MSP1D1 nanodiscs for HDX-MS analysis
(A) SEC profile and SDS-PAGE analysis of MtCNNMΔC reconstituted in MSP1D1 nanodiscs. (B) HDX-MS analysis of MtCNNMΔC in presence and absence of Mg^{2+}-ATP. Most differences occur in the CBS-pair domain. TMD shows limited coverage.

A

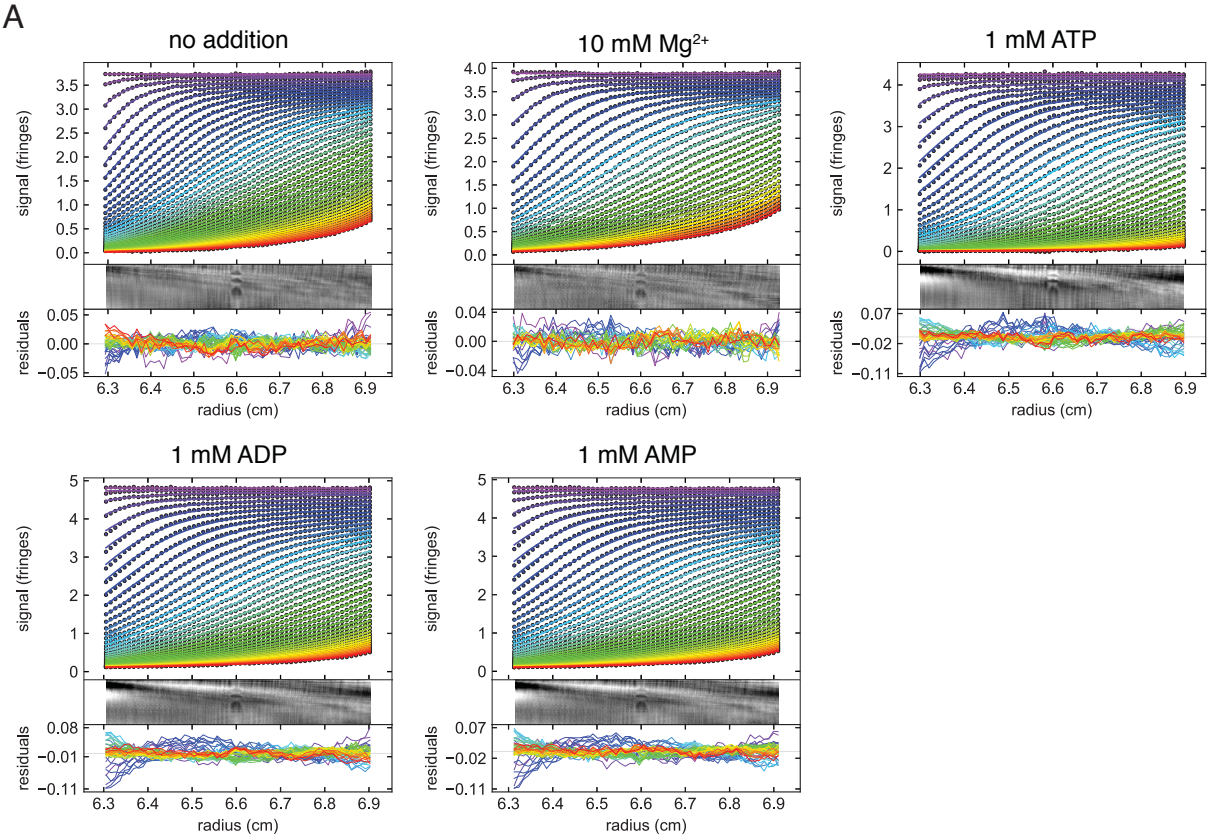

B

	Sedimentation coefficient (S)		Estimated MW (kDa)		RMSD	Theoretical MW (kDa)	
Condition	Peak 1	Peak 2	Peak 1	Peak 2		Monomer	Dimer
no addition	1.84	-	16.2		0.0049		
10 mM Mg^{2+}	1.78	-	16.0	-	0.0042		
1 mM ATP	-	2.49	-	32.0	0.0045	14.5	29.0
1 mM ADP	-	2.40	-	30.4	0.0044		
1 mM AMP	-	2.44	-	30.9	0.0050		

Figure 4.11 Summary of SV-AUC results

(A) Sedimentation velocity AUC profiles of $MtCNNM_{CBS}$ in presence of various ligands. Interference of the sample are plotted against the radial position in the cell. One in every 75 scans is plotted. (B) Summary of experimental sedimentation coefficients and estimated molecular weights.

4.4 Discussion

To date, MgtE and CorA represent the only two prokaryotic Mg^{2+} transport systems that have had their complete structures determined by X-ray crystallography [142, 155-157]. These advances have shed light on the structural basis of Mg^{2+} transport and homeostasis. Here, we determined the structure of a third Mg^{2+} transporter, CNNM.

The overall structure of MtCNNM is a dimer formed by three TM helices and one re-entrant JM helix, with a total of six TM helices (**Fig. 4.1C**). The low number of TM helices have previously been criticized as too little for a transporter when compared to other Mg^{2+} transporters such as CorA (10 TMs), MgtE (10 TMs), or TRPM6/7 (24 TMs) [32]. However, *in vitro* liposome assay using purified MtCNNM has demonstrated direct transport of Mg^{2+} (**Fig. 4.1B**). This affirms the notion that CNNM is a magnesium transporter on its own instead of regulator of other magnesium transporters.

The TMD exists in an inward-facing conformation without a continuous pore (**Fig. 4.6**), suggesting that CNNM could transport Mg^{2+} through a rocker-switch transport mechanism and the possibility of an outward-facing conformation. Since the TMD is connected to the CBS-pair domain through the AHB, perhaps conformational changes in the cytosolic domains caused by ATP-binding would propagate through AHB to the TMD, thereby affecting transport. The presence of many acidic residues on the AHB is reminiscent to CorA and MgtE, in which their cytosolic domains also contain acidic patches that are involved in Mg^{2+} sensing and regulation of channel activity [106]. Therefore, these acidic patches in AHB could also serve as potential Mg^{2+} binding sites that would play roles in Mg^{2+} sensing and transport regulation.

The highly negatively charged cavity strongly suggests binding of positively charged substrates (e.g. Mg^{2+} or Na^{+}). In this case, we observed a sodium ion bound in the negative cavity coordinated by conserved π-helix residues (**Fig. 4.6D**). It is unclear whether Mg^{2+} would compete for the same site or bind somewhere else in the cavity. A conserved glutamate residue (Glu28) is near the opening of the cavity; therefore, perhaps in another conformation, it could be involved in coordinating a hydrated Mg^{2+} ion.

The current structure lacks the C-terminal domain, which appears to be non-essential for the transport function. However, since this domain is the least conserved across species, the function of this domain may vary, especially in eukaryotic CNNMs that have a CNBH domain instead [131].

Taken together, we suggest a model for transport within CNNMs. During low or normal intracellular magnesium concentration, CNNM exists in an outward-facing conformation, in which the CBS-pair domain exhibits the open conformation and AHB exhibit a different conformation, constricting the JM helix. In the outward-facing state, high extracellular Na^+ concentration allows Na^+ binding to Na^+-binding site near π-helix. Upon elevation of intracellular magnesium level, Mg^{2+} ions bind to AHB and CBS-pair domain, stabilizing the flat, disc-like conformation, thus triggering the reorganization of the TMD into an inward-facing conformation, perhaps through relaxation of the constriction by JM helix. Upon exposure to the cytosol, Mg^{2+} ion will bind to the negatively charged cavity, and the Na^+ ions will diffuse away due to low intracellular Na^+ concentration. The departure of Na^+ ions will then destabilize the π-helix or TMD, thus favoring the outward-facing conformation, thereby transporting Mg^{2+} to the outside.

However, since we have only captured a snapshot of MtCNNM in the inward-facing conformation, further research is required to obtain snapshots of other states in order to fully understand the complete mechanism of transport by CNNMs.

4.5 Experimental Procedures

4.5.1 Construction of phylogenetic tree

Amino acid sequences of various CNNM orthologs were aligned using MUSCLE [15]. The phylogenetic tree was generated using neighbor-joining method and bootstrapping of 1,000 replications in MEGAX (Version 10.1.8) [16]. The CNNM orthologs and their UniProt accession numbers are: cnnm2a (*Danio rerio*; A2ATX7), CNNM2 (*Homo sapiens*; Q9H8M5), CNNM4 (*Homo sapiens*; Q6P4Q7), CNNM4 (*Xenopus tropicalis*; A0JPA0), CNNM1 (*Homo sapiens*; Q9NRU3), CNNM3 (*Homo sapiens*; Q8NE01), UEX (*Drosophila melanogaster*; A0A0B7P9G0), cnnm-1 (*Caenorhabditis elegans*; A3QM97), CBSDUF1 (*Arabidopsis thaliana*; Q67XQ0), MAM3 (*Saccharomyces cerevisiae*; Q12296), MpfA (*Staphylococcus aureus*; A0A0H3JL60), yhdP (*Bacillus subtilis*; O07585), MtCNNM (*Methanoculleus thermophilus*; A0A1G8XA46), CBSDUFCH1 (*Arabidopsis thaliana*; Q9LK65), CorB (*Salmonella typhimurium*; Q8XFY3), and yfjD (*Escherichia coli*; P37908),

4.5.2 Cloning of prokaryotic CNNMs

Codon-optimized cDNA of 20 prokaryotic CNNM orthologs were synthesized (Bio Basic Inc., Markham, Canada) and sub-cloned into NcoI and XhoI sites of pCGFP-BC vector [158] with a C-terminal GFP-His8-tag for small-scale expression and detergent screening. Promising orthologs were subcloned into NdeI and XhoI sites of pET29a vector (Millipore Sigma) with a C-terminal His6-tag for large-scale expression and crystallization experiments. Constructs for *Methanoculleus thermophilus* CNNM (UniProt entry A0A1G8XA46): MtCNNM (residues 1-426), MtCNNMΔC (residues 1-322), MtCNNMΔC$_{\Delta loop}$ (residues 1-322 Δ259-262). For MtCNNM$_{CBS}$, residues 199-322 were subcloned into BamHI and XhoI sites of pGEX-6P-1 vector (GE Healthcare) with an N-terminal GST-tag.

4.5.3 Small-scale expression and detergent screening of prokaryotic CNNMs

Prokaryotic CNNMs cloned in pCGFP-BC were transformed into *E. coli* strain C41 (DE3). Cells were grown in Luria Broth (LB) at 37°C to an optical density of 0.6 and induced with 1 mM IPTG for 4 hours at 30°C. Cell pellet was obtained by centrifuging at 5,000 g for 10 min. The pellet was re-suspended in lysis buffer (50 mM HEPES, 500 mM NaCl, 5% glycerol, pH 7.5) supplemented with cOmplete™ protease inhibitor cocktail (Roche) and split into 6

fractions. Lysis was performed using a 24-probe sonicator. Each fraction was solubilized with a different detergent (DDM; LMNG; OGNG; LDAO; C12E9; OG) to final concentration of 1%, then purified by IMAC in the same detergent (3x CMC). Elutions were analyzed by SDS-PAGE and size-exclusion chromatography on SEPAX Zenic-C SEC-300 connected to fluorescence detector (Ex 480 nm/ Em 510 nm) in buffer (50 mM HEPES pH 7.5, 150 mM NaCl, 0.5 mM TCEP, 3x CMC of detergent).

4.5.4 Expression and purification of MtCNNM and MtCNNMΔC

Constructs were transformed into *E. coli* strain C41 (DE3). Cells were grown in Luria Broth (LB) at 37°C to an optical density of 0.6 and induced with 0.5 mM IPTG overnight at 18°C. Cell pellet was obtained by centrifuging at 5,000 g for 20 min. The pellet was re-suspended in lysis buffer (50 mM HEPES, 500 mM NaCl, 5% glycerol, pH 7.5) supplemented with cOmplete™ protease inhibitor cocktail (Roche), 10 µg/mL DNAse I, 1 mM $CaCl_2$, 0.1 mg/mL lysozyme. Cells were lysed by passing through Avestin Emulsiflex-C3 homogenizer (10,000 – 15,000 p.s.i.). Cellular debris were removed by centrifugation at 27,000 g for 10 min at 4°C (this step is omitted for full-length MtCNNM). Membranes were pelleted by ultracentrifugation at 150,000 g for 1 hour at 4°C. The membrane fraction was collected, flash frozen in liquid nitrogen, and stored at -80°C for later use. The membrane fraction after thawing was solubilized in lysis buffer supplemented with 1% DDM for 1 hour at 4°C on a rotator, then ultracentrifuged at 150,000 g for 30 min at 4°C. The supernatant was loaded onto Qiagen Ni-NTA resin by batch binding, and incubated with gentle shaking for 1 hour at 4°C. The resin was then washed with wash buffer (50 mM HEPES, 500 mM NaCl, 5% glycerol, 30 mM imidazole, pH 7.5) containing 0.03% DDM or 0.05% UDM and eluted with elution buffer (50 mM HEPES, 500 mM NaCl, 5% glycerol, 300 mM imidazole, pH 7.5) containing 0.03% DDM or 0.05% UDM. The affinity-purified protein was further purified by size exclusion chromatography on a HiLoad 16/600 Superdex 200 pg column (GE Healthcare) in HPLC buffer (20 mM HEPES, 150 mM NaCl, pH 7.5) containing 0.03% DDM or 0.05% UDM. The final purified proteins were concentrated using 50 kDa (MtCNNMΔC) or 100 kDa (MtCNNM) cutoff concentrators (Amicon Ultra, Millipore), flash frozen in liquid nitrogen, and stored at -80°C for later use. The protein concentration is determined spectrophotometrically using Nanodrop, and purity is verified by SDS-PAGE.

4.5.5 Expression and purification of $MtCNNM_{CBS}$

Plasmid containing $MtCNNM_{CBS}$ was transformed into *E. coli* strain BL21 (DE3). Cells were grown in Luria Broth (LB) at 37°C to an optical density of 0.8 and induced with 1 mM IPTG overnight at 20°C. Cell pellet was obtained by centrifuging at 5,000 g for 20 min. The pellet was re-suspended in lysis buffer (50 mM HEPES, 500 mM NaCl, 5% glycerol, pH 7.5) supplemented with cOmplete™ protease inhibitor cocktail (Roche), 10 µg/mL DNAse I, 1 mM $CaCl_2$, 0.1 mg/mL lysozyme. Cells were lysed by sonication. Cellular debris were removed by centrifugation at 44,000 g for 45 min at 4°C. The supernatant was loaded onto Glutathione Sepharose resin (GE Healthcare), washed with lysis buffer and eluted with lysis buffer containing 20 mM glutathione. The GST-tag was removed by overnight incubation with PreScission Protease, leaving an N-terminal Gly-Pro-Leu-Gly-Ser extension. The protein was further purified by size exclusion chromatography on a HiLoad 16/600 Superdex 75 pg column (GE Healthcare) in HPLC buffer (20 mM HEPES, 100 mM NaCl, pH 7.5). The protein was diluted to a 5 µM, dialyzed overnight in dialysis buffer (20 mM HEPES, 100 mM NaCl, 5 mM EDTA, pH 7.5), and re-injected onto Superdex-75 to remove bound nucleotides. The final purified protein was concentrated to around 10 mg/mL (measured by NanoDrop), and the purity verified by SDS-PAGE.

4.5.6 Proteoliposome reconstitution and Mg^{2+} transport assay

Proteoliposome were made following [159] with modifications. A 3:1 mixture of 1-palmitoyl-2-oleoyl-*sn*-glycero-3-phosphoethanolamine (POPE) and 1-palmitoyl-2-oleoyl-*sn*-glycero-3-phospho-(1′-*rac*-glycerol) (POPG) (Avanti Polar Lipids) were dried into a thin film, followed by overnight incubation in a vacuum chamber. Dried lipids were solubilized to 5 mg/mL in buffer A (20 mM HEPES-NaOH, 150 mM NaCl, 5 mM EDTA-NaOH pH 7.5) supplemented with 35 mM CHAPS and incubated at room temperature for 2 hours. UDM-purified MtCNNM was mixed with 100 µL of solubilized lipids (0.5 mg) at a protein/lipid ratio of 1:30, 1:90, or 1:270 (wt:wt) and incubated for 20 min at room temperature. For the no-protein liposome control, the same volume of HPLC buffer containing 0.05% UDM was added. Proteoliposomes were formed by adding the protein/lipid sample to a partially dehydrated Sephadex G-50 column (1.5 mL) equilibrated in buffer A. Membrane impermeable ratiometric magnesium indicator, mag-fura-2 (Thermo Fisher; stock concentration 1 mM in H_2O) was added

to final concentration of 50 μM and encapsulated through 1 freeze-thaw cycle. Exchange of extra-liposomal buffer and dye removal were performed by centrifuging the proteoliposomes in a partially dehydrated Sephadex G-50 column equilibrated in buffer B (20 mM HEPES-NaOH, 150 mM NaCl, pH 7.5).

Fluorescence transport assay was performed with SpectraMax M5e using two excitation wavelengths (330 and 369 nm) and one emission wavelength (509 nm), measuring every 5 seconds including 1 second shaking between reads. 10 μL of mag-fura-2 encapsulated proteoliposome was diluted with 90 μL of Buffer B in a 96-well black bottom plate (Greiner) and baseline fluorescence was measured for 1 min at 25°C. The uptake reaction was initiated by addition of $MgCl_2$ and recorded for 5 min. CHAPS and EDTA were added to obtain the maximum and minimal mag-fura-2 signal. Each condition was performed with three independent proteoliposome preps.

4.5.7 Crystallization

Crystals of $MtCNNM_{CBS}$ co-crystallized with 5 mM ATP were obtained by equilibrating 0.4 μL of protein (20.8 mg/mL MtCNNMΔC purified in 0.03% DDM) and 0.4 μL of reservoir solution (0.1 M MOPS, pH 7.0; 9% PEG 8000; 20 mM $MgCl_2$) in sitting-drop vapor diffusion system incubated at 22°C. Rod-like crystals appeared after 2 weeks. The crystals were cryo-protected with reservoir solution supplemented with 5 mM ATP and 30% ethylene glycol, picked up in a nylon loop, and flash-cooled in a N_2 cold stream.

Crystals of $MtCNNM\Delta C_{\Delta loop}$ co-crystallized with 5 mM ATP were obtained by equilibrating 1 μL of protein (19.5 mg/mL $MtCNNM\Delta C_{\Delta loop}$ purified in 0.05% UDM) and 1 μL of reservoir solution (0.1 M Na citrate, pH 5.5; 0.1 M Li_2SO_4; 0.1 M NaCl; 20 mM $MgCl_2$; 34% PEG400; 10 mM Na_2HPO_4) in hanging-drop vapor diffusion system incubated at 22°C. Petal-like crystals appear after 1 week. The crystals were directly picked up in a nylon loop and flash-cooled in a N_2 cold stream.

4.5.8 Data collection and structure determination

The $MtCNNM_{CBS}$ dataset from a single crystal was collected using a Pilatus3 6M detector at beamline 5.0.2 of Advanced Light Source (ALS). Data processing and scaling were performed with HKL-2000 [115] with auto-corrections enabled. Initial phases were obtained by

molecular replacement with Phaser [121] in PHENIX [116] using CBS-pair domain structure of CorC (PDB: 5YZ2) [160]. The model was subsequently improved through iterative cycles of manual building with Coot [118] and refinement with phenix.refine [122]. TLS parameters were included at later stages of the refinement [120].

The MtCNNMΔC$_{\Delta loop}$ dataset from a single crystal was collected using a Pilatus3 6M detector at beamline 08ID-1 of the Canadian Macromolecular Crystallography Facility (CMCF) of the Canadian Light Source (CLS). The dataset showed anisotropic diffraction up to 3.25 Å. Data processing and scaling were performed with HKL-2000 [115] with auto-corrections enabled, in which ellipsoid truncation was performed automatically. Resolution cut-off is based on $CC_{1/2}$ = 0.3 [148]. Resolution limits after ellipsoid truncation were a*= 4.07 Å, b* = 3.71 Å and c* = 3.25 Å. Initial phases for the CBS-pair domain were obtained by molecular replacement with Phaser [121] in PHENIX [116] using MtCNNM$_{CBS}$ structure (determined in this study). Then AutoBuild [117]was used to build in the missing domains (TMD and AHB). The model was then improved through iterative cycles of manual building with Coot [118] and refinement with phenix.refine [122]. TLS parameters were included at later stages of the refinement [120].

The final structures were validated with MolProbity [149]. Crystallographic data collection and structure refinement statistics are shown in Table S1. Structural images were prepared with PyMOL, Version 2.3.4 (Schrödinger LLC, New York). Electrostatic surface potentials were calculated using the APBS plugin within PyMOL [161].

4.5.9 In vivo complementation assays of various MpfA mutants in *Staphylococcus aureus*

Various point mutants of mpfA were cloned on a multicopy plasmid (pCN47 based) under the control of a xylose inducible promoter [162, 163]. All mutated alleles were obtained by fusion PCR and cloned between restrictions sites SphI and AscI.

The functionality of the alleles was assessed by testing their ability to complement the magnesium sensitivity of an *Staphylococcus aureus* ΔmpfA strain (PR01-36) [39]. Overnight cultures of strains carrying various plasmids were serially diluted in Mueller Hinton (MH) media and 10 µL of each dilution were spotted onto MH plates containing media (MH 211443, BD Biosciences, Allschwil, Switzerland) supplemented with 10 mg/L uracil, 10 mg/L erythromycin, 13 g/L of agar and as necessary, varying concentrations of $MgCl_2$ and xylose. Plates were incubated for 20 hours at 37°C. Only relevant dilutions (10^{-4} to 10^{-6}) are shown in figures. All

experiments include three controls: WT strain (PR01) carrying an empty vector, ΔmpfA strain carrying an empty vector, and ΔmpfA strain carrying a vector containing mpfA G326C (an inactive allele).

4.5.10 Isothermal titration calorimetry

ITC experiments were performed on a MicroCal VP-ITC titration calorimeter (Malvern Instruments Ltd) at 20°C with stirring at 310 rpm. Protein (15 μM final concentration) and ligands were prepared in HPLC buffer containing 0.05% UDM with or without 50 mM $MgCl_2$. The ligands were injected 19 times (5 μL for the first injection, 15 μL for subsequent injections), with 4 min intervals between injections. Results were analyzed using ORIGIN software (MicroCal) and fitted to a binding model with a single set of identical sites.

4.5.11 Production and purification of MSP1D1

pMSP1D1 was a gift from S. Sligar (Addgene plasmid 20061). MSP1D1 production was carried out according to published protocols [164]. In brief, *E. coli* BL21 (DE3) cells transformed with pMSP1D1 were grown in LB at 37°C to an optical density of 0.8 and induced with 1 mM IPTG for 4 hours at 30°C. MSP1D1 was purified by nickel affinity chromatography according to standard conditions described in [164]. The polyhistidine tag was removed by overnight incubation with TEV protease and further purified by Superdex-75 size-exclusion column (GE Healthcare) in HPLC buffer (20 mM HEPES, 150 mM NaCl, pH 7.5)

4.5.12 Reconstitution into nanodisc

MtCNNMΔC and MSP1D1 were mixed with soybean polar extract (Avanti) solubilized in 40 mM DDM at a MtCNNMΔC:MSP1D1:lipid molar ratio of 2:10:550 in HPLC buffer. Detergent was removed by incubation with Bio-Beads (Bio-Rad SM-2 Resin) at 4°C overnight with constant rotation. Bio-beads were removed via filtration and the reconstitution mixture was re-loaded onto Qiagen Ni-NTA resin to remove empty nanodiscs. The resin was washed with wash buffer (20 mM HEPES, 200 mM NaCl, 20 mM imidazole, pH 7.5) and eluted with wash buffer with 300 mM imidazole. The eluted protein was further purified by size exclusion chromatography on a Superdex 200 Increase 10/300 GL column (GE Healthcare) in HPLC buffer (20 mM HEPES, 150 mM NaCl, pH 7.5).

4.5.13 Hydrogen deuterium exchange mass spectrometry

HDX-MS reactions were performed in a similar manner as described previously [165, 166]. In brief, HDX reactions for MtCNNMΔC were conducted in a final reaction volume of 10 µL with a molar quantity of 20 pmol of MtCNNMΔC. The reaction was started by the addition of 9.0 µL of D_2O buffer (100 mM NaCl, 20 mM HEPES pH 7.5, 94% D_2O (V/V)) to 1.0 µL of protein solution (final D_2O concentration of 84.9%). The reaction proceeded for 3, 30, 300, or 3000 s at 20°C, before being quenched with ice cold acidic quench buffer, resulting in a final concentration of 0.6 M guanidine-HCl and 0.9% formic acid post quench. All conditions and timepoints were created and run in triplicate. Samples were flash frozen immediately after quenching and stored at -80°C until injected onto the ultra-performance liquid chromatography (UPLC) system for proteolytic cleavage, peptide separation, and injection onto a QTOF for mass analysis, described below.

Protein samples were rapidly thawed and injected onto a UPLC system kept in a Peltier driven cold box at 2°C (LEAP). The protein was run over two immobilized pepsin columns (Trajan; ProDx Protease column PDX.PP01-F32) and the peptides were collected onto a VanGuard Precolumn trap (Waters). The trap was eluted in line with an ACQUITY 1.7 µm particle, 100 × 1 mm^2 C18 UPLC column (Waters), using a gradient of 5%-36% B (Buffer A 0.1% formic acid, Buffer B 100% acetonitrile) over 16 min. MS experiments were performed on an Impact HD QTOF (Bruker) and peptide identification was done by running tandem MS (MS/MS) experiments run in data-dependent acquisition mode. The resulting MS/MS datasets were analyzed using PEAKS7 (PEAKS) and a false discovery rate was set at 1% using a database of purified proteins and known contaminants. HDExaminer Software (Sierra Analytics) was used to automatically calculate the level of deuterium incorporation into each peptide. All peptides were manually inspected for correct charge state and presence of overlapping peptides. Deuteration levels were calculated using the centroid of the experimental isotope clusters. Differences in exchange in a peptide were considered significant if they met all three of the following criteria: > 5% change in exchange, > 0.4 Da mass difference in exchange, a p-value < 0.01 using a two-tailed Student's t-test, and change spanned by multiple peptides.

4.5.14 Analytical ultracentrifugation

Sedimentation velocity AUC experiments were performed at 20°C using a Beckman Coulter XL-I Optima analytical ultracentrifuge and an An-60Ti rotor at 98,000 g (35,000 rpm) for 18 hours with scans performed every 60 seconds. A double-sector cell, equipped with a 12 mm Epon centerpiece and sapphire windows, was loaded with 380 and 400 µL of sample and HPLC buffer. $MtCNNM_{CBS}$ (100 µM) with various ligands were monitored using interference optics. The data were analyzed with Sedfit v1501b [126] using a continuous c(s) distribution. Numerical values for the solvent density, viscosity, and partial specific volume were determined using Sednterp [127]. Buffer density and viscosity were calculated to be 1.0039 g/cm^3 and 0.01026 mPa·s, respectively (20 mM HEPES, 100 mM NaCl, pH 7.5). Partial specific volumes for $MtCNNM_{CBS}$ was calculated to be 0.7464 cm^3/g. The frictional ratio (f/f_0) value for $MtCNNM_{CBS}$ was calculated using US-SOMO [128] to be 1.26. Residual and c(s) distribution graphs were plotted using GUSSI [129].

4.6 Acknowledgements

We thank Katharina Duerr and her lab members for assistance with initial screening of prokaryotic CNNMs; Alexei Gorelik for advice on crystallographic data processing; Nazzareno D'Avanzo for assistance with liposome transport assay; Martin Schmeing and Camille Fortinez for crystallographic data collection at Advanced Light Source (ALS); Canadian Light Source (CLS) staff: Michel Fodje, Shaun Labiuk, Bulat Gabidullin, and Kathyrn Janzen. CLS is supported by the Canada Foundation for Innovation, the Natural Sciences and Engineering Research Council (NSERC), the National Research Council, the Canadian Institutes of Health Research (CIHR), the Government of Saskatchewan, and the University of Saskatchewan. Y.S.C. is supported by a CIHR Doctoral Research Award (GSD-167011). This work is supported by NSERC grant RGPIN-2020-07195 to K.G.

Chapter 5 – General Discussion

In this thesis, I have determined a total of six structures: two structures of CNBH domain, two structures of the cytosolic fragments, one structure of MtCNNM CBS-pair domain, and one structure of MtCNNM lacking CorC domain. Here, I present a structural comparison between CNNM and two other prokaryotic magnesium transporters with known structures.

5.1 Other Mg^{2+} transporters with known structures

Currently, there are two prokaryotic Mg^{2+} transporters that have their full-length structures determined: CorA and MgtE.

5.1.1 CorA

CorA represents one of two primary Mg^{2+} transport system in prokaryotes. It was named for the cobalt-resistant mutant in which it was first identified [167]. Its eukaryotic counterpart is a mitochondrial inner membrane protein, Mrs2, required for normal mitochondrial Mg^{2+} homeostasis and function [168]. Multiple full-length structures of CorA by X-ray crystallography or cryo-EM have been determined in presence or absence of Mg^{2+} from two species: *Thermotoga maritima* (TmCorA) and *Methanocaldococcus jhannachii* (MjCorA) [155-157, 169-172].

5.1.2 MgtE

MgtE represents the other primary Mg^{2+} transport system in prokaryotes. The human ortholog is represented by the SLC41 family of solute carriers [173]. Electrophysiological characterization by patch-clamp analysis established MgtE as a high conductance Mg^{2+}-selective Mg^{2+}-gated ion channel [141]. Multiple crystal structures have been determined for MgtE in the closed, Mg^{2+}-bound state [141, 142, 174, 175]. Recently, an open state of the channel stabilized by Fab antibodies has been elucidated by cryo-EM [176].

5.2 General architecture

CorA is represented as a funnel-shaped homopentamer with a large intracellular N-terminal domain linked through an extended α-helix to a C-terminal TM ion pore domain (**Fig. 5.1A**) [155-157]. The intracellular domain is a seven-stranded parallel/antiparallel β-sheet sandwiched between two sets of α-helices. The TM domain has a total of ten TM helices with two helices contributing from each protomer.

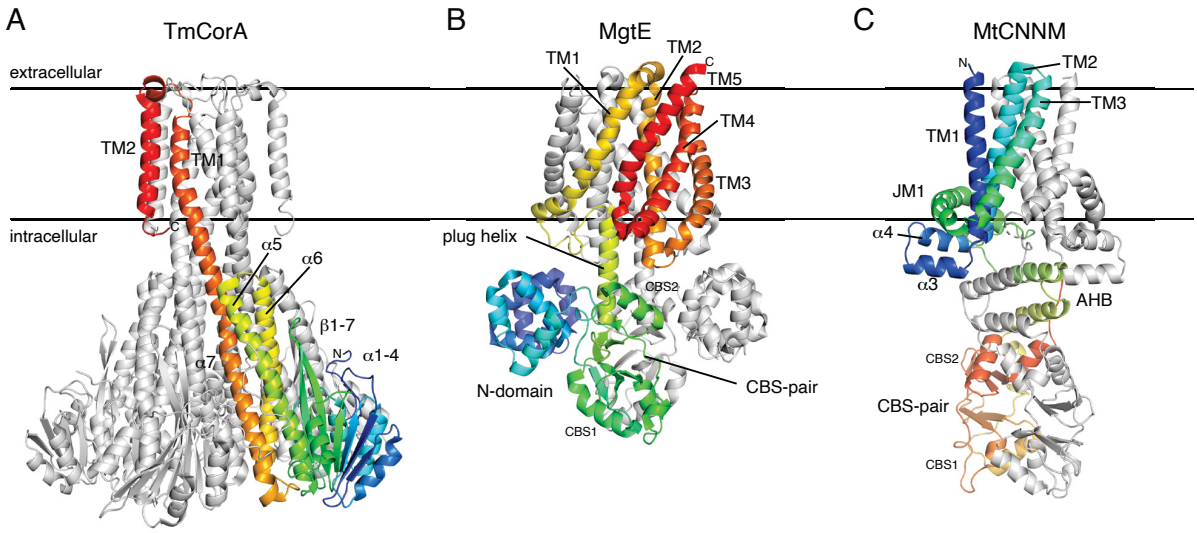

Figure 5.1 Structures of three prokaryotic Mg^{2+} transporters

(A) Overall structure of TmCorA in the Mg^{2+}-bound state (PDB: 4I0U [171]). (B) Overall structure of MgtE in Mg^{2+}-bound state (PDB: 2ZY9 [141]). (C) Overall structure of MtCNNM lacking CorC domain in Mg^{2+}-ATP-bound state. For each structure, a single chain is colored *blue* (N-terminus) to *red* (C-terminus).

MgtE is a dimer with two cytosolic domains (N-domain and CBS-pair domain) in the N-terminus (**Fig. 5.1B**) [142]. The CBS-pair domain dimerizes in a head-to-head fashion while the superhelical N-domain hangs on either side of the CBS module. This is then followed by an extended α-helix (plug helix) that leads to the C-terminal transmembrane domain. The TMD has a total of ten TM helices with each protomer contributing five helices. TM2-5 are arranged as a helical bundle while TM1 engages in a domain-swapped interaction with TM2′ and TM3′ from the other protomer.

MtCNNM is a homodimer with the TMD in the N-terminus, followed by CBS-pair and CorC domain (**Fig. 5.1C**). The TMD is made up of six TM helices with two juxtamembrane helices, with each protomer contributing three TM helices and one juxtamembrane helix. The TMD is connected to the CBS-pair domain through an acidic helical bundle (AHB). Similar to MgtE, CBS-pair domain of CNNM also dimerizes in a head-to-head fashion. In addition, the CorC domain is hypothesized to reside on either side of CBS-pair domain based on the CorC structure (PDB: 4HG0), thus also resembling the N-domain of MgtE. Therefore, it seems that the cytosolic domains of MgtE and MtCNNM share a similar structural rearrangement.

Other than the CBS-pair domain, the three proteins share no sequence or structural similarities. The TMD all have a different fold. The total number of TM helices vary from six to ten. Therefore, it seems that nature has evolved multiple structural scaffolds to selectively transport Mg^{2+} into and out of cells. This is in stark contrast to K^{+} channels that have highly defined single pore architecture [177].

5.3 Features of transmembrane domain

5.3.1 Pore/cavity

In CorA, the ion-conducting pore is formed by five TM1 helices, while TM2 helices form the outer ring (**Fig. 5.2A**) [155-157]. The two most profound features of the ion pore are the lack of conserved acidic residues along the conducting pathway and its surprisingly overall length of ~ 55Å. The TM pore contains two hydrophobic constrictions: the "hydrophobic gate", a 1.9-nm-long constriction formed by pore-lining residues Met291, Leu294, Ala298, and Met302; and the "lower leucine constriction" (LC), a shorter steric bottle neck formed by the side chain of Leu280. In all crystal structures of CorA, both hydrophobic constrictions are too narrow to be hydrated, suggesting that the channel is in its closed, non-conductive state. However, portions of the pore are wide enough to accommodate a Mg^{2+} ion with its first hydration shell intact. From all the available CorA crystal structures, a total of eight divalent cations have been assigned along the ion pore. In fact, MjCorA appears to house up to five hydrated Mg^{2+} ions simultaneously [169], implying that CorA contains a multi-ion pore with a knock-on conduction mechanism reminiscent of K^{+} channels [177].

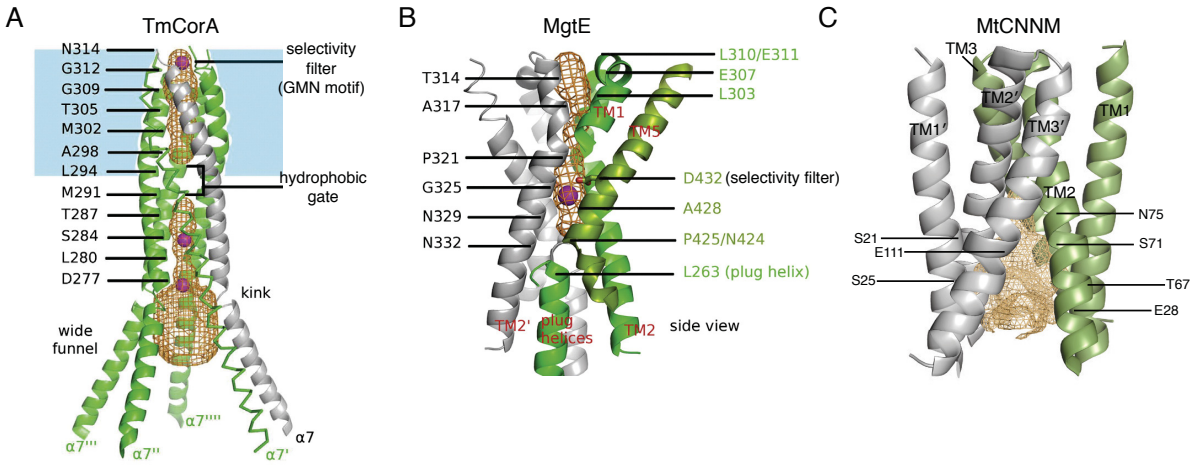

Figure 5.2 Ion pore or cavity structures of three magnesium transporters

Ion pore or cavity structures of (A) TmCorA (PDB: 4EED [170]), (B) MgtE (PDB: 2ZY9 [141]), and (C) MtCNNM. Only the pore forming helices are shown. Pore lining residues are indicated. Mg^{2+} ions are shown as magenta spheres. The solvent accessible pore volume is rendered as an orange mesh. Panel A & B are adapted from [106].

The ion-conducting pore in MgtE is formed by three TM helices (TM1, TM2, and TM5) of each protomer interlacing around the central ion pore while TM3 and TM4 form the periphery (**Fig. 5.2B**) [142]. The solvent-accessible pore is ~30 Å long. The pore diameter near the cytoplasmic end is ~6 Å, while that of the periplasmic end is ~15Å. At the periplasmic entrance, there are two cation binding sites that represent periplasmic gating sites [174]. Binding of Mn^{2+} to these sites strongly inhibit the transport activity MgtE, suggesting that these gating sites may fix the protein in a closed form, thereby preventing excess uptake of toxic cations, such as Fe^{2+}, Co^{2+}, Ni^{2+}, and Mn^{2+} [174]. Following the periplasmic gate is a narrow constriction with numerous glycine and proline residues imparting a kinked and slighted twisted appearance. The selectivity filter resides in the middle, then the constriction becomes occluded by the plug helices at the cytoplasmic side.

For MtCNNM, there is no central pore formed by the TMD. Instead, there is a large negatively charged cavity decorated with many conserved polar residues (**Fig. 5.2C**). It is possible that the current structure is in a non-conductive state. However, due to the Na^+/Mg^{2+} exchange evidence from the human counterpart [20], it is unlikely that CNNM would transport Na^+ and Mg^{2+} in opposite directions as a channel. Therefore, it seems more likely that CNNM would behave as a secondary active transporter. In fact, an electron density that resembled Na^+ is observed to bind in the negatively charged cavity. This suggests that the structure here represents the inward-facing state in which the Na^+ is bound, and upon dissociation, Mg^{2+} would be able to bind and be exported out of the cell.

5.3.2 Selectivity filter

For CorA, there is a universally conserved GMN motif that lines the extracellular pore entrance [155-157]. The bound Mg^{2+} ion is coordinated through its first shell of waters to the asparagine sidechain and glycine backbone carbonyl atoms. This interaction is notably asymmetric with respect to the central pore axis, as are all Mg^{2+} coordination observed within the CorA pore. This GMN motif supports the selection of first shell hydrated Mg^{2+} ions. The GMN motif is intolerant to substitutions. Gly312 is absolutely required for magnesium uptake; Met313 is absolutely required for pentamer integrity in the open conformation, and Asn314 plays a role in both functions [178]. The transport of hydrated Mg^{2+} makes intuitive sense as excessively

removing the first hydration shell from Mg^{2+} would be most demanding energetically and counterproductive to achieving high flux rates.

In MgtE, the selectivity filter in the middle of the ion-conducting pore is dictated by a conserved aspartate residue (Asp432). At the M1 site, a fully octahedrally hydrated Mg^{2+} is coordinated by the carboxylate groups of Asp432 sidechains [174]. Crystal structures with Mn^{2+} and Ca^{2+} bound at this site have also been obtained [174]. Mn^{2+} also assumes an octahedral hydration geometry similar to Mg^{2+}, whereas the coordination geometry of Ca^{2+} is dynamic and exhibit a broad range of coordination numbers, differing from Mg^{2+} and Mn^{2+} ions. This suggests that the M1 site specifically recognizes divalent cations that can assume an octahedral geometry, which may be important for selective transport of Mg^{2+} over other cations, such as Na^{+}, K^{+} and Ca^{2+}.

For MtCNNM, due to the absence of a bound Mg^{2+} in the cavity, the mechanism of ion selectivity is unclear. However, in the cavity there are two conserved glutamate residues (Glu28 and Glu111) that could serve as potential Mg^{2+} binding sites. Perhaps in another conformation, these two glutamate residues would together be involved in coordinating a hydrated Mg^{2+} ion.

5.4 Features of cytosolic domains

5.4.1 Mg^{2+} binding sites

For CorA, there are five regulatory M1 ions assigned as Mg^{2+} or Ca^{2+} that are coordinated directly between the sidechains of Asp89 (α3) and Asp253 (α7′) (**Fig. 5.3A**) [155-157]. At the subunit interface, five additional divalent cations are bound through water molecules at the M2 site. The strategic positioning of these ten bound divalent cations symmetrically around the CorA pentamer represented key regulatory sites. Since they shield an otherwise electrostatically repulsive interface, dissociation of bound M1 and M2 metals under low Mg^{2+} conditions would propagate significant structural changes throughout TmCorA. Studies suggest that divalent cation binding to these sites locks TmCorA in a transport incompetent conformation and that loss of these cations leads to an open conformation [170].

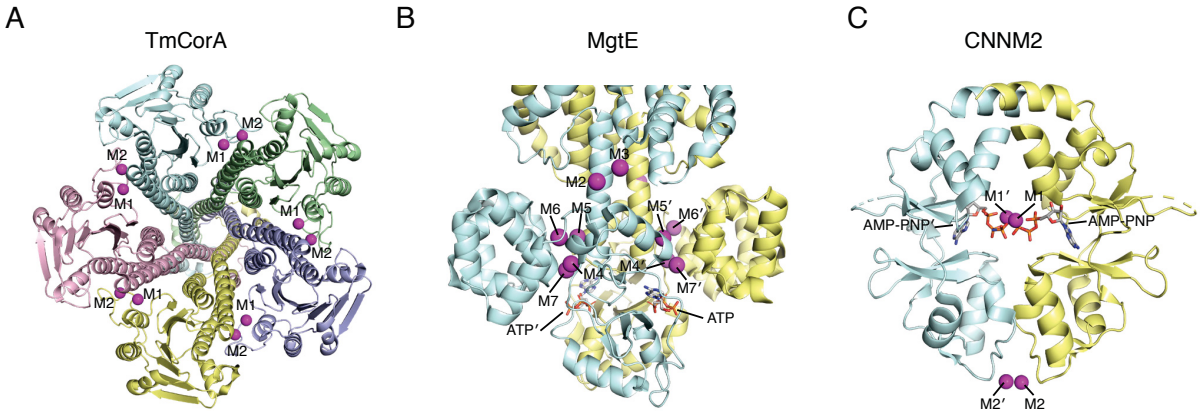

Figure 5.3 Mg^{2+}-binding sites in cytosolic domains of magnesium transporters
Cytosolic Mg^{2+} and ATP-binding sites in (A) TmCorA (PDB: 4I0U [171]), (B) MgtE (PDB: 5X9H [175]), and (C) CNNM2 (PDB: 6N7E [153]). Mg^{2+} ions are shown as magenta spheres.

In MgtE, there are twelve Mg^{2+} binding sites in the cytosolic domain with six Mg^{2+} ions (named M2-M7) per protomer (**Fig. 5.3B**) [141]. M2 and M3 are bound near the membrane-proximal interface of the plug helix, CBS2, and TM5. M4-M7 ions further connect the intracellular ends of plug helices, the N-domains, and CBS-pair domains from neighboring subunits. The M2, M4, M5, and M6 ions are involved in direct protein interactions coordinated mainly by glutamate and aspartate residues. While the high concentration of Mg^{2+} used in

crystallization (200 mM $MgCl_2$) may lead to identification of non-physiological binding sites, these structural bindings implicate roles in Mg^{2+}-sensing.

As for CNNM, there are two magnesium ions observed in the structure of human CNNM2 cytosolic fragment bound to Mg^{2+}-AMP-PNP (**Fig. 5.3C**) [153]. These two Mg^{2+} ions are coordinated by a cluster of acidic residues at the base of CBS1 motifs of each protomer. Although mutation of this acidic cluster did not abolish Mg^{2+} efflux function, *in vitro* ITC studies showed that mutation of these aspartate residues lead to a two-fold decrease in ATP binding. Therefore, this site could potentially serve as a weak regulatory site. On the other hand, there are many conserved acidic residues in the acidic helical bundle between TMD and CBS-pair domain of MtCNNM. Even though there were no electron densities observed, these acidic patches could serve as potential Mg^{2+} binding sites that may play roles in sensing intracellular Mg^{2+} level.

5.4.2 ATP-binding sites

Both MgtE and CNNM contain a CBS-pair domain that have ATP-binding ability while CorA does not. MgtE binds ATP with an affinity of 172 and 415 μM in presence and absence of Mg^{2+}, respectively [175]. The ATP molecule is exclusively recognized by the CBS-pair domain (**Fig. 5.3B**). Interesting, the phosphate groups of the ATP are 5.4 Å away from the closest Mg^{2+} ions in the structure, suggesting ATP binding to MgtE may not be directly coupled to Mg^{2+} binding.

On the other hand, cytosolic fragment of CNNM2 and CNNM4 bind ATP with an affinity of 4.3 and 2.8 μM, respectively in presence of Mg^{2+}, while no binding is observed in absence of Mg^{2+} [153]. In contrast, binding of ATP to archaeal CNNM (MtCNNM) is independent of Mg^{2+} with affinity of 1.47 μM and a three-fold increase to 0.59 μM with Mg^{2+}. The discrepancy between human and archaeal CNNMs could be due to differences in ATP or Mg^{2+} concentrations in archaeal and human cells. Structurally, the ATP binds to the CBS-pair domain and an Mg^{2+} ion is coordinated by the three phosphates of ATP (**Fig. 5.3C**), differing from MgtE.

5.4.3 Mg^{2+}-induced conformational changes

In presence of Mg^{2+}, CorA exists in a symmetric pentamer with ten Mg^{2+} ions bound between the funnel domains [155-157]. Whereas in the structure with Cs^+ instead of Mg^{2+}, the

monovalent ion shows irregular occupancy, resulting in a structurally asymmetric pentamer, suggesting that movement cations are not able to lock CorA in a closed, symmetric state [170]. From the cryo-EM studies, in the absence of bound Mg^{2+} ions, four of the five subunits are displaced to variable extends (~10-25 Å) by hinge-like motions are large as ~35° at the stalk helix [172]. Reduction of intracellular Mg^{2+} level leads to interfacial Mg^{2+} release and subsequent large-range cytoplasmic domain rearrangements. These conformational changes are suggested to drive gating transitions along the TM segments.

In the case of MgtE, all the existing full-length MgtE structures are in the Mg^{2+}-bound form. However, crystal structures of the isolated intracellular domain in absence of Mg^{2+} revealed striking domain rearrangements [142]. The N-domain in the unliganded state has disengaged from its interactions with the CBS-pair domain and the plug helix. The CBS2 motifs become separated due to electrostatic repulsion generated by the departure of Mg^{2+} ions, and the plug helices undergoes a significant displacement that would effectively "de-cork" these helices from their block of the ion conduction pathway. The M5 ion, which bridges the plug helix and CBS2 motif, was reported to be indispensable for maintaining the closed state. Mutational crippling of the M5 site abolished Mg^{2+}-dependent regulation, supporting the conclusion that intracellular domains are responsible for Mg^{2+}-sensing and channel gating [141]. In addition, MgtE lacking the N-domain showed reduced Mg^{2+}-dependent inhibition as well as an increased open probability, implicating N-domain directly in MgtE function [141]. These conformational changes are supported by experiments from paramagnetic relaxation enhancement (PRE) experiments and molecular dynamics simulations [143, 179].

As shown in Chapter 3, upon Mg^{2+}-ATP binding, CBS-pair domain of CNNM changes from an open conformation to a closed, flat, disc-like conformation [153]. This is similar to MgtE, in which ligand-binding results in dimerization of CBS-pair domain. However, in this case, CBS1 motifs are the ones that become separated instead of CBS2 motifs. Despite only having the Mg^{2+}-ATP bound conformation in the structure containing TMD, the conformational changes of CBS-pair domains are likely to be translated to the AHB and TMD and affect transport function. Since the inability to bind ATP strongly correlates with loss of Mg^{2+} efflux function, it appears that ligand binding to CNNM cytosolic domain would activate its transport function. This is in clear contrast to CorA and MgtE, in which binding of multiple Mg^{2+} ions to the intracellular domains inactivate the channels.

5.5 Concluding remarks

Compared to MgtE and CorA, structural studies of CNNM still have a long way to go. Currently, there is only one structure containing the TMD, representing only one snapshot of the transport cycle. Assuming transport through a rocker-switch mechanism, more structures of different conformations would be needed to fully understand the mechanism of transport by CNNM. This thesis is a step toward understanding the mechanism of Mg^{2+} transport by CNNM proteins. The structural and functional insights could provide the framework for design of new therapeutics targeting CNNM for the treatment of cancer and other associated diseases, such as hypomagnesemia and Jalili syndrome.

References

1. Ebel, H. & Gunther, T. (1980) Magnesium metabolism: a review, *J Clin Chem Clin Biochem.* **18**, 257-70.

2. de Baaij, J. H., Hoenderop, J. G. & Bindels, R. J. (2015) Magnesium in man: implications for health and disease, *Physiol Rev.* **95**, 1-46.

3. Brautigam, C. A. & Steitz, T. A. (1998) Structural and functional insights provided by crystal structures of DNA polymerases and their substrate complexes, *Curr Opin Struct Biol.* **8**, 54-63.

4. Klein, D. J., Moore, P. B. & Steitz, T. A. (2004) The contribution of metal ions to the structural stability of the large ribosomal subunit, *RNA.* **10**, 1366-79.

5. Suh, W. C., Leirmo, S. & Record, M. T., Jr. (1992) Roles of Mg2+ in the mechanism of formation and dissociation of open complexes between Escherichia coli RNA polymerase and the lambda PR promoter: kinetic evidence for a second open complex requiring Mg2+, *Biochemistry.* **31**, 7815-25.

6. Jahnen-Dechent, W. & Ketteler, M. (2012) Magnesium basics, *Clin Kidney J.* **5**, i3-i14.

7. Li, F. Y., Chaigne-Delalande, B., Kanellopoulou, C., Davis, J. C., Matthews, H. F., Douek, D. C., Cohen, J. I., Uzel, G., Su, H. C. & Lenardo, M. J. (2011) Second messenger role for Mg2+ revealed by human T-cell immunodeficiency, *Nature.* **475**, 471-6.

8. Rude, R. K. (1998) Magnesium deficiency: a cause of heterogeneous disease in humans, *J Bone Miner Res.* **13**, 749-58.

9. Elin, R. J. (1987) Assessment of magnesium status, *Clin Chem.* **33**, 1965-70.

10. Alfrey, A. C., Miller, N. L. & Trow, R. (1974) Effect of age and magnesium depletion on bone magnesium pools in rats, *J Clin Invest.* **54**, 1074-81.

11. Kroll, M. H. & Elin, R. J. (1985) Relationships between magnesium and protein concentrations in serum, *Clin Chem.* **31**, 244-6.

12. Glaudemans, B., Knoers, N. V., Hoenderop, J. G. & Bindels, R. J. (2010) New molecular players facilitating Mg(2+) reabsorption in the distal convoluted tubule, *Kidney Int.* **77**, 17-22.

13. Maguire, M. E. & Cowan, J. A. (2002) Magnesium chemistry and biochemistry, *Biometals.* **15**, 203-10.

14. Wang, C. Y., Shi, J. D., Yang, P., Kumar, P. G., Li, Q. Z., Run, Q. G., Su, Y. C., Scott, H. S., Kao, K. J. & She, J. X. (2003) Molecular cloning and characterization of a novel gene family of four ancient conserved domain proteins (ACDP), *Gene.* **306**, 37-44.
15. Edgar, R. C. (2004) MUSCLE: multiple sequence alignment with high accuracy and high throughput, *Nucleic Acids Res.* **32**, 1792-7.
16. Kumar, S., Stecher, G., Li, M., Knyaz, C. & Tamura, K. (2018) MEGA X: Molecular Evolutionary Genetics Analysis across Computing Platforms, *Mol Biol Evol.* **35**, 1547-1549.
17. Meyer, T. E., Verwoert, G. C., Hwang, S. J., Glazer, N. L., Smith, A. V., van Rooij, F. J., Ehret, G. B., Boerwinkle, E., Felix, J. F., Leak, T. S., Harris, T. B., Yang, Q., Dehghan, A., Aspelund, T., Katz, R., Homuth, G., Kocher, T., Rettig, R., Ried, J. S., Gieger, C., Prucha, H., Pfeufer, A., Meitinger, T., Coresh, J., Hofman, A., Sarnak, M. J., Chen, Y. D., Uitterlinden, A. G., Chakravarti, A., Psaty, B. M., van Duijn, C. M., Kao, W. H., Witteman, J. C., Gudnason, V., Siscovick, D. S., Fox, C. S., Kottgen, A., Genetic Factors for Osteoporosis, C., Meta Analysis of, G. & Insulin Related Traits, C. (2010) Genome-wide association studies of serum magnesium, potassium, and sodium concentrations identify six Loci influencing serum magnesium levels, *PLoS Genet.* **6**.
18. Goytain, A. & Quamme, G. A. (2005) Functional characterization of ACDP2 (ancient conserved domain protein), a divalent metal transporter, *Physiol Genomics.* **22**, 382-9.
19. Stuiver, M., Lainez, S., Will, C., Terryn, S., Gunzel, D., Debaix, H., Sommer, K., Kopplin, K., Thumfart, J., Kampik, N. B., Querfeld, U., Willnow, T. E., Nemec, V., Wagner, C. A., Hoenderop, J. G., Devuyst, O., Knoers, N. V., Bindels, R. J., Meij, I. C. & Muller, D. (2011) CNNM2, encoding a basolateral protein required for renal Mg2+ handling, is mutated in dominant hypomagnesemia, *Am J Hum Genet.* **88**, 333-43.
20. Yamazaki, D., Funato, Y., Miura, J., Sato, S., Toyosawa, S., Furutani, K., Kurachi, Y., Omori, Y., Furukawa, T., Tsuda, T., Kuwabata, S., Mizukami, S., Kikuchi, K. & Miki, H. (2013) Basolateral Mg2+ extrusion via CNNM4 mediates transcellular Mg2+ transport across epithelia: a mouse model, *PLoS Genet.* **9**, e1003983.
21. Funato, Y., Yamazaki, D. & Miki, H. (2017) Renal function of cyclin M2 Mg2+ transporter maintains blood pressure, *J Hypertens.* **35**, 585-592.

22. Wang, C. Y., Yang, P., Shi, J. D., Purohit, S., Guo, D., An, H., Gu, J. G., Ling, J., Dong, Z. & She, J. X. (2004) Molecular cloning and characterization of the mouse Acdp gene family, *BMC Genomics.* **5**, 7.
23. Quamme, G. A. (2010) Molecular identification of ancient and modern mammalian magnesium transporters, *Am J Physiol Cell Physiol.* **298**, C407-29.
24. de Baaij, J. H., Stuiver, M., Meij, I. C., Lainez, S., Kopplin, K., Venselaar, H., Muller, D., Bindels, R. J. & Hoenderop, J. G. (2012) Membrane topology and intracellular processing of cyclin M2 (CNNM2), *J Biol Chem.* **287**, 13644-55.
25. Hirata, Y., Funato, Y. & Miki, H. (2014) Basolateral sorting of the Mg(2)(+) transporter CNNM4 requires interaction with AP-1A and AP-1B, *Biochem Biophys Res Commun.* **455**, 184-9.
26. Voets, T., Nilius, B., Hoefs, S., van der Kemp, A. W., Droogmans, G., Bindels, R. J. & Hoenderop, J. G. (2004) TRPM6 forms the Mg2+ influx channel involved in intestinal and renal Mg2+ absorption, *J Biol Chem.* **279**, 19-25.
27. Ryazanova, L. V., Rondon, L. J., Zierler, S., Hu, Z., Galli, J., Yamaguchi, T. P., Mazur, A., Fleig, A. & Ryazanov, A. G. (2010) TRPM7 is essential for Mg(2+) homeostasis in mammals, *Nat Commun.* **1**, 109.
28. Sponder, G., Svidova, S., Schweigel, M., Vormann, J. & Kolisek, M. (2010) Splice-variant 1 of the ancient domain protein 2 (ACDP2) complements the magnesium-deficient growth phenotype of Salmonella enterica sv. typhimurium strain MM281, *Magnes Res.* **23**, 105-14.
29. Arjona, F. J., de Baaij, J. H., Schlingmann, K. P., Lameris, A. L., van Wijk, E., Flik, G., Regele, S., Korenke, G. C., Neophytou, B., Rust, S., Reintjes, N., Konrad, M., Bindels, R. J. & Hoenderop, J. G. (2014) CNNM2 mutations cause impaired brain development and seizures in patients with hypomagnesemia, *PLoS Genet.* **10**, e1004267.
30. Sponder, G., Mastrototaro, L., Kurth, K., Merolle, L., Zhang, Z., Abdulhanan, N., Smorodchenko, A., Wolf, K., Fleig, A., Penner, R., Iotti, S., Aschenbach, J. R., Vormann, J. & Kolisek, M. (2016) Human CNNM2 is not a Mg(2+) transporter per se, *Pflugers Arch.* **468**, 1223-40.
31. Funato, Y., Furutani, K., Kurachi, Y. & Miki, H. (2018) CrossTalk proposal: CNNM proteins are Na(+) /Mg(2+) exchangers playing a central role in transepithelial Mg(2+) (re)absorption, *J Physiol.* **596**, 743-746.

32. Arjona, F. J. & de Baaij, J. H. F. (2018) CrossTalk opposing view: CNNM proteins are not Na(+) /Mg(2+) exchangers but Mg(2+) transport regulators playing a central role in transepithelial Mg(2+) (re)absorption, *J Physiol.* **596**, 747-750.
33. Funato, Y., Furutani, K., Kurachi, Y. & Miki, H. (2018) Rebuttal from Yosuke Funato, Kazuharu Furutani, Yoshihisa Kurachi and Hiroaki Miki, *J Physiol.* **596**, 751.
34. Arjona, F. J., Chen, Y. X., Flik, G., Bindels, R. J. & Hoenderop, J. G. (2013) Tissue-specific expression and in vivo regulation of zebrafish orthologues of mammalian genes related to symptomatic hypomagnesemia, *Pflugers Arch.* **465**, 1409-21.
35. Ishii, T., Funato, Y., Hashizume, O., Yamazaki, D., Hirata, Y., Nishiwaki, K., Kono, N., Arai, H. & Miki, H. (2016) Mg2+ Extrusion from Intestinal Epithelia by CNNM Proteins Is Essential for Gonadogenesis via AMPK-TORC1 Signaling in Caenorhabditis elegans, *PLoS Genet.* **12**, e1006276.
36. Yang, M., Jensen, L. T., Gardner, A. J. & Culotta, V. C. (2005) Manganese toxicity and Saccharomyces cerevisiae Mam3p, a member of the ACDP (ancient conserved domain protein) family, *Biochem J.* **386**, 479-87.
37. Hmiel, S. P., Snavely, M. D., Miller, C. G. & Maguire, M. E. (1986) Magnesium transport in Salmonella typhimurium: characterization of magnesium influx and cloning of a transport gene, *J Bacteriol.* **168**, 1444-50.
38. Gibson, M. M., Bagga, D. A., Miller, C. G. & Maguire, M. E. (1991) Magnesium transport in Salmonella typhimurium: the influence of new mutations conferring Co2+ resistance on the CorA Mg2+ transport system, *Mol Microbiol.* **5**, 2753-62.
39. Armitano, J., Redder, P., Guimaraes, V. A. & Linder, P. (2016) An Essential Factor for High Mg(2+) Tolerance of Staphylococcus aureus, *Front Microbiol.* **7**, 1888.
40. Trachsel, E., Redder, P., Linder, P. & Armitano, J. (2019) Genetic screens reveal novel major and minor players in magnesium homeostasis of Staphylococcus aureus, *PLoS Genet.* **15**, e1008336.
41. Hirata, Y., Funato, Y., Takano, Y. & Miki, H. (2014) Mg2+-dependent interactions of ATP with the cystathionine-beta-synthase (CBS) domains of a magnesium transporter, *J Biol Chem.* **289**, 14731-9.
42. Accogli, A., Scala, M., Calcagno, A., Napoli, F., Di Iorgi, N., Arrigo, S., Mancardi, M. M., Prato, G., Pisciotta, L., Nagel, M., Severino, M. & Capra, V. (2019) CNNM2 homozygous

mutations cause severe refractory hypomagnesemia, epileptic encephalopathy and brain malformations, *Eur J Med Genet.* **62**, 198-203.
43. Garcia-Castano, A., Madariaga, L., Anton-Gamero, M., Mejia, N., Ponce, J., Gomez-Conde, S., Perez de Nanclares, G., De la Hoz, A. B., Martinez, R., Saso, L., Martinez de LaPiscina, I., Urrutia, I., Velasco, O., Aguayo, A., Castano, L. & Gaztambide, S. (2020) Novel variant in the CNNM2 gene associated with dominant hypomagnesemia, *PLoS One.* **15**, e0239965.
44. Parry, D. A., Mighell, A. J., El-Sayed, W., Shore, R. C., Jalili, I. K., Dollfus, H., Bloch-Zupan, A., Carlos, R., Carr, I. M., Downey, L. M., Blain, K. M., Mansfield, D. C., Shahrabi, M., Heidari, M., Aref, P., Abbasi, M., Michaelides, M., Moore, A. T., Kirkham, J. & Inglehearn, C. F. (2009) Mutations in CNNM4 cause Jalili syndrome, consisting of autosomal-recessive cone-rod dystrophy and amelogenesis imperfecta, *Am J Hum Genet.* **84**, 266-73.
45. Kiessling, F., Mitter, D., Langmann, T. & Müller, D. T. H. (2016) Novel deletion in the CNNM4 gene in siblings with jalili syndrome, *Int J Ophthalmol Clin Res.* **3**, 046.
46. Coppieters, F., Van Schil, K., Bauwens, M., Verdin, H., De Jaegher, A., Syx, D., Sante, T., Lefever, S., Abdelmoula, N. B., Depasse, F., Casteels, I., de Ravel, T., Meire, F., Leroy, B. P. & De Baere, E. (2014) Identity-by-descent-guided mutation analysis and exome sequencing in consanguineous families reveals unusual clinical and molecular findings in retinal dystrophy, *Genet Med.* **16**, 671-80.
47. Wang, H., Wang, X., Zou, X., Xu, S., Li, H., Soens, Z. T., Wang, K., Li, Y., Dong, F., Chen, R. & Sui, R. (2015) Comprehensive Molecular Diagnosis of a Large Chinese Leber Congenital Amaurosis Cohort, *Invest Ophthalmol Vis Sci.* **56**, 3642-55.
48. Polok, B., Escher, P., Ambresin, A., Chouery, E., Bolay, S., Meunier, I., Nan, F., Hamel, C., Munier, F. L., Thilo, B., Megarbane, A. & Schorderet, D. F. (2009) Mutations in CNNM4 cause recessive cone-rod dystrophy with amelogenesis imperfecta, *Am J Hum Genet.* **84**, 259-65.
49. Prasov, L., Ullah, E., Turriff, A. E., Warner, B. M., Conley, J., Mark, P. R., Hufnagel, R. B. & Huryn, L. A. (2020) Expanding the genotypic spectrum of Jalili syndrome: Novel CNNM4 variants and uniparental isodisomy in a north American patient cohort, *Am J Med Genet A.* **182**, 493-497.
50. Hirji, N., Bradley, P. D., Li, S., Vincent, A., Pennesi, M. E., Thomas, A. S., Heon, E., Bhan, A., Mahroo, O. A., Robson, A., Inglehearn, C. F., Moore, A. T. & Michaelides, M. (2018) Jalili

Syndrome: Cross-sectional and Longitudinal Features of Seven Patients With Cone-Rod Dystrophy and Amelogenesis Imperfecta, *Am J Ophthalmol.* **188**, 123-130.
51. Maia, C. M. F., Machado, R. A., Gil-da-Silva-Lopes, V. L., Lustosa-Mendes, E., Rim, P. H. H., Dias, V. O., Martelli, D. R. B., Nasser, L. S., Coletta, R. D. & Martelli-Junior, H. (2018) Report of two unrelated families with Jalili syndrome and a novel nonsense heterozygous mutation in CNNM4 gene, *Eur J Med Genet.* **61**, 384-387.
52. Rahimi-Aliabadi, S., Daftarian, N., Ahmadieh, H., Emamalizadeh, B., Jamshidi, J., Tafakhori, A., Ghaedi, H., Noroozi, R., Taghavi, S., Ahmadifard, A., Alehabib, E., Andarva, M., Shokraeian, P., Atakhorrami, M. & Darvish, H. (2016) A novel mutation and variable phenotypic expression in a large consanguineous pedigree with Jalili syndrome, *Eye (Lond).* **30**, 1424-1432.
53. Parveen, A., Mirza, M. U., Vanmeert, M., Akhtar, J., Bashir, H., Khan, S., Shehzad, S., Froeyen, M., Ahmed, W., Ansar, M. & Wasif, N. (2019) A novel pathogenic missense variant in CNNM4 underlying Jalili syndrome: Insights from molecular dynamics simulations, *Mol Genet Genomic Med.* **7**, e902.
54. Lopez Torres, L., Schorderet, D., Valmaggia, C. & Todorova, M. (2015) A novel mutation in CNNM 4 (G492C) associated with Jalili Syndrome, *Acta Ophthalmologica.* **93**.
55. Abu-Safieh, L., Alrashed, M., Anazi, S., Alkuraya, H., Khan, A. O., Al-Owain, M., Al-Zahrani, J., Al-Abdi, L., Hashem, M., Al-Tarimi, S., Sebai, M. A., Shamia, A., Ray-Zack, M. D., Nassan, M., Al-Hassnan, Z. N., Rahbeeni, Z., Waheeb, S., Alkharashi, A., Abboud, E., Al-Hazzaa, S. A. & Alkuraya, F. S. (2013) Autozygome-guided exome sequencing in retinal dystrophy patients reveals pathogenetic mutations and novel candidate disease genes, *Genome Res.* **23**, 236-47.
56. Prasad, M. K., Geoffroy, V., Vicaire, S., Jost, B., Dumas, M., Le Gras, S., Switala, M., Gasse, B., Laugel-Haushalter, V., Paschaki, M., Leheup, B., Droz, D., Dalstein, A., Loing, A., Grollemund, B., Muller-Bolla, M., Lopez-Cazaux, S., Minoux, M., Jung, S., Obry, F., Vogt, V., Davideau, J. L., Davit-Beal, T., Kaiser, A. S., Moog, U., Richard, B., Morrier, J. J., Duprez, J. P., Odent, S., Bailleul-Forestier, I., Rousset, M. M., Merametdijan, L., Toutain, A., Joseph, C., Giuliano, F., Dahlet, J. C., Courval, A., El Alloussi, M., Laouina, S., Soskin, S., Guffon, N., Dieux, A., Doray, B., Feierabend, S., Ginglinger, E., Fournier, B., de la Dure Molla, M., Alembik, Y., Tardieu, C., Clauss, F., Berdal, A., Stoetzel, C., Maniere, M. C., Dollfus, H. &

Bloch-Zupan, A. (2016) A targeted next-generation sequencing assay for the molecular diagnosis of genetic disorders with orodental involvement, *J Med Genet.* **53**, 98-110.
57. Topcu, V., Alp, M. Y., Alp, C. K., Bakir, A., Geylan, D. & Yilmazoglu, M. O. (2017) A new familial case of Jalili syndrome caused by a novel mutation in CNNM4, *Ophthalmic Genet.* **38**, 161-166.
58. Doucette, L., Green, J., Black, C., Schwartzentruber, J., Johnson, G. J., Galutira, D. & Young, T. L. (2013) Molecular genetics of achromatopsia in Newfoundland reveal genetic heterogeneity, founder effects and the first cases of Jalili syndrome in North America, *Ophthalmic Genet.* **34**, 119-29.
59. Li, S., Xi, Q., Zhang, X., Yu, D., Li, L., Jiang, Z., Chen, Q., Wang, Q. K. & Traboulsi, E. I. (2018) Identification of a mutation in CNNM4 by whole exome sequencing in an Amish family and functional link between CNNM4 and IQCB1, *Mol Genet Genomics.* **293**, 699-710.
60. Genovese, G., Fromer, M., Stahl, E. A., Ruderfer, D. M., Chambert, K., Landen, M., Moran, J. L., Purcell, S. M., Sklar, P., Sullivan, P. F., Hultman, C. M. & McCarroll, S. A. (2016) Increased burden of ultra-rare protein-altering variants among 4,877 individuals with schizophrenia, *Nat Neurosci.* **19**, 1433-1441.
61. Jalili, I. K. & Smith, N. J. (1988) A progressive cone-rod dystrophy and amelogenesis imperfecta: a new syndrome, *J Med Genet.* **25**, 738-40.
62. Crawford, P. J., Aldred, M. & Bloch-Zupan, A. (2007) Amelogenesis imperfecta, *Orphanet J Rare Dis.* **2**, 17.
63. Michaelides, M., Hardcastle, A. J., Hunt, D. M. & Moore, A. T. (2006) Progressive cone and cone-rod dystrophies: phenotypes and underlying molecular genetic basis, *Surv Ophthalmol.* **51**, 232-58.
64. Jalevik, B., Odelius, H., Dietz, W. & Noren, J. (2001) Secondary ion mass spectrometry and X-ray microanalysis of hypomineralized enamel in human permanent first molars, *Arch Oral Biol.* **46**, 239-47.
65. Funato, Y., Yamazaki, D., Mizukami, S., Du, L., Kikuchi, K. & Miki, H. (2014) Membrane protein CNNM4-dependent Mg2+ efflux suppresses tumor progression, *J Clin Invest.* **124**, 5398-410.
66. Hardy, S., Uetani, N., Wong, N., Kostantin, E., Labbe, D. P., Begin, L. R., Mes-Masson, A., Miranda-Saavedra, D. & Tremblay, M. L. (2015) The protein tyrosine phosphatase PRL-2

interacts with the magnesium transporter CNNM3 to promote oncogenesis, *Oncogene.* **34**, 986-95.
67. Kostantin, E., Hardy, S., Valinsky, W. C., Kompatscher, A., de Baaij, J. H., Zolotarov, Y., Landry, M., Uetani, N., Martinez-Cruz, L. A., Hoenderop, J. G., Shrier, A. & Tremblay, M. L. (2016) Inhibition of PRL-2.CNNM3 Protein Complex Formation Decreases Breast Cancer Proliferation and Tumor Growth, *J Biol Chem.* **291**, 10716-25.
68. Rubin, H. (1975) Central role for magnesium in coordinate control of metabolism and growth in animal cells, *Proc Natl Acad Sci U S A.* **72**, 3551-5.
69. Rubin, H. (2005) Central roles of Mg2+ and MgATP2- in the regulation of protein synthesis and cell proliferation: significance for neoplastic transformation, *Adv Cancer Res.* **93**, 1-58.
70. Wolf, F. I. & Trapani, V. (2012) Magnesium and its transporters in cancer: a novel paradigm in tumour development, *Clin Sci (Lond).* **123**, 417-27.
71. Castiglioni, S. & Maier, J. A. (2011) Magnesium and cancer: a dangerous liason, *Magnes Res.* **24**, S92-100.
72. Newton-Cheh, C.Johnson, T.Gateva, V.Tobin, M. D.Bochud, M.Coin, L.Najjar, S. S.Zhao, J. H.Heath, S. C.Eyheramendy, S.Papadakis, K.Voight, B. F.Scott, L. J.Zhang, F.Farrall, M.Tanaka, T.Wallace, C.Chambers, J. C.Khaw, K. T.Nilsson, P.van der Harst, P.Polidoro, S.Grobbee, D. E.Onland-Moret, N. C.Bots, M. L.Wain, L. V.Elliott, K. S.Teumer, A.Luan, J.Lucas, G.Kuusisto, J.Burton, P. R.Hadley, D.McArdle, W. L.Wellcome Trust Case Control, C.Brown, M.Dominiczak, A.Newhouse, S. J.Samani, N. J.Webster, J.Zeggini, E.Beckmann, J. S.Bergmann, S.Lim, N.Song, K.Vollenweider, P.Waeber, G.Waterworth, D. M.Yuan, X.Groop, L.Orho-Melander, M.Allione, A.Di Gregorio, A.Guarrera, S.Panico, S.Ricceri, F.Romanazzi, V.Sacerdote, C.Vineis, P.Barroso, I.Sandhu, M. S.Luben, R. N.Crawford, G. J.Jousilahti, P.Perola, M.Boehnke, M.Bonnycastle, L. L.Collins, F. S.Jackson, A. U.Mohlke, K. L.Stringham, H. M.Valle, T. T.Willer, C. J.Bergman, R. N.Morken, M. A.Doring, A.Gieger, C.Illig, T.Meitinger, T.Org, E.Pfeufer, A.Wichmann, H. E.Kathiresan, S.Marrugat, J.O'Donnell, C. J.Schwartz, S. M.Siscovick, D. S.Subirana, I.Freimer, N. B.Hartikainen, A. L.McCarthy, M. I.O'Reilly, P. F.Peltonen, L.Pouta, A.de Jong, P. E.Snieder, H.van Gilst, W. H.Clarke, R.Goel, A.Hamsten, A., et al. (2009) Genome-wide association study identifies eight loci associated with blood pressure, *Nat Genet.* **41**, 666-76.

73. Schunkert, H.Konig, I. R.Kathiresan, S.Reilly, M. P.Assimes, T. L.Holm, H.Preuss, M.Stewart, A. F.Barbalic, M.Gieger, C.Absher, D.Aherrahrou, Z.Allayee, H.Altshuler, D.Anand, S. S.Andersen, K.Anderson, J. L.Ardissino, D.Ball, S. G.Balmforth, A. J.Barnes, T. A.Becker, D. M.Becker, L. C.Berger, K.Bis, J. C.Boekholdt, S. M.Boerwinkle, E.Braund, P. S.Brown, M. J.Burnett, M. S.Buysschaert, I.CardiogenicsCarlquist, J. F.Chen, L.Cichon, S.Codd, V.Davies, R. W.Dedoussis, G.Dehghan, A.Demissie, S.Devaney, J. M.Diemert, P.Do, R.Doering, A.Eifert, S.Mokhtari, N. E.Ellis, S. G.Elosua, R.Engert, J. C.Epstein, S. E.de Faire, U.Fischer, M.Folsom, A. R.Freyer, J.Gigante, B.Girelli, D.Gretarsdottir, S.Gudnason, V.Gulcher, J. R.Halperin, E.Hammond, N.Hazen, S. L.Hofman, A.Horne, B. D.Illig, T.Iribarren, C.Jones, G. T.Jukema, J. W.Kaiser, M. A.Kaplan, L. M.Kastelein, J. J.Khaw, K. T.Knowles, J. W.Kolovou, G.Kong, A.Laaksonen, R.Lambrechts, D.Leander, K.Lettre, G.Li, M.Lieb, W.Loley, C.Lotery, A. J.Mannucci, P. M.Maouche, S.Martinelli, N.McKeown, P. P.Meisinger, C.Meitinger, T.Melander, O.Merlini, P. A.Mooser, V.Morgan, T.Muhleisen, T. W.Muhlestein, J. B.Munzel, T.Musunuru, K.Nahrstaedt, J.Nelson, C. P.Nothen, M. M., et al. (2011) Large-scale association analysis identifies 13 new susceptibility loci for coronary artery disease, *Nat Genet.* **43**, 333-8.

74. Takeuchi, F., Isono, M., Katsuya, T., Yamamoto, K., Yokota, M., Sugiyama, T., Nabika, T., Fujioka, A., Ohnaka, K., Asano, H., Yamori, Y., Yamaguchi, S., Kobayashi, S., Takayanagi, R., Ogihara, T. & Kato, N. (2010) Blood pressure and hypertension are associated with 7 loci in the Japanese population, *Circulation.* **121**, 2302-9.

75. Dichgans, M., Malik, R., Konig, I. R., Rosand, J., Clarke, R., Gretarsdottir, S., Thorleifsson, G., Mitchell, B. D., Assimes, T. L., Levi, C., O'Donnell, C. J., Fornage, M., Thorsteinsdottir, U., Psaty, B. M., Hengstenberg, C., Seshadri, S., Erdmann, J., Bis, J. C., Peters, A., Boncoraglio, G. B., Marz, W., Meschia, J. F., Kathiresan, S., Ikram, M. A., McPherson, R., Stefansson, K., Sudlow, C., Reilly, M. P., Thompson, J. R., Sharma, P., Hopewell, J. C., Chambers, J. C., Watkins, H., Rothwell, P. M., Roberts, R., Markus, H. S., Samani, N. J., Farrall, M., Schunkert, H., Consortium, M., Consortium, C. A., Consortium, C. D. & International Stroke Genetics, C. (2014) Shared genetic susceptibility to ischemic stroke and coronary artery disease: a genome-wide analysis of common variants, *Stroke.* **45**, 24-36.

76. Laarman, M. D., Geeven, G., Barnett, P., Netherlands Brain, B., Rinkel, G. J. E., de Laat, W., Ruigrok, Y. M. & Bakkers, J. (2019) Chromatin Conformation Links Putative Enhancers in

Intracranial Aneurysm-Associated Regions to Potential Candidate Genes, *J Am Heart Assoc.* **8**, e011201.
77. Yamazaki, D., Miyata, H., Funato, Y., Fujihara, Y., Ikawa, M. & Miki, H. (2016) The Mg2+ transporter CNNM4 regulates sperm Ca2+ homeostasis and is essential for reproduction, *J Cell Sci.* **129**, 1940-9.
78. Yamazaki, D., Funato, Y., Miyata, H., Ikawa, M. & Miki, H. (2016) Complementary role of CNNM2 in sperm motility and Ca(2+) influx during capacitation, *Biochem Biophys Res Commun.* **474**, 441-446.
79. Schizophrenia Psychiatric Genome-Wide Association Study, C. (2011) Genome-wide association study identifies five new schizophrenia loci, *Nat Genet.* **43**, 969-76.
80. Aberg, K. A., Liu, Y., Bukszar, J., McClay, J. L., Khachane, A. N., Andreassen, O. A., Blackwood, D., Corvin, A., Djurovic, S., Gurling, H., Ophoff, R., Pato, C. N., Pato, M. T., Riley, B., Webb, T., Kendler, K., O'Donovan, M., Craddock, N., Kirov, G., Owen, M., Rujescu, D., St Clair, D., Werge, T., Hultman, C. M., Delisi, L. E., Sullivan, P. & van den Oord, E. J. (2013) A comprehensive family-based replication study of schizophrenia genes, *JAMA Psychiatry.* **70**, 573-81.
81. Lotan, A., Fenckova, M., Bralten, J., Alttoa, A., Dixson, L., Williams, R. W. & van der Voet, M. (2014) Neuroinformatic analyses of common and distinct genetic components associated with major neuropsychiatric disorders, *Front Neurosci.* **8**, 331.
82. Cross-Disorder Group of the Psychiatric Genomics, C. (2013) Identification of risk loci with shared effects on five major psychiatric disorders: a genome-wide analysis, *Lancet.* **381**, 1371-1379.
83. Ripke, S.O'Dushlaine, C.Chambert, K.Moran, J. L.Kahler, A. K.Akterin, S.Bergen, S. E.Collins, A. L.Crowley, J. J.Fromer, M.Kim, Y.Lee, S. H.Magnusson, P. K.Sanchez, N.Stahl, E. A.Williams, S.Wray, N. R.Xia, K.Bettella, F.Borglum, A. D.Bulik-Sullivan, B. K.Cormican, P.Craddock, N.de Leeuw, C.Durmishi, N.Gill, M.Golimbet, V.Hamshere, M. L.Holmans, P.Hougaard, D. M.Kendler, K. S.Lin, K.Morris, D. W.Mors, O.Mortensen, P. B.Neale, B. M.O'Neill, F. A.Owen, M. J.Milovancevic, M. P.Posthuma, D.Powell, J.Richards, A. L.Riley, B. P.Ruderfer, D.Rujescu, D.Sigurdsson, E.Silagadze, T.Smit, A. B.Stefansson, H.Steinberg, S.Suvisaari, J.Tosato, S.Verhage, M.Walters, J. T.Multicenter Genetic Studies of Schizophrenia, C.Levinson, D. F.Gejman, P. V.Kendler, K. S.Laurent, C.Mowry, B. J.O'Donovan, M. C.Owen,

M. J.Pulver, A. E.Riley, B. P.Schwab, S. G.Wildenauer, D. B.Dudbridge, F.Holmans, P.Shi, J.Albus, M.Alexander, M.Campion, D.Cohen, D.Dikeos, D.Duan, J.Eichhammer, P.Godard, S.Hansen, M.Lerer, F. B.Liang, K. Y.Maier, W.Mallet, J.Nertney, D. A.Nestadt, G.Norton, N.O'Neill, F. A.Papadimitriou, G. N.Ribble, R.Sanders, A. R.Silverman, J. M.Walsh, D.Williams, N. M.Wormley, B.Psychosis Endophenotypes International, C.Arranz, M. J.Bakker, S.Bender, S.Bramon, E.Collier, D.Crespo-Facorro, B., et al. (2013) Genome-wide association analysis identifies 13 new risk loci for schizophrenia, *Nat Genet.* **45**, 1150-9.

84. Ohi, K., Hashimoto, R., Yamamori, H., Yasuda, Y., Fujimoto, M., Umeda-Yano, S., Fukunaga, M., Watanabe, Y., Iwase, M., Kazui, H. & Takeda, M. (2013) The impact of the genome-wide supported variant in the cyclin M2 gene on gray matter morphology in schizophrenia, *Behav Brain Funct.* **9**, 40.

85. Rose, E. J., Hargreaves, A., Morris, D., Fahey, C., Tropea, D., Cummings, E., Caltagirone, C., Bossu, P., Chiapponi, C., Piras, F., Spalletta, G., Gill, M., Corvin, A. & Donohoe, G. (2014) Effects of a novel schizophrenia risk variant rs7914558 at CNNM2 on brain structure and attributional style, *Br J Psychiatry.* **204**, 115-21.

86. Thyme, S. B., Pieper, L. M., Li, E. H., Pandey, S., Wang, Y., Morris, N. S., Sha, C., Choi, J. W., Herrera, K. J., Soucy, E. R., Zimmerman, S., Randlett, O., Greenwood, J., McCarroll, S. A. & Schier, A. F. (2019) Phenotypic Landscape of Schizophrenia-Associated Genes Defines Candidates and Their Shared Functions, *Cell.* **177**, 478-491 e20.

87. Urwyler, O., Izadifar, A., Vandenbogaerde, S., Sachse, S., Misbaer, A. & Schmucker, D. (2019) Branch-restricted localization of phosphatase Prl-1 specifies axonal synaptogenesis domains, *Science.* **364**.

88. Guo, P., Xu, X., Wang, F., Yuan, X., Tu, Y., Zhang, B., Zheng, H., Yu, D., Ge, W., Gong, Z., Yang, X. & Xi, Y. (2019) A Novel Neuroprotective Role of Phosphatase of Regenerating Liver-1 against CO2 Stimulation in Drosophila, *iScience.* **19**, 291-302.

89. Almagro Armenteros, J. J., Tsirigos, K. D., Sonderby, C. K., Petersen, T. N., Winther, O., Brunak, S., von Heijne, G. & Nielsen, H. (2019) SignalP 5.0 improves signal peptide predictions using deep neural networks, *Nat Biotechnol.* **37**, 420-423.

90. El-Gebali, S., Mistry, J., Bateman, A., Eddy, S. R., Luciani, A., Potter, S. C., Qureshi, M., Richardson, L. J., Salazar, G. A., Smart, A., Sonnhammer, E. L. L., Hirsh, L., Paladin, L.,

Piovesan, D., Tosatto, S. C. E. & Finn, R. D. (2019) The Pfam protein families database in 2019, *Nucleic Acids Res.* **47**, D427-D432.
91. Corral-Rodriguez, M. A., Stuiver, M., Abascal-Palacios, G., Diercks, T., Oyenarte, I., Ereno-Orbea, J., de Opakua, A. I., Blanco, F. J., Encinar, J. A., Spiwok, V., Terashima, H., Accardi, A., Muller, D. & Martinez-Cruz, L. A. (2014) Nucleotide binding triggers a conformational change of the CBS module of the magnesium transporter CNNM2 from a twisted towards a flat structure, *Biochem J.* **464**, 23-34.
92. Bateman, A. (1997) The structure of a domain common to archaebacteria and the homocystinuria disease protein, *Trends Biochem Sci.* **22**, 12-3.
93. Baykov, A. A., Tuominen, H. K. & Lahti, R. (2011) The CBS domain: a protein module with an emerging prominent role in regulation, *ACS Chem Biol.* **6**, 1156-63.
94. Yan, Y., Zhou, X. E., Xu, H. E. & Melcher, K. (2018) Structure and Physiological Regulation of AMPK, *Int J Mol Sci.* **19**.
95. Beis, I. & Newsholme, E. A. (1975) The contents of adenine nucleotides, phosphagens and some glycolytic intermediates in resting muscles from vertebrates and invertebrates, *Biochem J.* **152**, 23-32.
96. Gulerez, I., Funato, Y., Wu, H., Yang, M., Kozlov, G., Miki, H. & Gehring, K. (2016) Phosphocysteine in the PRL-CNNM pathway mediates magnesium homeostasis, *EMBO Rep.* **17**, 1890-1900.
97. Zhang, H., Kozlov, G., Li, X., Wu, H., Gulerez, I. & Gehring, K. (2017) PRL3 phosphatase active site is required for binding the putative magnesium transporter CNNM3, *Sci Rep.* **7**, 48.
98. Gimenez-Mascarell, P., Oyenarte, I., Hardy, S., Breiderhoff, T., Stuiver, M., Kostantin, E., Diercks, T., Pey, A. L., Ereno-Orbea, J., Martinez-Chantar, M. L., Khalaf-Nazzal, R., Claverie-Martin, F., Muller, D., Tremblay, M. L. & Martinez-Cruz, L. A. (2017) Structural Basis of the Oncogenic Interaction of Phosphatase PRL-1 with the Magnesium Transporter CNNM2, *J Biol Chem.* **292**, 786-801.
99. Saha, S., Bardelli, A., Buckhaults, P., Velculescu, V. E., Rago, C., St Croix, B., Romans, K. E., Choti, M. A., Lengauer, C., Kinzler, K. W. & Vogelstein, B. (2001) A phosphatase associated with metastasis of colorectal cancer, *Science.* **294**, 1343-6.

100. Clayton, G. M., Silverman, W. R., Heginbotham, L. & Morais-Cabral, J. H. (2004) Structural basis of ligand activation in a cyclic nucleotide regulated potassium channel, *Cell.* **119**, 615-27.
101. Holm, L. & Rosenstrom, P. (2010) Dali server: conservation mapping in 3D, *Nucleic Acids Res.* **38**, W545-9.
102. Pessoa, J., Fonseca, F., Furini, S. & Morais-Cabral, J. H. (2014) Determinants of ligand selectivity in a cyclic nucleotide-regulated potassium channel, *J Gen Physiol.* **144**, 41-54.
103. Lo, M. C., Aulabaugh, A., Jin, G., Cowling, R., Bard, J., Malamas, M. & Ellestad, G. (2004) Evaluation of fluorescence-based thermal shift assays for hit identification in drug discovery, *Anal Biochem.* **332**, 153-9.
104. Wong, K., Kozlov, G., Zhang, Y. & Gehring, K. (2015) Structure of the Legionella Effector, lpg1496, Suggests a Role in Nucleotide Metabolism, *J Biol Chem.* **290**, 24727-37.
105. Schaffers, O. J. M., Hoenderop, J. G. J., Bindels, R. J. M. & de Baaij, J. H. F. (2018) The rise and fall of novel renal magnesium transporters, *Am J Physiol Renal Physiol*.
106. Payandeh, J., Pfoh, R. & Pai, E. F. (2013) The structure and regulation of magnesium selective ion channels, *Biochim Biophys Acta.* **1828**, 2778-92.
107. Zagotta, W. N., Olivier, N. B., Black, K. D., Young, E. C., Olson, R. & Gouaux, E. (2003) Structural basis for modulation and agonist specificity of HCN pacemaker channels, *Nature.* **425**, 200-5.
108. Flynn, G. E., Black, K. D., Islas, L. D., Sankaran, B. & Zagotta, W. N. (2007) Structure and rearrangements in the carboxy-terminal region of SpIH channels, *Structure.* **15**, 671-82.
109. Kesters, D., Brams, M., Nys, M., Wijckmans, E., Spurny, R., Voets, T., Tytgat, J., Kusch, J. & Ulens, C. (2015) Structure of the SthK carboxy-terminal region reveals a gating mechanism for cyclic nucleotide-modulated ion channels, *PLoS One.* **10**, e0116369.
110. VanSchouwen, B. & Melacini, G. (2016) Regulation of HCN Ion Channels by Non-canonical Cyclic Nucleotides in *Non-canonical Cyclic Nucleotides* pp. 123-133, Springer.
111. Brelidze, T. I., Carlson, A. E., Sankaran, B. & Zagotta, W. N. (2012) Structure of the carboxy-terminal region of a KCNH channel, *Nature.* **481**, 530-3.
112. Weber, I. T. & Steitz, T. A. (1987) Structure of a complex of catabolite gene activator protein and cyclic AMP refined at 2.5 A resolution, *J Mol Biol.* **198**, 311-26.

113. James, Z. M. & Zagotta, W. N. (2018) Structural insights into the mechanisms of CNBD channel function, *J Gen Physiol.* **150**, 225-244.
114. Haitin, Y., Carlson, A. E. & Zagotta, W. N. (2013) The structural mechanism of KCNH-channel regulation by the eag domain, *Nature.* **501**, 444-8.
115. Otwinowski, Z. & Minor, W. (1997) [20] Processing of X-ray diffraction data collected in oscillation mode, *Methods Enzymol.* **276**, 307-326.
116. Adams, P. D., Afonine, P. V., Bunkoczi, G., Chen, V. B., Davis, I. W., Echols, N., Headd, J. J., Hung, L. W., Kapral, G. J., Grosse-Kunstleve, R. W., McCoy, A. J., Moriarty, N. W., Oeffner, R., Read, R. J., Richardson, D. C., Richardson, J. S., Terwilliger, T. C. & Zwart, P. H. (2010) PHENIX: a comprehensive Python-based system for macromolecular structure solution, *Acta Crystallogr D Biol Crystallogr.* **66**, 213-21.
117. Terwilliger, T. C., Grosse-Kunstleve, R. W., Afonine, P. V., Moriarty, N. W., Zwart, P. H., Hung, L. W., Read, R. J. & Adams, P. D. (2008) Iterative model building, structure refinement and density modification with the PHENIX AutoBuild wizard, *Acta Crystallogr D Biol Crystallogr.* **64**, 61-9.
118. Emsley, P., Lohkamp, B., Scott, W. G. & Cowtan, K. (2010) Features and development of Coot, *Acta Crystallogr D Biol Crystallogr.* **66**, 486-501.
119. Murshudov, G. N., Skubak, P., Lebedev, A. A., Pannu, N. S., Steiner, R. A., Nicholls, R. A., Winn, M. D., Long, F. & Vagin, A. A. (2011) REFMAC5 for the refinement of macromolecular crystal structures, *Acta Crystallogr D Biol Crystallogr.* **67**, 355-67.
120. Painter, J. & Merritt, E. A. (2006) Optimal description of a protein structure in terms of multiple groups undergoing TLS motion, *Acta Crystallogr D Biol Crystallogr.* **62**, 439-50.
121. McCoy, A. J., Grosse-Kunstleve, R. W., Adams, P. D., Winn, M. D., Storoni, L. C. & Read, R. J. (2007) Phaser crystallographic software, *J Appl Crystallogr.* **40**, 658-674.
122. Afonine, P. V., Grosse-Kunstleve, R. W., Echols, N., Headd, J. J., Moriarty, N. W., Mustyakimov, M., Terwilliger, T. C., Urzhumtsev, A., Zwart, P. H. & Adams, P. D. (2012) Towards automated crystallographic structure refinement with phenix.refine, *Acta Crystallogr D Biol Crystallogr.* **68**, 352-67.
123. Laskowski, R. A., MacArthur, M. W., Moss, D. S. & Thornton, J. M. (1993) PROCHECK: a program to check the stereochemical quality of protein structures, *Journal of applied crystallography.* **26**, 283-291.

124. Delaglio, F., Grzesiek, S., Vuister, G. W., Zhu, G., Pfeifer, J. & Bax, A. (1995) NMRPipe: a multidimensional spectral processing system based on UNIX pipes, *J Biomol NMR.* **6**, 277-93.
125. Goddard, T. & Kneller, D. (2008) SPARKY 3, *University of California, San Francisco*.
126. Schuck, P. (2000) Size-distribution analysis of macromolecules by sedimentation velocity ultracentrifugation and lamm equation modeling, *Biophys J.* **78**, 1606-19.
127. Laue, T., Bhairavi, D., Ridgeway, T. & Pelletier, S. (1992) SE Harding, and AJ Rowe, and JC Horton, eds. Analytical Ultracentrifugation in Biochemistry and Polymers Science 90-125 in, Royal Society of Chemistry, Cambridge, UK,
128. Brookes, E., Demeler, B. & Rocco, M. (2010) Developments in the US-SOMO bead modeling suite: new features in the direct residue-to-bead method, improved grid routines, and influence of accessible surface area screening, *Macromol Biosci.* **10**, 746-53.
129. Brautigam, C. A. (2015) Calculations and Publication-Quality Illustrations for Analytical Ultracentrifugation Data, *Methods Enzymol.* **562**, 109-33.
130. Funato, Y. & Miki, H. (2019) Molecular function and biological importance of CNNM family Mg2+ transporters, *J Biochem.* **165**, 219-225.
131. Chen, Y. S., Kozlov, G., Fakih, R., Funato, Y., Miki, H. & Gehring, K. (2018) The cyclic nucleotide-binding homology domain of the integral membrane protein CNNM mediates dimerization and is required for Mg(2+) efflux activity, *J Biol Chem.* **293**, 19998-20007.
132. Feng, L., Campbell, E. B., Hsiung, Y. & MacKinnon, R. (2010) Structure of a eukaryotic CLC transporter defines an intermediate state in the transport cycle, *Science.* **330**, 635-41.
133. Markovic, S. & Dutzler, R. (2007) The structure of the cytoplasmic domain of the chloride channel ClC-Ka reveals a conserved interaction interface, *Structure.* **15**, 715-25.
134. Meyer, S. & Dutzler, R. (2006) Crystal structure of the cytoplasmic domain of the chloride channel ClC-0, *Structure.* **14**, 299-307.
135. Meyer, S., Savaresi, S., Forster, I. C. & Dutzler, R. (2007) Nucleotide recognition by the cytoplasmic domain of the human chloride transporter ClC-5, *Nat Struct Mol Biol.* **14**, 60-7.
136. Park, E., Campbell, E. B. & MacKinnon, R. (2017) Structure of a CLC chloride ion channel by cryo-electron microscopy, *Nature.* **541**, 500-505.
137. Park, E. & MacKinnon, R. (2018) Structure of the CLC-1 chloride channel from Homo sapiens, *Elife.* **7**, e36629.

138. Kovrigin, E. L. (2012) NMR line shapes and multi-state binding equilibria, *J Biomol NMR.* **53**, 257-70.
139. Kovrigin, E. L. (2017) Resolving Three-State Ligand-Binding Mechanisms by Isothermal Titration Calorimetry: A Simulation Study, *bioRxiv*, 145516.
140. Ereno-Orbea, J., Oyenarte, I. & Martinez-Cruz, L. A. (2013) CBS domains: Ligand binding sites and conformational variability, *Arch Biochem Biophys.* **540**, 70-81.
141. Hattori, M., Iwase, N., Furuya, N., Tanaka, Y., Tsukazaki, T., Ishitani, R., Maguire, M. E., Ito, K., Maturana, A. & Nureki, O. (2009) Mg(2+)-dependent gating of bacterial MgtE channel underlies Mg(2+) homeostasis, *EMBO J.* **28**, 3602-12.
142. Hattori, M., Tanaka, Y., Fukai, S., Ishitani, R. & Nureki, O. (2007) Crystal structure of the MgtE Mg2+ transporter, *Nature.* **448**, 1072-5.
143. Ishitani, R., Sugita, Y., Dohmae, N., Furuya, N., Hattori, M. & Nureki, O. (2008) Mg2+-sensing mechanism of Mg2+ transporter MgtE probed by molecular dynamics study, *Proc Natl Acad Sci U S A.* **105**, 15393-8.
144. Gupta, R. K. & Yushok, W. D. (1980) Noninvasive 31P NMR probes of free Mg2+, MgATP, and MgADP in intact Ehrlich ascites tumor cells, *Proc Natl Acad Sci U S A.* **77**, 2487-91.
145. Williams, G. D., Mosher, T. J. & Smith, M. B. (1993) Simultaneous determination of intracellular magnesium and pH from the three 31P NMR Chemical shifts of ATP, *Anal Biochem.* **214**, 458-67.
146. Kowal, J., Biyani, N., Chami, M., Scherer, S., Rzepiela, A. J., Baumgartner, P., Upadhyay, V., Nimigean, C. M. & Stahlberg, H. (2018) High-Resolution Cryoelectron Microscopy Structure of the Cyclic Nucleotide-Modulated Potassium Channel MloK1 in a Lipid Bilayer, *Structure.* **26**, 20-27 e3.
147. Mossessova, E. & Lima, C. D. (2000) Ulp1-SUMO crystal structure and genetic analysis reveal conserved interactions and a regulatory element essential for cell growth in yeast, *Mol Cell.* **5**, 865-76.
148. Karplus, P. A. & Diederichs, K. (2015) Assessing and maximizing data quality in macromolecular crystallography, *Curr Opin Struct Biol.* **34**, 60-8.
149. Chen, V. B., Arendall, W. B., 3rd, Headd, J. J., Keedy, D. A., Immormino, R. M., Kapral, G. J., Murray, L. W., Richardson, J. S. & Richardson, D. C. (2010) MolProbity: all-atom

structure validation for macromolecular crystallography, *Acta Crystallogr D Biol Crystallogr.* **66**, 12-21.
150. Daneshmandpour, Y., Darvish, H., Pashazadeh, F. & Emamalizadeh, B. (2019) Features, genetics and their correlation in Jalili syndrome: a systematic review, *J Med Genet.* **56**, 358-369.
151. Akanuma, G., Kobayashi, A., Suzuki, S., Kawamura, F., Shiwa, Y., Watanabe, S., Yoshikawa, H., Hanai, R. & Ishizuka, M. (2014) Defect in the formation of 70S ribosomes caused by lack of ribosomal protein L34 can be suppressed by magnesium, *J Bacteriol.* **196**, 3820-30.
152. Resch, C. T., Winogrodzki, J. L., Patterson, C. T., Lind, E. J., Quinn, M. J., Dibrov, P. & Hase, C. C. (2010) The putative Na+/H+ antiporter of Vibrio cholerae, Vc-NhaP2, mediates the specific K+/H+ exchange in vivo, *Biochemistry.* **49**, 2520-8.
153. Chen, Y. S., Kozlov, G., Fakih, R., Yang, M., Zhang, Z., Kovrigin, E. L. & Gehring, K. (2020) Mg(2+)-ATP Sensing in CNNM, a Putative Magnesium Transporter, *Structure.* **28**, 324-335 e4.
154. Zheng, H., Chordia, M. D., Cooper, D. R., Chruszcz, M., Muller, P., Sheldrick, G. M. & Minor, W. (2014) Validation of metal-binding sites in macromolecular structures with the CheckMyMetal web server, *Nat Protoc.* **9**, 156-70.
155. Lunin, V. V., Dobrovetsky, E., Khutoreskaya, G., Zhang, R., Joachimiak, A., Doyle, D. A., Bochkarev, A., Maguire, M. E., Edwards, A. M. & Koth, C. M. (2006) Crystal structure of the CorA Mg2+ transporter, *Nature.* **440**, 833-7.
156. Payandeh, J. & Pai, E. F. (2006) A structural basis for Mg2+ homeostasis and the CorA translocation cycle, *EMBO J.* **25**, 3762-73.
157. Eshaghi, S., Niegowski, D., Kohl, A., Martinez Molina, D., Lesley, S. A. & Nordlund, P. (2006) Crystal structure of a divalent metal ion transporter CorA at 2.9 angstrom resolution, *Science.* **313**, 354-7.
158. Kawate, T. & Gouaux, E. (2006) Fluorescence-detection size-exclusion chromatography for precrystallization screening of integral membrane proteins, *Structure.* **14**, 673-81.
159. Nimigean, C. M. (2006) A radioactive uptake assay to measure ion transport across ion channel-containing liposomes, *Nat Protoc.* **1**, 1207-12.

160. Feng, N., Qi, C., Hou, Y. J., Zhang, Y., Wang, D. C. & Li, D. F. (2018) The C2'- and C3'-endo equilibrium for AMP molecules bound in the cystathionine-beta-synthase domain, *Biochem Biophys Res Commun.* **497**, 646-651.
161. Jurrus, E., Engel, D., Star, K., Monson, K., Brandi, J., Felberg, L. E., Brookes, D. H., Wilson, L., Chen, J., Liles, K., Chun, M., Li, P., Gohara, D. W., Dolinsky, T., Konecny, R., Koes, D. R., Nielsen, J. E., Head-Gordon, T., Geng, W., Krasny, R., Wei, G. W., Holst, M. J., McCammon, J. A. & Baker, N. A. (2018) Improvements to the APBS biomolecular solvation software suite, *Protein Sci.* **27**, 112-128.
162. Charpentier, E., Anton, A. I., Barry, P., Alfonso, B., Fang, Y. & Novick, R. P. (2004) Novel cassette-based shuttle vector system for gram-positive bacteria, *Appl Environ Microbiol.* **70**, 6076-85.
163. Tu Quoc, P. H., Genevaux, P., Pajunen, M., Savilahti, H., Georgopoulos, C., Schrenzel, J. & Kelley, W. L. (2007) Isolation and characterization of biofilm formation-defective mutants of Staphylococcus aureus, *Infect Immun.* **75**, 1079-88.
164. Ritchie, T. K., Grinkova, Y. V., Bayburt, T. H., Denisov, I. G., Zolnerciks, J. K., Atkins, W. M. & Sligar, S. G. (2009) Chapter 11 - Reconstitution of membrane proteins in phospholipid bilayer nanodiscs, *Methods Enzymol.* **464**, 211-31.
165. Jenkins, M. L., Margaria, J. P., Stariha, J. T. B., Hoffmann, R. M., McPhail, J. A., Hamelin, D. J., Boulanger, M. J., Hirsch, E. & Burke, J. E. (2018) Structural determinants of Rab11 activation by the guanine nucleotide exchange factor SH3BP5, *Nat Commun.* **9**, 3772.
166. Lucic, I., Rathinaswamy, M. K., Truebestein, L., Hamelin, D. J., Burke, J. E. & Leonard, T. A. (2018) Conformational sampling of membranes by Akt controls its activation and inactivation, *Proc Natl Acad Sci U S A.* **115**, E3940-E3949.
167. Park, M. H., Wong, B. B. & Lusk, J. E. (1976) Mutants in three genes affecting transport of magnesium in Escherichia coli: genetics and physiology, *J Bacteriol.* **126**, 1096-103.
168. Piskacek, M., Zotova, L., Zsurka, G. & Schweyen, R. J. (2009) Conditional knockdown of hMRS2 results in loss of mitochondrial Mg(2+) uptake and cell death, *J Cell Mol Med.* **13**, 693-700.
169. Guskov, A., Nordin, N., Reynaud, A., Engman, H., Lundback, A. K., Jong, A. J., Cornvik, T., Phua, T. & Eshaghi, S. (2012) Structural insights into the mechanisms of Mg2+ uptake, transport, and gating by CorA, *Proc Natl Acad Sci U S A.* **109**, 18459-64.

170. Pfoh, R., Li, A., Chakrabarti, N., Payandeh, J., Pomes, R. & Pai, E. F. (2012) Structural asymmetry in the magnesium channel CorA points to sequential allosteric regulation, *Proc Natl Acad Sci U S A.* **109**, 18809-14.
171. Nordin, N., Guskov, A., Phua, T., Sahaf, N., Xia, Y., Lu, S., Eshaghi, H. & Eshaghi, S. (2013) Exploring the structure and function of Thermotoga maritima CorA reveals the mechanism of gating and ion selectivity in Co2+/Mg2+ transport, *Biochem J.* **451**, 365-74.
172. Matthies, D., Dalmas, O., Borgnia, M. J., Dominik, P. K., Merk, A., Rao, P., Reddy, B. G., Islam, S., Bartesaghi, A., Perozo, E. & Subramaniam, S. (2016) Cryo-EM Structures of the Magnesium Channel CorA Reveal Symmetry Break upon Gating, *Cell.* **164**, 747-56.
173. Goytain, A. & Quamme, G. A. (2005) Functional characterization of human SLC41A1, a Mg2+ transporter with similarity to prokaryotic MgtE Mg2+ transporters, *Physiol Genomics.* **21**, 337-42.
174. Takeda, H., Hattori, M., Nishizawa, T., Yamashita, K., Shah, S. T., Caffrey, M., Maturana, A. D., Ishitani, R. & Nureki, O. (2014) Structural basis for ion selectivity revealed by high-resolution crystal structure of Mg2+ channel MgtE, *Nat Commun.* **5**, 5374.
175. Tomita, A., Zhang, M., Jin, F., Zhuang, W., Takeda, H., Maruyama, T., Osawa, M., Hashimoto, K. I., Kawasaki, H., Ito, K., Dohmae, N., Ishitani, R., Shimada, I., Yan, Z., Hattori, M. & Nureki, O. (2017) ATP-dependent modulation of MgtE in Mg(2+) homeostasis, *Nat Commun.* **8**, 148.
176. Jin, F., Sun, M., Fujii, T., Yamada, Y., Wang, J., Maturana, A. D., Wada, M., Su, S., Ma, J., Takeda, H., Kusakizako, T., Tomita, A., Nakada-Nakura, Y., Liu, K., Uemura, T., Nomura, Y., Nomura, N., Ito, K., Nureki, O., Namba, K., Iwata, S., Yu, Y. & Hattori, M. (2020) Cryo-EM structure of the MgtE Mg(2+) channel pore domain in Mg(2+)-free conditions reveals cytoplasmic pore opening, *bioRxiv*, 2020.08.27.270991.
177. Kuang, Q., Purhonen, P. & Hebert, H. (2015) Structure of potassium channels, *Cell Mol Life Sci.* **72**, 3677-93.
178. Palombo, I., Daley, D. O. & Rapp, M. (2013) Why is the GMN motif conserved in the CorA/Mrs2/Alr1 superfamily of magnesium transport proteins?, *Biochemistry.* **52**, 4842-7.
179. Imai, S., Maruyama, T., Osawa, M., Hattori, M., Ishitani, R., Nureki, O. & Shimada, I. (2012) Spatial distribution of cytoplasmic domains of the Mg(2+)-transporter MgtE, in a solution

lacking Mg(2+), revealed by paramagnetic relaxation enhancement, *Biochim Biophys Acta.* **1824**, 1129-35.